Electron Dynamics in Low-Dimensional Surfaces Studied by Time-Resolved Photoelectron Spectroscopy

---

Dissertation

zur

Erlangung der naturwissenschaftlichen Doktorwürde
(Dr. sc. nat.)

vorgelegt der

Mathematisch-naturwissenschaftlichen Fakultät

der

Universität Zürich

von

Dominik Leuenberger
von Walterswil (BE)

Promotionskomitee

Prof. Dr. Jürg Osterwalder (Vorsitz und Leitung der Dissertation)
Dr. Matthias Hengsberger
Prof. Dr. Martin Aeschlimann

Zürich 2012

Die vorliegende Arbeit wurde von der Mathematisch-Naturwissenschaftlichen Fakultät der Universität Zürich im Herbstsemester 2011/2012 als Dissertation angenommen.

Promotionskomitee: Prof. Dr. Jürg Osterwalder (Vorsitzender und Leiter der Dissertation),
Dr. Matthias Hengsberger (Betreuer) und
Prof. Dr. Martin Aeschlimann (Gutachter).

Abstract

In this thesis, time-resolved photoelectron spectroscopy was used for the investigation of electron dynamics in low-dimensional surfaces and interfaces.

An atomic layer of hexagonal boron nitride (*h*-BN) on top of a Ni(111) surface serves as model system for a two-dimensional metal-insulator interface. Previous time-resolved two-photon photoemission (TR-2PPE) measurements revealed two unoccupied electronic states, both with remarkable long lifetimes in the order of hundred femtoseconds.

The first state is a so called interface state which is spatially located between the boron nitride layer and the nickel surface. It was predicted by both density functional theory and calculations within the dielectric continuum model, respectively. Resonant two-photon photoemission (2PPE) was used in order to tackle the binding energy and dispersion of this state. A large difference in binding energy of 190 meV, found from direct comparison between the 2PPE measurements and corresponding results from inverse photoemission, is discussed in terms of an excitonic excitation at the *h*-BN/Ni(111) interface.

The second unoccupied feature in the TR-2PPE spectra from *h*-BN/Ni(111) belongs to the Rydberg series of image potential states (IPS). Spatially located a few Ångström in front of the surface the lowest lying image potential state turns out to be sensitive on the sample temperature dependent ferromagnetic phase transition across the Curie temperature of Ni. Based on this finding a *h*-BN/Ni(111) film was initially excited by means of an intense infrared laser pulse. A transient change of the energy position of the IPS within the first 300 fs after excitation by the infrared pump pulse is discussed in terms of ultrafast demagnetization of the Ni substrate. Space-charge simulations were performed in order to disentangle the transient energy shifts caused by electron-dynamics in the solid from the spectral distortions caused by mutual Coulomb repulsions of the photoelectrons in vacuum.

The 'machine part' of this thesis mainly consists of the commissioning and characterization of an elliptical display analyzer (EDA) for low energy laser pulses. This parallel data acquisition scheme paved the way for circular dichroism experiments in the angular distribution (CDAD) without the interference of photoemission matrix elements. The spin-splitting of the quasi one-dimensional surface state of the Bi(114) surface was revealed by CDAD using the EDA, in agreement with the results of previous spin- and angle-resolved photoemission experiments.

At last, time- and angle-resolved photoemission measurements from the one-dimensional Bi(114) surface were performed. The transient hot electron population in the Bi conduction band, created by absorption of an intense infrared laser pulse, relaxes by means of electron-electron and electron-phonon scattering processes on a femtosecond time scale. The excitation of coherent optical phonons at the Bi(114) surface leads to periodic modifications of the time-resolved photoelectron spectra on a picosecond time scale. From comparison with theoretical phonon dispersion calculations the strong periodic modification of the time-resolved photoelectron spectra have been identified to be caused mainly by optical phonons, with a frequency of 0.7 THz, forming a standing wave along the atomic rows of the vicinal Bi(114) surface.

Zusammenfassung

In der vorliegenden Doktorarbeit wurden dynamische elektronische Prozesse in niedrig dimensionalen Oberflächen mit Hilfe von zeitaufgelöster Photoelektronen-Spektroskopie untersucht.

Eine monoatomare Schicht von hexagonalem Bornitrid (h-BN) auf einer Ni(111) Oberfläche diente als Modellsystem für eine zweidimensionale Isolator-Metall-Grenzfläche. Frühere Experimente zeigten die Existenz von zwei unbesetzten elektronischen Zuständen, beide mit beachtlich langen Lebensdauern von mehreren hundert Femtosekunden.

Der erste Zustand ist ein sogenannter Interface-Zustand, der räumlich zwischen der Nickel Oberfläche und der Bornitrid Schicht lokalisiert ist und mit Hilfe der Dichtefunktionaltheorie und des dielektrischen Kontinuumsmodells vorhergesagt wurde. Resonante Zwei-Photo-Photoemissionsmessungen (2PPE) erlauben es, die Bindungsenergie und die Dispersion des besagten Zustandes mit hoher Genauigkeit zu vermessen. Die gefundene Abweichung von 190 meV im Vergleich zu früheren inversen Photoemissionsmessungen wird im Rahmen einer exitonischen Anregung in der h-BN/Ni(111) Schnittstelle diskutiert.

Der zweite unbesetzte Zustand ist ein sogenannter Bildladungszustand, der nur wenige Ångström vor der Oberfläche lokalisiert ist. Temperaturabhängige 2PPE-Messungen zeigen, dass der Zustand empfindlich auf den ferromagnetischen Phasenübergang der Nickel Oberfläche reagiert. Gestützt auf diesen Befund wurden zeitaufgelöste Messungen mit intensiven Infrarot-Laserpulsen durchgeführt. Eine transiente Verschiebung der Bindungsenergie des Bildladungszustandes innerhalb von 300 Femtosekunden nach der Einwirkung des Infrarot-Laserpulses könnte ein Hinweis auf die ultraschnelle Demagnetisierung der Nickeloberfläche sein. Um diese kleinen Effekte aus den Rohdaten extrahieren zu können, wurden Simulationen der störenden spektralen Verbreiterungen und Verschiebungen, verursacht durch abstossende Coulombkräfte unter den Photoelektronen im Vakuum, gerechnet.

Der experimentelle Hauptteil dieser Arbeit beinhaltet die Inbetriebnahme und Charakterisierung eines Ellipsoidalen Display Analysators (EDA) für niederenergetische Laserpulse. Der EDA erlaubt eine parallele Datenakquisition und ermöglicht somit Zirkular-Dichroismus Experimente in der Winkelverteilung von Photoelektronen ohne die beeinträchtigen Effekte von Photoemissions-Matrixelementen. Als Beispiel dafür wurde der spin-aufgespaltene eindimensionale Oberflächenzustand der Bi(114) Oberfläche aufgelöst.

Schliesslich wurde auf dieser vizinalen Bi(114) Oberfläche mit Hilfe von zeitaufgelöster Photoemission die Dynamik von kurzlebigen Elektronenpopulationen studiert. Die Absorption eines intensiven Infrarot-Laserpulses resultiert in einer angeregten Besetzung des Bi Leitungsbands, die durch Elektron-Elektron und Elektron-Phonon Streuprozesse zerfällt. Dabei werden koheränte Gitterschwingungen angeregt, welche die zeitabhängigen Photoelektronenspektren periodisch auf einer Pikosekunden Zeitskala modulieren. Durch den Vergleich mit gerechneten Dispersionskurven von Gitterschwingungen in Bi konnte die gefundene Mode mit einer Frequenz von 0.7 THz als eine koheränt angeregte stehende Welle entlang der atomaren Reihen der Bi(114) Oberfläche identifiziert werden.

List of Acronyms

1D/ 2D/ 3D	one-/ two-/three-dimensional
ARPES	angle resolved photoelectron spectroscopy
BZ	Brillouin zone
CB	conduction band
CDAD	circular dichroism in the angular distribution
DCM	dielectric continuum model
DFT	density functional theory
DOS	density of states
EDA	elliptical display analyzer
ESCA	electron spectroscopy for chemical analysis
fcc	face centered cubic (lattice)
FT	Fourier transform
FSM	photoemission Fermi surface map
FWHM	full width at half maximum
$h-$BN	hexagonal boron nitride
hcp	hexagonal close-packed (lattice)
IPE	inverse photoemission
IPS	image potential state
IR	infrared
LEED	low energy electron diffraction
PES	photoemssion spectroscopy
SBZ	surface Brillouin zone
SEM	scanning electron microscopy
SH	second harmonic
SHG	second harmonic generation
SLS	Swiss Light Source
SNR	signal to noise ratio
STM	scanning tunneling microscopy/microscope
SR-IPE	spin-resolved inverse photoemission
TR-PES	time-resolved photoemssion spectroscopy
TR-2PPE	time-resolved two photon photoemssion
TR-XRD	time-resolved X-ray diffraction
UFDM	ultrafast demagnetization
UHV	ultra-high vacuum
UPD	ultraviolet photoelectron diffraction
UPS	ultraviolet photoelectron spectroscopy
UV	ultraviolet (radiation)
XMCD	X–ray magnetic circular dichroism
XPD	X–ray photoelectron diffraction
XPS	X–ray photoelectron spectroscopy

Contents

1 Introduction and motivation

Parallel data acquisition with an elliptical display analyzer: The absorption of intense femtosecond (10^{-15} s) laser pulses in solids causes non-equilibrium conditions in the structural, electronic and magnetic order of a solid state system on a very short time scale. The relaxation of the system towards a dynamic equilibrium includes several scattering processes as *e.g.* electron-electron or electron-phonon scattering. These microscopic scattering processes in solids, at solid state surfaces or interfaces are governed by strong interactions and, therefore, occur on an ultrafast time scale ranging from attoseconds (10^{-18} s) to picoseconds (10^{-12} s).

Photoelectron spectroscopy (PES) and photoelectron diffraction are well established and powerful techniques for resolving the electronic and spatial structure of surfaces. Furthermore angle-resolved photoelectron spectroscopy (ARPES) provides direct access to the band structure in the reciprocal k-space of a solid state system.

Combining this photoemission techniques with pulsed ultrafast laser light sources in a pump-probe scheme allows one to probe the dynamical behavior of electrons in non-equilibrium conditions in solids induced by a pump pulse directly in the time domain. This work will focus on two time-resolved PES techniques: While time-resolved ARPES (TR-ARPES) experiments add important information about collective excitations in the occupied band structure, time-resolved two-photon photelectron spectroscopy (TR-2PPES) monitors energy and momentum relaxation dynamics of unoccupied electronic states on a femtosecond time scale.

Compared to conventional ARPES experiments the investigation of dynamical processes directly in the time domain increases the experimental parameter space by one extra dimension. A reduced data acquisition time as well as other advantages like *e.g.* the elimination of matrix element effects in photoemission require parallel data acquisition schemes in time-resolved photoelectron spectroscopy experiments.

An integral part of this thesis was the commissioning and optimization of an ellipsoidal display analyzer (EDA) [1–3] for time-resolved photoemission experiments at low photon energies. The EDA is a parallel data acquisition system based on electrostatic reflection of photoelectrons at an elliptical mirror. The detector is capable of monitoring simultaneously snapshots of photoelectron distributions at constant energy being emitted into an emission cone of ±43°. In contrast to state-of-the-art two-dimensional time-of-flight detectors [4,5] which require pulsed photon sources in order to resolve the energy of the photoelectrons the detection scheme of an EDA allows one to combine both time-resolved experiments using low photon energy laser pulses and various surface characterization possibilities (XPS, LEED) using continuous sources, respectively.

Regarding future time-resolved experiments with the Swiss X-ray free-electron laser (XFEL) at the Paul Scherrer Institute (PSI) detailed knowledge and experience in parallel detection of photoelectrons will be a must. Highly brilliant X-ray bursts with femtosecond pulse duration[1] will

---

[1] The SwissXFEL will deliver $5 \cdot 10^{12}$ photons per pulse within a temporal pulse duration of 20 fs at a repetition rate of 100 Hz with a maximum photon energy of 12.4 keV [6]. Note that the brilliance within the pulse duration of present XFELs is larger by ten orders of magnitude than the ones of modern 3rd generation synchrotons.

enable us to study hot and dense plasmas similar to those at the heart of stars and planets. The investigation of ultrafast effects in correlated electron materials like ferromagnets and superconducters, cell imaging and the structure analysis of proteins and inorganic crystals in single shot experiments will lead to field ionisation and multiphoton processes above the damage threshold. Numerous charged particles, electrons and photons resulting from the interaction with a single incident XFEL pulse and being scattered over a wide solid angle raise the demand for parallel and simultaneous detection schemes.

Aiming towards the understanding of molecular electron transfer and possible future devices with ultrafast molecular switches the Swiss collaboration for molecular ultrafast science and technology (MUST) started in 2010. One particular project within this framework focuses on the study of structural dynamics of molecular adsorbate layers and solid surfaces by means of time-resolved UV photoelectron diffraction (TR-UPD). Electrons are photoemitted from the molecular adsorbate layers by means of femtosecond pulses with photon energies in the order of 40 eV which could either be provided by a free-electron laser or by means of high harmonic generation (HHG) from a laboratory Ti:sapphire laser system, respectively. The detection of photoelectron scattering patterns over a wide solid angle range up to the whole hemisphere is a necessary condition for tracing structural dynamics of the molecules under investigation.

Another main focus of our group within this collaboration are attosecond streaking experiments using higher harmonic pump pulses and the phase stabilized fundamental probe pulses of a tabletop laser system for temporally resolving electron dynamics on the attosecond time scale. Electrons initially released into the vacuum by photoemission from a higher harmonic pulse are subsequently modulated in kinetic energy and momentum by the electrical field of a infrared few cycle pulse. Delay dependent changes of the photoelectron momentum perpendicular to the propagation direction are preferentially measured in a two-dimensional detector.

In that sense preliminary experiences with parallel data acquisition of photoelectrons using the EDA detection scheme are important for the design and realization of various experiments in the near future.

The two-dimensional h-BN/Ni(111) interface: Nanotechnology and nanoscience are driven by the study of surfaces and interfaces between two solids with different electronic properties. The unique physical and chemical properties of these objects are often influenced by their morphology, the spatial structure and interplaying quantum size effects.

A monoatomic layer of hexagonal boron nitride (*h*-BN) on top of a ferromagnetic Ni(111) surface serves in this work as model system for an insulator-metal interface. The presence of an insulating capping layer on top of the ferromagnetic metal surface substrate adds additional occupied and unoccupied electronic states when compared to a bare metal surface system. Furthermore the robust *h*-BN layer enhances significantly the chemical inertness of the surfaces compared to bare Ni and was found to have a very low defect density, all very appreciated characteristics for surface physics studies.

TR-2PPE spectroscopy allows one to identify the existence and to investigate the dynamics of unoccupied (boron nitride related) electronic states. The topic of excitonic excitations in *h*-BN will be discussed in this chapter. This is from particular interest since *e.g.* TR-2PPE studies have shown that exciton excitation in semiconductor heterojunctions (donors and acceptors) are the limiting factor for charge separation in organic solar cells [7].

In a next step we investigated the ferromagnetic properties of the h-BN/Ni(111) surface. The rapidly increasing information density of modern magnetic data storage systems constantly push the limits of bit size and writing speed. One conventional way to record a bit is to reverse the magnetization by applying a magnetic field parallel to the magnetization direction. Perpendicularly aligned picosecond magnetic field pulses turned out to reverse the magnetization much faster on an ultrafast time scale of 200 ps by means of precessional reversal [8]. Deterministic precessional switching does not take place below an ultimate limit of 2 ps since at that time scale the intense magnetic field pulses start to fracture the magnetization resulting in random switching [9]. In 2007 it was demonstrated that circularly polarized femtosecond light pulses can reverse the magnetization in an all optical experiment without an external magnetic field by means of the inverse Faraday effect [10]. The ultrafast optical heating makes the magnetic system highly susceptible to the magnetic field simultaneously generated by the circularly polarized light pulses. The fastest way to demagnetize a ferromagnetic thin film in a non-deterministic way on a time scale of a few 100 fs by means of an intense infrared laser pulse has been reported for the first time in 1996 [11] and has been confirmed later by time-resolved photoemission [12, 13], by time-resolved magnetic optical Kerr experiments [14] and X-ray magnetic circular dichroism (XMCD) [15].

Considering the strong progress in this field it is certainly worth to investigate the sensitivity of the unoccupied states of *h*-BN/Ni(111) to the magnetic order of the Ni substrate across the ferromagnetic phase transition, for both static sample temperature dependent equilibrium conditions and laser pulse induced changes on an ultrafast time scale, respectively. Either localized at the metal-insulator interface or a few Ångström in front of the *h*-BN/Ni(111) surface, respectively, the investigated states turned out to be sensitive on the long-range order of the ferromagnetic nickel substrate. One may think of these states as "contactless magnetization probe" on a very small time and length scale.

The quasi one-dimensional Bi(114) surface: Reduced dimensionality at the surfaces of solids often results in unique characteristics of the electronic structure at the surface compared to the bulk. Furthermore in a rather new phase of solids, the so called topological insulators, the transition from such a material to a normal insulator (*e.g.* the transition from a topological insulator to vacuum at the solid surface) dictates the existence of topologically protected metallic states at the solid surface. Electrons in such surface states are protected against backscattering by time-reversal symmetry and therefor these states are highly robust against surface contamination in contrast to conventional metallic surface states.

Bulk bismuth is a semimetal with a low density of electronic states (DOS) at the Fermi level and poor electrical conductivity. At the surface of Bi the DOS as well as the conductivity is significantly enhanced due to the symmetry breaking and the corresponding existence of metallic states in the first few surface layers.

The vicinal Bi(114) surface is terminated by one-dimensional atomic rows. The strongly anisotropic (114) surface was found to support a quasi-one-dimensional metallic surface state [16]. The degeneracy of the surface state electrons is lifted along the direction of the atomic rows due to the strong spin-orbit coupling in the heavy element bismuth[2]. The corresponding Fermi surface contour consists of two parallel lines with opposite spin direction. Therefore the surface state of Bi(114) strongly resembles the edge states in the quantum spin Hall effect [16,17]. Similar surface structures made of insulating compounds as *e.g.* a $Bi_{0.9}Sb_{0.1}$ alloy could be promising candidates for one-dimensional topological insulators. Within the field of spintronics, where not only the charge but also the spin of an electron is used as an information, one may think about possible applications of these spin-split, one-dimensional and topologically protected surface states as spin-filters in future devices.

The low DOS at the Fermi level of bulk bismuth which is dominated by the surface states makes these surfaces in particular very sensitive to optical excitations. One would expect long lifetimes for transient electronic excitations due to the small scattering phase space at the Fermi level. Furthermore coherent electronic excitations are well known to be the driving force for coherent phonons in bismuth on an ultrafast time scale. TR-ARPES experiments are the method of choice for monitoring the effect of such collective coherent excitations on the electronic structure of Bi(114).

Beside many interesting physical properties the anisotropic electronic structure also serves as model system for characterizing the Fermi surface mapping capabilities of the EDA at low photon energies.

---

[2] The atomic number of bismuth is 83.

2 Experimental techniques and setup

2.1 Photoelectron spectroscopy

Photoelectron spectroscopy makes use of the photoelectric effect, which was first observed by Hertz in 1887 [18] and explained by Einstein (1905) by invoking the quantum nature of light [19]: When light is incident on a sample, an electron can absorb a photon and escape from the material. The kinetic energy of the outcoming electron is

$$E_{kin} = h\nu - \Phi - E_B \quad , \tag{1}$$

where h is the constant of Planck, ν the photon frequency, Φ the material work function and E_B the binding energy of the electron. For incident light with high energy (between 100 eV and 10 keV) the method is called X-ray photoemission spectroscopy (XPS), whereas for $h\nu$ between 5 eV and 50 eV it is called ultraviolet photoemission spectroscopy (UPS). With UPS, valence and conduction electrons can be examined, because they have a large absorption cross section for the photons from UV light.

The emitted electrons escape in all directions into the vacuum and are collected with an energy analyzer. The measurement is called angle-resolved photoelectron spectroscopy (ARPES) if the kinetic energy E_{kin} of the photoelectrons is measured with a small acceptance angle or with an angle resolving one- or two-dimensional parallel detection scheme.

Electron excitation by an electric field: The interaction between an electron and a time-dependent vector field $\mathbf{A}(\mathbf{r}, t)$ in the non-relativistic case is described by the Schroedinger equation

$$i\hbar\frac{\partial}{\partial t}\psi(\mathbf{r},t) = \Big[\frac{1}{2m}\big(\frac{\hbar}{i}\nabla - \frac{e}{c}\mathbf{A}(\mathbf{r},t)\big)^2 + V(\mathbf{r})\Big]\psi(\mathbf{r},t) = H\psi(\mathbf{r},t), \tag{2}$$

where $\psi(\mathbf{r}, t)$ is the wave function of the electron and $V(\mathbf{r}, t)$ the non-perturbated potential. Assuming $H = H_0 + H_{int}$ the hamiltonian H splits into an unperturbated part $H_0 = -\frac{\hbar^2}{2m}\Delta\psi + V(\mathbf{r})$ and an interaction term H_{int}. By neglecting the terms $divA$ (gauge invariance) and $|\mathbf{A}|^2$ (for weak electric fields), one obtains for the interaction hamiltonian H'_{int}:

$$H'_{int} = -\frac{e\hbar}{imc}\mathbf{A}\cdot\triangle = -\frac{e}{mc}\mathbf{A}\cdot\mathbf{p}$$

The vector potential $\mathbf{A}$ can be described as a plane wave $\mathbf{A} = A_0 \cdot \varepsilon \cdot exp\big[i(\mathbf{k}\cdot\mathbf{r} - \omega t)\big]$, where ε is the polarisation and $\mathbf{k}$ the wave vector of the light. Time dependent perturbation theory provides the transition rate W_{if} between an initial state $\psi_i(\mathbf{r}, t)$ (before the excitation) and a final electronic state $\psi_f(\mathbf{r}, t)$ (after the excitation) by Fermi's golden rule:

$$W_{if} \propto \sum_{i,f} \frac{2\pi}{\hbar}|\langle\psi_i|H'_{int}|\psi_f\rangle|^2\delta\big(E_f - E_i - h\nu\big) \tag{3}$$

The δ-function ensures energy conservation in the allowed transitions. If the wavelength $\lambda(\approx 100$ nm) of the incident photons is much larger than the lattice constant $a(\approx 0.1$ nm) of the

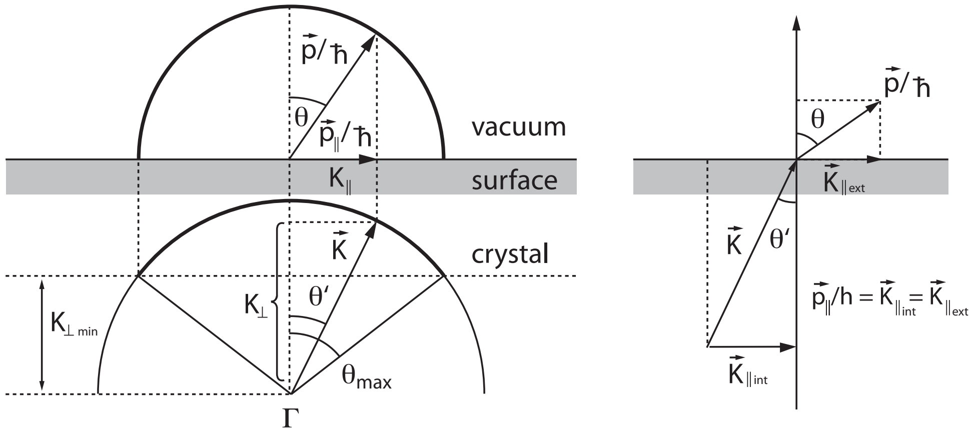

Figure 1: *Left-hand side*: Escape condition for excited photoelectrons with momentum $\mathbf{K}$ inside and $\mathbf{p}/\hbar$ outside of the crystal. *Thick solid* lines represent the internal and the external escape cones, respectively. *Right-hand side*: The crystal-vacuum interface and the corresponding momentum conservation relations. The parallel momentum $\mathbf{K}_{||}$ of electrons is conserved while transversing the surface barrier and escaping into the vacuum. Pictures are adapted from Ref. [20].

material containing the electrons (dipole approximation), the vector potential is assumed to be constant in space. Therefore the transition rate becomes proportional to the incident light intensity $I = |\mathbf{E}|^2 \propto A_0^2$:

$$W_{if} \propto A_0^2|\langle\psi_i|\varepsilon\cdot\mathbf{p}|\psi_f\rangle|^2 \propto A_0^2\varepsilon\cdot|\langle\psi_i|\mathbf{r}|\psi_f\rangle|^2 \propto \mathbf{I} \tag{4}$$

2.1.1 Angle-resolved photoelectron spectroscopy (ARPES)

Fermi's golden rule in Eq. 3 with the proper initial ψ_i and final state functions ψ_f contains all the physics of the photoemission process in an accurate *one-step model*. Though it cannot be solved rigorously without various approximations. However a completely phenomenological *three-step model* is much more intuitive, and despite its many simplifying assumptions, has proved to be successful for the description of various experimental data. In the three-step model the photoemission process is subdivided into three steps [20]:

- *First*, the electron is optically excited in the solid, in a momentum[3] and energy conserving transition from an initial state $|i\rangle$ with energy $E_i(\mathbf{k}_i)$ to a final state $|f\rangle$ with $E_f(\mathbf{k}_f)$.

- *Second*, the excited electrons with a $K_\perp$ component parallel to the surface normal eventually reach the surface. Electron-electron scattering processes predominantly determine the mean free path of the photoexcited electrons, leading to an inelastically scattered secondary electron distribution.

---

[3] The momentum of the photons for UV photonenergies can be neglected. Thus momentum conservation is fulfilled with $\mathbf{k}_i = \mathbf{k}_f$ in the reduced and with $\mathbf{K}_i = \mathbf{k}_f + \mathbf{G}$ in the extended brillouin zone scheme, where $\mathbf{K}$ is the wave vector of the optically excited electron in the solid and $\mathbf{G}$ denotes a reciprocal vector of the lattice.

- *Third*, part of the excited final state electrons $|f\rangle$ have sufficient kinetic energy $E(K_\perp)$ to overcome the surface potential barrier and being emitted into the vacuum. For the escape into vacuum they have to satisfy the condition: $(\hbar^2/2m)K_\perp^2 \geqslant E_{vac}$-$E_0$, whereas E_{vac} is the vacuum energy, related to the workfunction Φ of the surface, and E_0 the valence band bottom energy, as schematically sketched in Fig. 1. Transmission through the surface leaves the parallel component $K_{||}$ of the electron momentum conserved. Thus the momentum conserving relation can be written as

$$|\mathbf{p}_{||}|/\hbar \;=\; \mathbf{K}_{||} \;=\; \frac{1}{\hbar}\sqrt{2m_e E_{kin}^{solid}}sin(\theta') \;=\; \frac{1}{\hbar}\sqrt{2m_e E_{kin}^{vac}}sin(\theta). \tag{5}$$

E_{kin}^{solid} and θ' characterize the excited final state electrons in the solid whereas the kinetic energy of the photoelectrons in vacuum E_{kin}^{vac} and the emission angle relative to the sample surface normal θ can be measured in an angle-resolved photoelectron spectroscopy (ARPES) experiment.

Since two-dimensional electronic systems, *i.e.* surface states, are only supposed to disperse along $\mathbf{K}_{||}$ their complete electronic band structure $A(E, \mathbf{K}_x, \mathbf{K}_y)$ can be obtained in ARPES experiments by measuring the photoemission intensity as function of E_{kin}^{vac} and the corresponding polar angle θ and azimuthal emission angles ϕ relative to the sample surface normal, on the outer escape sphere, drawn as solid line in Fig. 1. Both momentum components $\mathbf{K}_x$ and $\mathbf{K}_y$ parallel to the sample surface are conserved in the photoemission process and can be written in a handy form for daily ARPES experiments as

$$K_x(\AA^{-1}) \;=\; 0.5123\cdot\sqrt{E_{kin}^{vac}(eV)}\sin\theta\cos\phi\;; \qquad K_y(\AA^{-1}) \;=\; 0.5123\cdot\sqrt{E_{kin}^{vac}(eV)}\sin\theta\sin\phi. \tag{6}$$

The three-dimensional case is more complicated. From Eq. 5 follows Snell's law for electron refraction at the crystal-vacuum potential barrier, with $E_{kin}^{vac} = E_{kin}^{solid}$-$E_0$, as

$$\sin(\theta') \;=\; \sin(\theta)\frac{(E_{kin}^{vac})}{(E_{kin}^{vac}+E_0)} \tag{7}$$

and therefore

$$\mathbf{K}_\perp \;=\; \frac{1}{\hbar}\sqrt{2m_e(E_{kin}^{vac}+E_0)}\cdot cos(\theta'). \tag{8}$$

Thus the assignment of a dispersion relation $E(\mathbf{K}_\perp)$, *i.e.* from three-dimensional bulk states, requires information about the inner potential E_0 of the crystal, which is often not directly available. Comparison between measured and calculated band structures may lead to the correct value of E_0.

2.1.2 Time-resolved two-photon photoelectron spectroscopy (TR-2PPE)

Light sources, providing photons with energies below the work function and intensities high enough to make multi-photon processes probable can lead to observable signals of unoccupied electronic states in the energetic range between the vacuum level E_{vac} and the Fermi level E_F. In contrast,

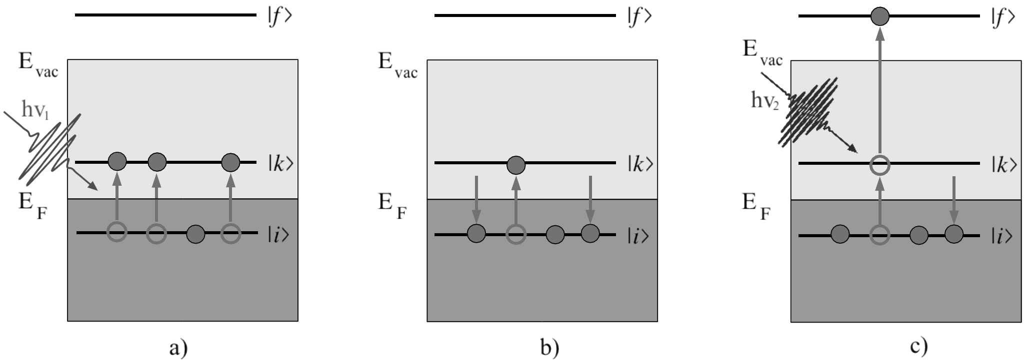

Figure 2: The basic principle of 2PPE as described in the text. (a) Pump pulse $h\nu_1$ excites the electrons from an initial state $|i\rangle$ to an intermediate state $|k\rangle$. (b) Relaxation process by electron-hole recombination. (c) Probe pulse $h\nu_2$ promotes a part of the electrons from the intermediate state $|k\rangle$ to the final state $|f\rangle$.

conventional photoelectron spectroscopy is solely sensitive for occupied electronic states below E_F.

The basic principle of time-resolved two-photon photoemission (TR-2PPE) can be described the following way:

- A first femtosecond laser pulse (pump pulse) excites electrons out of an occupied initial state $|i\rangle$ into an intermediate state $|k\rangle$ by absorption of one photon with energy $h\nu_1$, sketched in Fig. 2 (a).

- After excitation by the pump pulse, the electrons in the intermediate state $|k\rangle$ relax by means of different elastic and inelastic scattering processes, listed according to their timescales and described in detail in Sec. 5.3.1. They can be pooled together into a lifetime of the involved intermediate state, which is conventionally called population relaxation time τ.

- The second light pulse (probe pulse) arrives after a defined time delay Δt after the first pulse and excites a part of the electrons from the intermediate state $|k\rangle$ to the final state $|f\rangle$ above the vacuum level E_{vac} by absorbing a photon $h\nu_2$, shown in Fig. 2 (c). The detected kinetic energy and emission angle of the photoelectrons in the analyzer lead by calculation to the binding energy (and momentum) of the electrons in the solid, for initial and intermediate states:

$$E_i = h\nu_1 + h\nu_2 - E_{kin} - \Phi \qquad and \qquad E_k = E_i + h\nu_1.$$

The optical Bloch equations describe the three steps of such a 2PPE process in an analytical way, discussed more detailed in Sec. 5.3.1. Note that in principle three different excitation mechanisms can be distinguished:

- *Resonant excitation* occurs when the binding energy difference E_i-E_k between initial $|i\rangle$ and

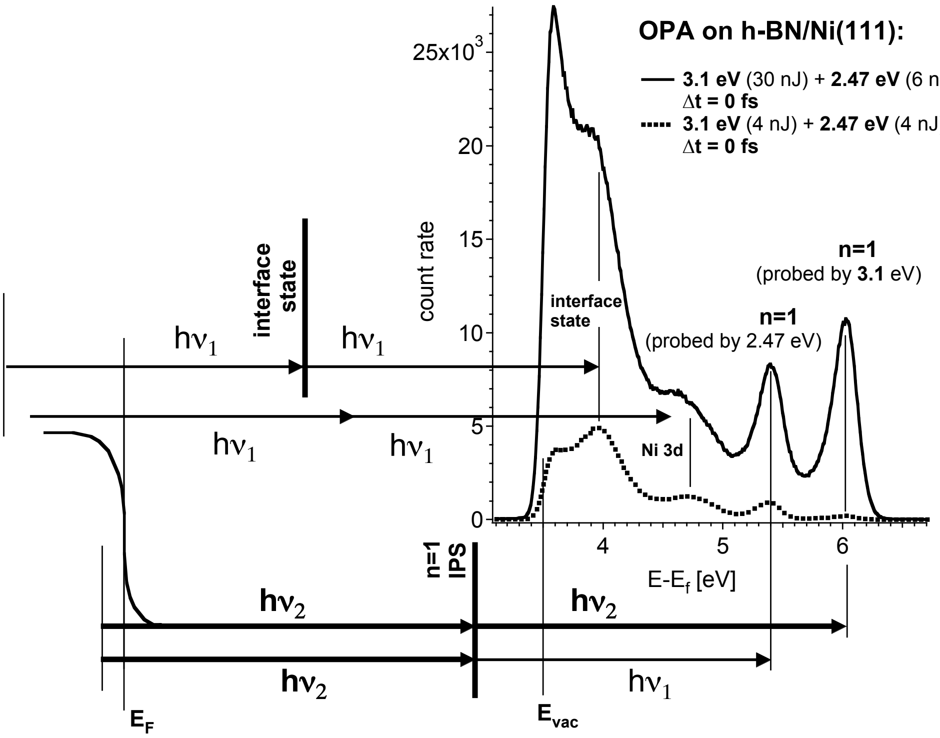

Figure 3: Bichromatic 2PPE spectra from *h*-BN/Ni(111) for temporal coincidence between the two pulses $h\nu_1 =$ 2.5 eV and $h\nu_2 = 3.1$ eV. Three resonant transitions in the high fluence regime ($h\nu_2$: 30 nJ): $h\nu_2$ - $h\nu_2$ and $h\nu_2$ - $h\nu_1$ transition via the image potential state (IPS) as well as $h\nu_1$ - $h\nu_1$ via the interface state. At 4.7 eV a $h\nu_1$ - $h\nu_1$ direct 2PPE excitation from initial states in the Ni 3*d*-band via an virtual intermediate state is observed. In the case of a reduced $h\nu_2$ fluence (4 nJ) the $h\nu_2$ - $h\nu_2$ IPS transition and hence the amount of inelastically scattered electrons around 4 eV above E_F are drastically reduced. A distinct $h\nu_1$ - $h\nu_1$ transition via the interface state becomes clearly visible.

intermediate state $|k\rangle$ exactly matches the pump pulse photon energy $h\nu_1$, often represented as pronounced peaks in the experimental spectra, as shown in Fig. 3.

- *Non-resonant* excitation is typical for a continuous distribution of initial states combined with a continuous distribution of intermediate states. A distinct intermediate state $|k\rangle$ from this continuum is eventually populated via inelastic scattering from another intermediate states at higher energy and different $\mathbf{k}_{||}$ by means of inter- and intraband scattering processes.

- Direct 2PPE via a *virtual intermediate* state can be regarded as simultaneous absorption of two photons at the same time. The nonlinearity of this process, as shown in Eq. 9, requires strong laser field intensities *i.e.* a reasonable amount of photons per short laser pulse duration.

Experimental examples of resonant and non-resonant 2PPE as well as direct 2PPE via an virtual intermediate state are *e.g.* obtained within the same bichromatic spectrum from a *h*-BN/Ni(111) surface, shown in Fig. 3. The energy scale refers to the final state energy of the photoelectrons with respect to the Fermi energy E_F. The peculiar peaks at 6 eV and 5.4 eV belong to a resonant 2PPE transition, initially pumped with $h\nu_2 = 3.1$ eV from the initial Ni 3*d*-bands via a discrete image potential state as intermediate state, symbolized by a bold vertical line, and subsequently probed by either $h\nu_2$ or $h\nu_1 = 2.5$ eV respectively. The rather weak feature around 4.75 eV is related to a direct 2PPE process from the initial Ni 3*d*-bands via a virtual intermediate state by simultaneous absorption of two times $h\nu_1$. Inelastically scattered secondary electrons and electrons from non-resonant 2PPE processes contribute to the strongly increasing exponential background towards lower final state energies. The spectrum is terminated by a so called low energy cut off at 3.5 eV, directly indicating the workfunction Φ of the sample surface.

Transition rate for 2PPE Second-order perturbation theory yields a rate W_{if} for simultaneous absorption of two photons with the energies $h\nu_1$ and $h\nu_2$ [21], given by:

$$W_{if} \propto \frac{I_1 \cdot I_2}{(\nu_f - \nu_i - \nu_1 - \nu_2)^2} \left| \sum_k \frac{M_{ik} \cdot \varepsilon_{\mathbf{1}} \cdot M_{kf} \cdot \varepsilon_{\mathbf{2}}}{(\nu_k - \nu_i - \nu_1)} + \frac{M_{ik} \cdot \varepsilon_{\mathbf{1}} \cdot M_{kf} \cdot \varepsilon_{\mathbf{2}}}{(\nu_f - \nu_k - \nu_2)} \right| \propto I_1 \cdot I_2 \tag{9}$$

The transition probability is proportional to the product of the light intensities $I_1 \cdot I_2$. $M_{ik,kf}$ is the matrix element $\langle \psi_{i,k} | \mathbf{r} | \psi_{k,f} \rangle$. Both matrix elements M_{ik} and M_{kf} have to be nonzero to give a non-vanishing transition probability W_{if}. The summation in the second factor extends over all intermediate levels ψ_k that are accessible by allowed one-photon transitions from the initial state ψ_i. The intermediate states can be discrete states, e.g. the Rydberg series of the image state potential in Fig. 3, as will be introduced in Sec. 4.1.4, or a continuum of states.

However, for a detailed overview over TR-2PPE the comprehensive review article by Petek *et. al.* [22] is highly recommended.

2.1.3 Time- and angle-resolved photoelectron spectroscopy (TR-ARPES)

Time- and angle-resolved photoemission spectroscopy (TR-ARPES) directly probes the transient non-equilibrium evolution of the occupied band structure after intense laser pulse irradiation. Hence TR-ARPES is the method of choice for investigating electronic, structural and magnetic phase transitions of solid state systems induced by intense infrared laser irradiation on a femtosecond time scale.

TR-ARPES obtains information about a single particle spectral function $A(E, k)$ in the energy or frequency domain, as conventional ARPES does. Furthermore the technique gains information about collective excitation modes in the time domain. Summarizing the informations from time- and frequency-domain leads to an extended spectral function $A(E, k, \Delta t)$.

Fig. 4 schematically illustrates the the experimental method of TR-ARPES. An intense infrared laser pulse with a typical fluence between 0.1 and 3 mJ/cm^2 excites the electronic system at delay 0 fs, leading to a coherent electron-hole population. This initial non-equilibrium population

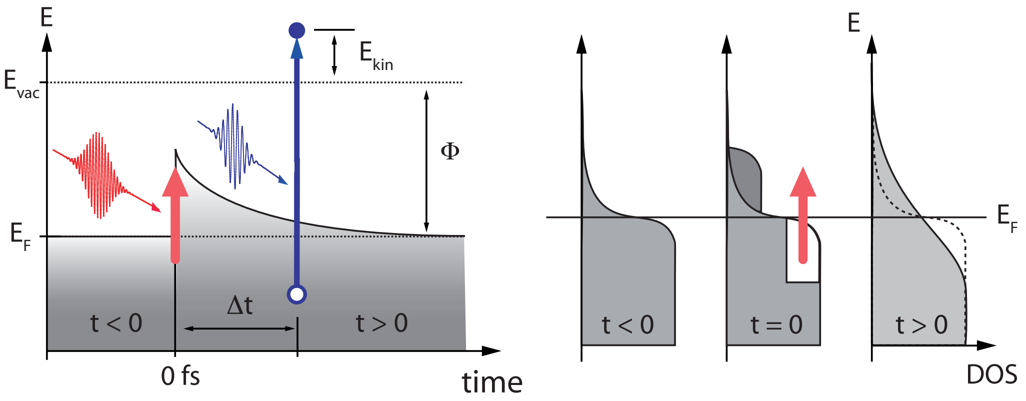

Figure 4: *Left-hand side*: The electronic system of a solid state surface is excited by means of a femtosecond infrared laser pulse at $t = 0$ fs. An UV pulse subsequently probes the transient non-equilibrium occupied band structure for variable time delays Δt after excitation. *Right-hand side*: Schematic illustration of thermalized equilibrium distribution at $t < 0$ fs, with a temperature T_{init}. Excitation by an infrared laser pulse leads to a non-equilibrium hot electron population at zero delay. Inelastic scattering processes on a femtosecond time scale thermalize the system, described by a final temperature $T_{final} > T_{initial}$.

decays by means of several elastic and inelastic scattering processes on a femto- and picosecond time scale. Sec. 5.3.1 contains a detailed description of these scattering processes. The transient dynamics of the occupied electronic structure and the excited hot electron population around E_F can then subsequently be probed for variable time delay Δt by means of direct photoemission with an UV femtosecond laser pulse at a photon energy $h\nu_2$ [4] larger than the sample surface workfunction Φ. The corresponding photoelectrons are measured in the four-dimensional parameter space by varying the time delay Δt between the pump and probe laser pulses, polar θ and azimuthal ϕ emission angles and kinetic energies of the photoelectrons, leading to an experimentally obtained extended spectral function $A(E, k_x, k_y, \Delta t)$.

2.1.4 Photoelectron detection

The photoemitted electrons were either analyzed in a hemispherical energy analyzer in a VG ESCALAB 220 [23] with its energy and angular resolution set to 50 meV and ±1°, respectively, or in an elliptical display analyzer (EDA) in a separate vacuum chamber, both schematically shown in Fig. 5. A detailed description of the non-commercial EDA detector will be given in chapter 3. All spectra measured in the hemispherical analyzer with laser pulses at low photon energies (between 1.55 eV and 6 eV) were taken with a bias voltage between -3 V and of -10 V, applied to the sample with respect to the analyzer in order to avoid the low-transmission regime of the analyzer at low kinetic energies [24]. Consequently the released photoelectrons follow bended trajectories

---

[4] or with $2\times h\nu_2$ for a direct 2PPE probing process with two photons from the same probe pulse

and based on an electrostatic model the true emission angle at the sample θ_e can be obtained from the manipulator angle θ_m by [24]

$$\theta_e = \theta_m + \arctan\left(\frac{eU\,(1-\sin\theta_m/\theta_m)}{E_{kin} - eU\,(1-\sin\theta_m/\theta_m)}\right)^{1/2}, \tag{10}$$

whereas E_{kin} denotes the kinetic energy of the photoelectrons at the sample surface. Furthermore the total number of photoelectrons per pulse has been determined by measuring the sample current with a pico amperemeter (Keithly 6487).

2.1.5 The light pulses

The light pulses were produced by a commercial femtosecond oscillator (Coherent Mira Seed; 76 MHz) and amplified in a high repetition rate (250 kHz) regenerative pulse amplifier (RegA 9050). On the sample, the pump pulses (800 nm; 1.55 eV) were either *s*-polarized[5] in order to create a hot electron gas above the Fermi level [25], while minimizing the IR photoemission background, or *p*-polarized[6] in order to allow multi photon transitions, both due to dipole selection rules [26]. The probe pulses (400 nm; 3.1 eV) were produced by frequency-doubling in a 0.5 mm thick β-barium borate (β-BaB$_2$O$_2$) crystal and the group velocity dispersion was compensated in a prism sequence. The second harmonic (SH) probe light was *p*-polarized in order to excite electrons from unoccupied intermediate states into final free electron states in the vacuum. The pulse widths were 108 fs and 70 fs at the sample position for the fundamental and the second harmonic, respectively. If the probe process is a second-order two-photon-photoemission process (as in Sec. 4.6 and Sec. 5.4), this leads to a probe pulse width of $70/\sqrt{2} \approx 50$ fs, and, thereby, to an overall cross-correlation width of 119 fs [27].

For TR-2PPE and TR-ARPES experiments the fundamental 800 nm pulses were delayed on a computer controlled delay stage. Both light beams were focused onto the sample inside a VG ESCALAB 220 [23] ultrahigh vacuum photoemission chamber [23] by a lens of 300 mm focal length, which produced a spot with a beam waist of 100 μm. The pump fluence of the fundamental was choosen up to 3 mJ/cm^2 on the sample for TR-ARPES experiments, which corresponds for Ni to 140 nJ ($5.6 \cdot 10^{11}$ photons) absorbed pump energy per pulse in the probed volume [7]. Subsequent probing of the transient electronic structure by means of direct 2PPE (2×3.1 eV; 2×400 nm) via a virtual intermediate state or resonant 2PPE via an unoccupied intermediate state with two photons from the same second harmonic (SH) pulse has been performed for variable time delays Δt.

---

[5] *s*-polarized: the electrical field vector is polarized perpendicular to the plane of incidence.

[6] *p*-polarized: the electrical field vector is polarized in the plane of incidence.

[7] For the calculations the following optical constants have been used: reflectivities at 30° incidence for 400 nm 0.74 (*s*-polarized) and 0.66 (*p*-polarized), for 800 nm 0.85 (*s*-polarized) and 0.81 (*p*-polarized); an absorption volume which corresponds to a cylinder with a waist of 100 μm and a penetration depth of 140 Å (for 800 nm); refractive indices for nickel are 2.49 (800 nm) and 1.6 (400 nm); absorption coefficients (imaginary parts of the refractive indices) for nickel are 4.45 (800 nm) and 2.4 (400 nm). Values are from www.ioffe.ru.

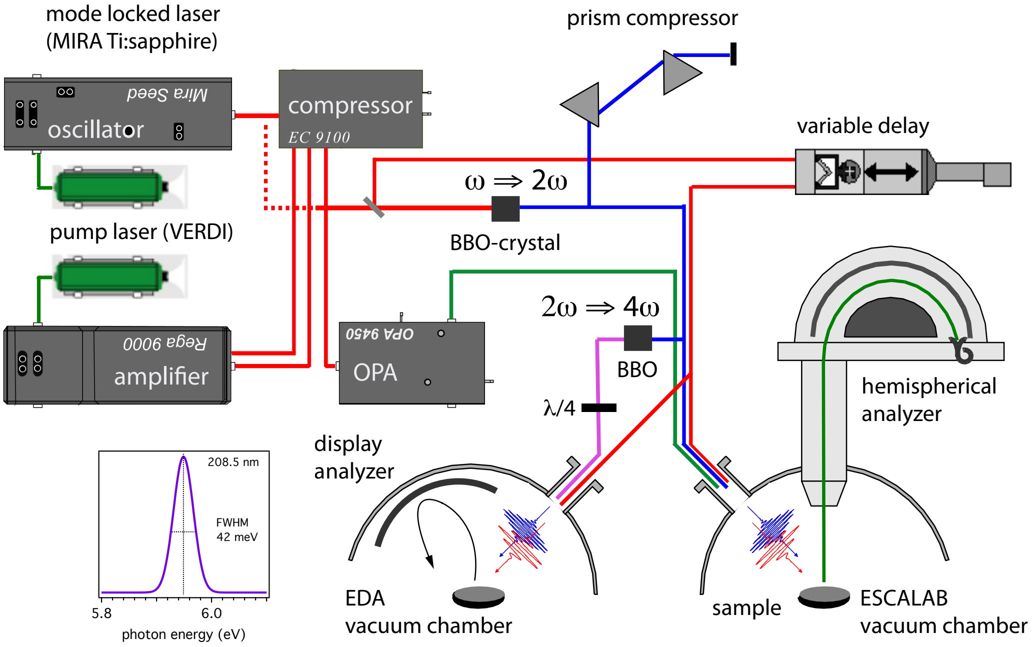

Figure 5: Schematic experimental setup for TR-PES experiments. Optionally one can proceed TR-PES experiments either by using the RegA amplifier (*filled red line*) or only with the MIRA oscillator (*dotted red line*). *Inset*: Optical spectrum of the fourth-harmonic pulses measured with a commercial Ocean Optics spectrometer.

The time-zero pump-probe delay was defined by taking the maximum of the cross-correlation curve from a poly crystalline Ag surface for a hot electron distribution at E-E_F = 1.45 eV where the lifetimes of the intermediate states were previously found to be shorter than 5 fs [28]. Note that for high infrared fluences $F > 1$ mJ/cm^2 a considerable amount (more than 1%) of the conduction band electrons near E_F is transiently populated. This reduces the available relaxation phase space for the hot electrons at higher excess energies and hence increases their life times, leading to an asymmetric cross-correlation. At excitation densities in the order of several mJ/cm^2 such a broadening and shift of the cross-correlation maximum has to be considered for time-zero determination even for large energy values E-E_F above the Fermi level.

In order to avoid space-charge effects only caused by the probing SH pulse the intensity of the blue pulse has been reduced such as that any spectral distortions caused by mutual Coulomb repulsion between the emitted photoelectrons are below the energy resolution of the electron analyzer (10 meV). Background contributions by 4PPE from the 1.55 eV pulse in the spectral region of transient changes around E_F at $E_{kin} = 2\times 2h\nu$ - Φ were found to be weak compared to the probing 2PPE intensity from the 3.1 eV pulse and thus can be neglected.

In order to explore resonant excitations of unoccupied intermediate states (e.g. in Sec. 4.2) the amplified fundamental pulses have been shifted in wavelength (between 460 nm and 530 nm) by means of an optical parametric amplifier (OPA 9450) [29].

The circular dichroism experiments in this work have been performed with the elliptical display analyzer (EDA) at low photon energies, using the fourth harmonics of the amplified Ti:sapphire pulses. The fourth harmonic at 5.95 eV photon energy has been obtained by two times consecutive second harmonic generation (SHG) in the 500 μm and an additional 100 μm thick nonlinear β-barium borate crystal, as schematically shown in Fig. 5 and described in detail in Ref. [30]. Therefore the RegA output has been set to 1.49 eV (830 nm). The optical spectrum of the 5.95 eV pulses with an energy width ΔE_{FWHM} of 42 meV and a central wavelength of 208.5 nm has been characterized with a commercial Ocean Optics spectrometer, exemplarily shown in the inset of Fig. 5. Finally a rotatable $\lambda/4$-plate allows to manually switch between the two different circular polarizations of opposite helicity as well as linear p-polarization respectively, before focussing the beam by means of an UV-fused silica lens through a $\mathrm{SrF_2}$ window into the EDA, onto the sample surface.

3 Elliptical display analyzer EDA

3.1 Motivation: Parallel detection scheme for time resolved photoemission

The experimental main topic of this thesis was the commissioning and optimization of an ellipsoidal display analyzer (EDA) for time-resolved photoelectron spectroscopy at low photon energies.
The EDA has been built by Dütemeyer *et al.* [2, 3] at the Physics Institute, at the University of Dortmund and is an improved version of the design of Eastman *et al.* [1]. This instrument measures angle-resolved photoelectron intensity distributions at fixed energy $I(\theta,\phi)|_{E\,=\,const}$ for rather large acceptance angles of $\delta\theta = \pm 43^\circ$ and $\delta\phi = 360^\circ$ where θ denotes the polar and ϕ the azimuthal angle. Since both in-plane electron momenta $p_x = \hbar k_x$ and $p_y = \hbar k_y$ are determined simultaneously for fixed kinetic energy in a single shot, no rotation of the sample relative to the detector coordinates is required.
Two main advantages arising from such a detection scheme for time- and angular-resolved photoemission spectroscopy (TR-ARPES) experiments are: $First$ no rotation of the sample surface and *second* the parallel data acquisition.
The angle between the incident polarization vector **A** and the crystal symmetry axes of the surface remains constant for all detected electron momenta. Since in the one-electron picture the efficiency of a specific photoemission process with initial state i and final state f depends on the squared matrix element, given in the dipole approximation by $t_{fi} = \langle f|\mathbf{A}\cdot\nabla|i\rangle$, the photoemission intensity $I(\theta,\phi)|_{E=const}$ can be written as

$$I(\theta,\phi,E_f) \propto w_{fi}(k_x(\theta,\phi),k_y(\theta,\phi)) = |t_{fi}(k_x,k_y)|^2\delta(E_f - E_i - h\nu) \tag{11}$$

Thus with a polarization vector **A** fixed with respect to all electron momenta k_x and k_y acquired in parallel, the photoemission intensity $I(k_x,k_y)$ only depends on the specific nature of the states i and f and not on the detection geometry. In contrary, in ARPES experiments using a fixed hemispherical analyzer and small acceptance angles $\delta\theta$ and $\delta\phi$, the two-dimensional (2D) surface Brillouin zone (SBZ) has to be mapped by sequentially rotating the sample in polar (θ) and azimuthal (ϕ) direction. Thereby the polarization **A** varies for different emission angles and electron momenta k_x and k_y modulating t_{fi} and $I(k_x,k_y)$. The influence of these so called matrix-element effects in the photoelectron intensity distributions can be avoided by the use of 2D parallel detection schemes like the one described in this chapter. This has been done *e.g.* in circular dichroism in the angular distribution (CDAD) experiments by Schönhense *et al.* [31] or in the observation of circular dichroism in photoelectron diffraction patterns by Daimon *et al.* [32], by the use of a display-type spherical-mirror analyzer [33].
The second advantage is the short data acquisition time owing to parallel detection scheme of the EDA. For comparison in a single-channeltron analyzer the angular resolution $\Delta\theta$ and $\Delta\phi$ are in the order of the acceptance angle $\delta\theta = \delta\phi = 1^\circ$. The fraction of detected photoelectrons ϵ can be approximated by [2, 3]

$$\epsilon \approx \int\limits_{\delta\phi}\int\limits_{\delta\theta} \frac{\sin(\theta)\,d\phi\,d\theta}{2\pi}\left(\frac{\Delta E}{h\nu - \Phi}\right) \approx \left(\frac{1^\circ}{90^\circ}\right)\left(\frac{1^\circ}{360^\circ}\right)\frac{0.2}{2} \approx 3\cdot 10^{-6}. \tag{12}$$

Where ΔE denotes the energy band pass and $h\nu - \Phi$ the width of the photoemission spectrum in energy depending on the photon energy $h\nu$ and the sample surface workfunction Φ. A typical value for $h\nu$ is 6 eV, corresponding to the photon energy of the fourth-harmonic of an Ti:Sapphire oscillator and a workfunction energy between 4 eV and 5 eV for common metal surfaces [20]. The resulting detector efficiency in the order of 10^{-6} is three orders of magnitude smaller than the one of the EDA, given by [2,3]

$$\epsilon_{EDA} \approx \int_0^{2\pi}\int_0^{43^\circ} \frac{\sin(\theta)\, d\phi\, d\theta}{2\pi} \left(\frac{\Delta E}{h\nu - \Phi}\right) T \approx \cos(\theta)|_{43^\circ}^{0^\circ} \left(\frac{0.2}{2}\right) (0.81)^8 \approx 5 \cdot 10^{-3}.$$

In the case of the EDA the finite transition probability T of the photoelectron through the 7 hemispherical gold grids is $T = (0.81)^8$ where the finite transmission $T_i = 0.81$ of each grid is taken into account. Owing to the factor ϵ/ϵ_{EDA} the data acquisition time for constant energy cuts through the complete SBZ is faster by three order of magnitudes for an elliptical display analyzer than for a hemispherical single-channeltron analyzer. Regarding time-resolved Fermi surface mapping experiments, where the temporal resolution increases the parameter space by one extra dimension, such a parallel detection scheme is invaluable. Furthermore, the EDA is adequate for delicate surface studies because the short experimental acquisition time helps to avoid surface contamination.

3.2 Detection principle and analyzer settings

The EDA basically consists of four main parts: a spherical pre-retardation stage, an ellipsoidal low-pass mirror, a hemispherical high-pass filter and a detection unit, schematically drawn in Fig. 6. Photoelectrons are excited by either pulsed laser light at low photon energies through a small hole from one side or UV light from a He-discharge lamp from the other side, in the horizontal plane and at an incidence angle of 56° with respect to the sample surface normal. The sample itself is located in the upper focal point of the ellipsoidal mirror M_{0-2}.

Photoelectrons emitted inside a cone of $\pm 43^\circ$ are then electrostatically reflected at the ellipsoidal mirror segments M_0, M_1 and M_2 and focussed towards the lower focal point of the ellipsoid. The ellipsoidal mirror acts as a low-pass filter since electrons with kinetic energies higher than E_{pass} hit the mirrors and are absorbed. Since the electrical field component perpendicular to the mirror surface is crucial for the reflection, shown in Fig. 13 (b), all the electrons with an incident angle of $\eta(\theta)$ relative to the mirror normal and kinetic energy less than $E_{pass} = eU_M \cdot cos(\eta(\theta))^2$ are reflected back towards the lower focal point. A small aperture of typically 1.5 mm diameter in the lower focal point of the ellipsoid discriminates the proper photoelectron trajectories, exemplarily marked as three black lines in Fig. 6, from stray electrons and enhances the angular resolution of the system. The aperture is subsequently followed by a high-pass filter unit, composed of three concentric gold grids. The applied voltage U_{G_5} at the center grid G_5 closes the bandpass ΔE and cuts off the photoelectrons with less kinetic energy than E_{pass} - ΔE as shown in Fig. 7. The last part of the analyzer is the detector made up of a planar stack consisting of a flat grid G_7,

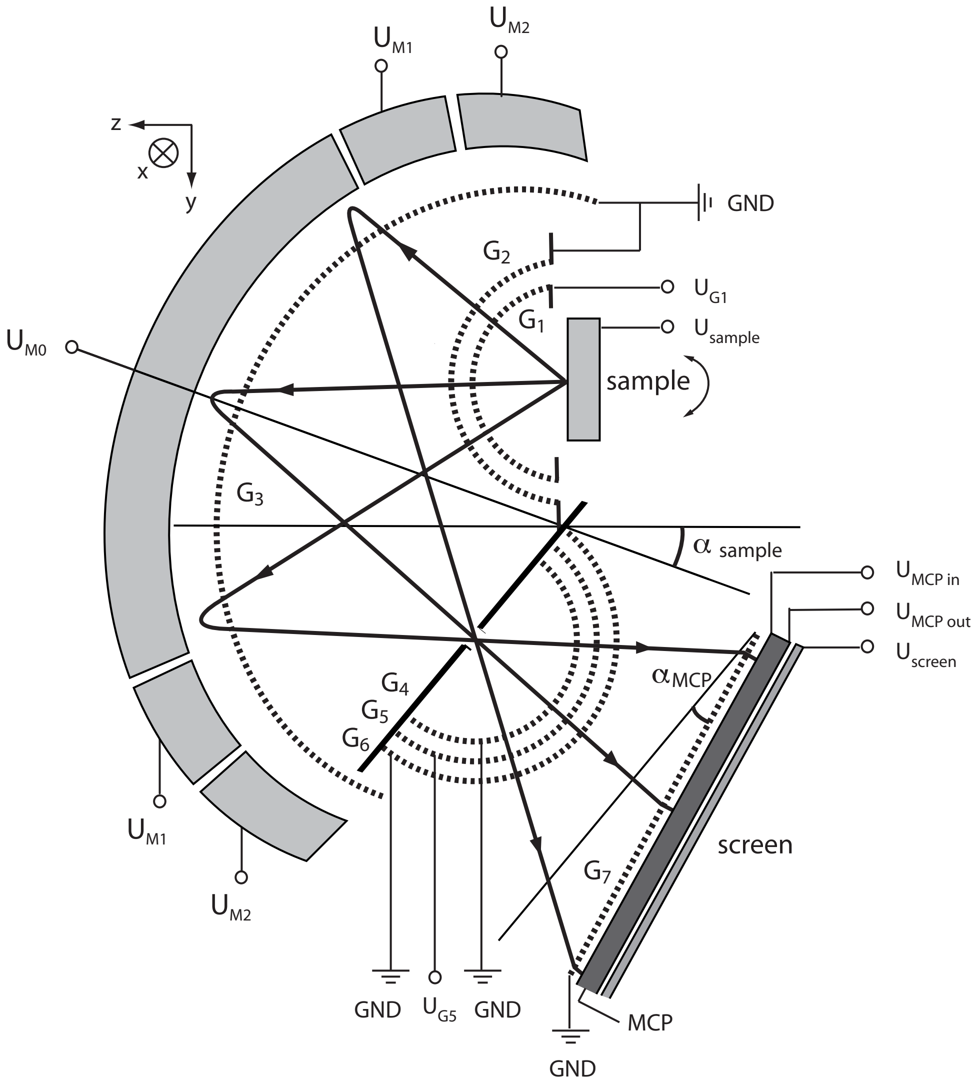

Figure 6: Drawing showing the operation principle of the ellipsoidal display analyzer with the main components: the sample position in the upper focal point, the pre-retardation stage G_1, the ellipsoidal low-pass mirror M_0, M_1 and M_2, the aperture in the lower focal point, the high-pass filter G_5, and the detector stack composed of a micro-channel plate (MCP) and a phosphor screen.

a micro-channel plate (MCP) [8] and a phosphorous screen. Accelerated up to typically 0.2 kV between the planar G_7 and the input of the MCP the electrons are amplified by a factor of 10^4 while passing the MCP with an applied potential difference of 1 kV. The amplified photoelectron cascade is then further accelerated up to 3.6 kV between the MCP exit and the screen, causing phosphorescent light on the screen which finally can be recorded by means of a charge-coupling-device [9] (CCD) outside of the vacuum chamber. U_{G_2}, U_{G_3}, U_{G_4}, U_{G_6} and U_{G_7} are set to ground

---

[8] single MCP, $1.7 \cdot 10^4$ amplification factor

[9] pixelfly CCD: 936×936 pixels, 12 bit dynamic range

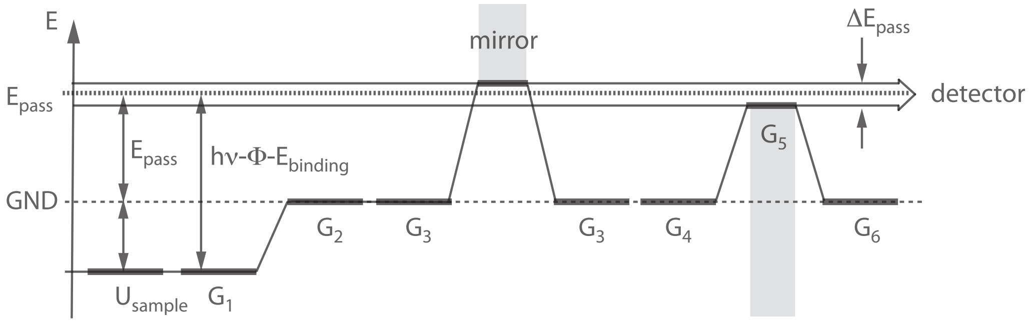

Figure 7: Energy scheme of the applied analyzer voltages, according to Table 1.

Component	Radius of curvature (mm)	Tilt angle	Applied voltage w.r. to GND
Sample	∞	0	$-E_{pass} \leqslant U_{sample} \leqslant h\nu$-$E_{pass}$
G_1	24.5	0	$U_{G1} = U_{sample}$+$\Delta\Phi$
G_2	28.0	0	GND
G_3	$x_{G3} = z_{G3} = 91.67$; $y_{G3} = 94.0$	12.47°	GND
Mirror	$x_M = z_M = 99.3$; $y_M = 102.0$	12.47°	$U_M = E_{pass}/cos(\eta)^2 = 1.055 \cdot E_{pass}$
G_4	41.0	6.2°	GND
G_5	47.97	6.2°	$U_{G5} = E_{pass}(1 - 1/r_A^2 - \Delta E)$
G_6	57.8	6.2°	GND
G_7	∞	14.62°	GND
MCP	∞	14.62°	$U_{in} = 0.2$ kV; $U_{out} = 1.2$ kV
Screen	∞	14.62°	$U_{screen} = 3.6$ kV

Table 1: Summary of the applied analyzer potentials, the radii of the distinct detector components as well as their tilt angle with respect to the axis of curvature (x-direction in Fig. 6).

ensuring a field-free transmission in straight trajectories between the distinct analyzer parts. The applied analyzer potentials are summarized in Tab. 1.

Finally, sequential variation of U_{sample} and U_{G_1} between $h\nu - E_{pass}$ and $-E_{pass}$ leads to complete data stacks in relative short data acquisition time, providing the three-dimensional momentum- and energy-resolved photoelectron intensity distribution $I(E_B, k_{||})$ and thus the electronic structure of the studied system. In order to vary the kinetic energy of the photoelectrons two spherical Grids G_1 and G_2 are centrically mounted in front of the sample, forming a pre-retardation stage. Changing the voltage of the sample U_{sample} and of the first Grid U_{G_1} allows to change the kinetic energy of the photoelectrons at constant pass energy E_{pass} and thus to keep the transmission function of the EDA constant.

Angle-integrated spectra can be recorded either from the measured screen current by means of a special nanoampere meter which can be operated at high voltages or by numerical integration of the detector signal on the CCD.

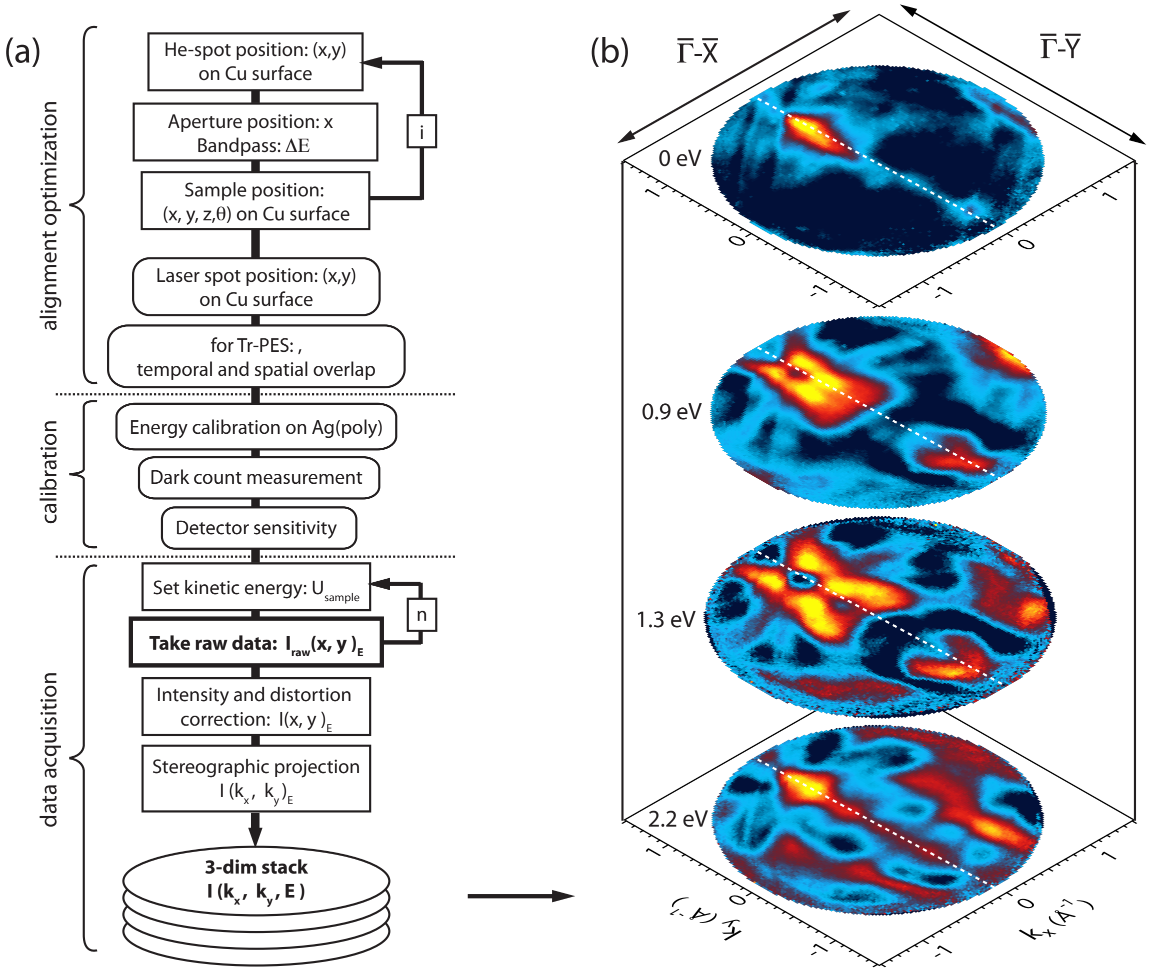

Figure 8: (a) Flow chart illustrating the EDA detector alignment and the data acquisition procedure, including calibrations and detector sensitivity corrections, leading to a three-dimensional stack of constant energy snap shots $I(k_x, k_y, E_{binding})$, as shown exemplarily for the Bi(114) surface in (b). Note the Fermi surface map on top of the stack, revealing the one-dimensional surface state of Bi(114) along $\overline{\Gamma}$-$\overline{Y}$, highlighted by a *dashed white* line.

3.3 Measurement and data processing strategy

This section describes the data acquisition procedure and the subsequent data processing, summarized in the flow chart in Fig. 8.

So as to accurately image the two-dimensional cut $I(k_x, k_y)$ through the SBZ, both the spot of the light source as well as the sample surface have to match exactly the upper focal point of the ellipsoid. Furthermore the aperture has to be accurately positioned on the lower focal point, otherwise angular distortions would lead to a discrepancy between the detected $I(\theta, \phi)|_{E=const}$ and the $I(k_x, k_y)$ of the given sample surface in the case of a mismatch in z- and y-direction on one hand. On the other hand a slight mismatch with respect to the upper focal point in x-direction,

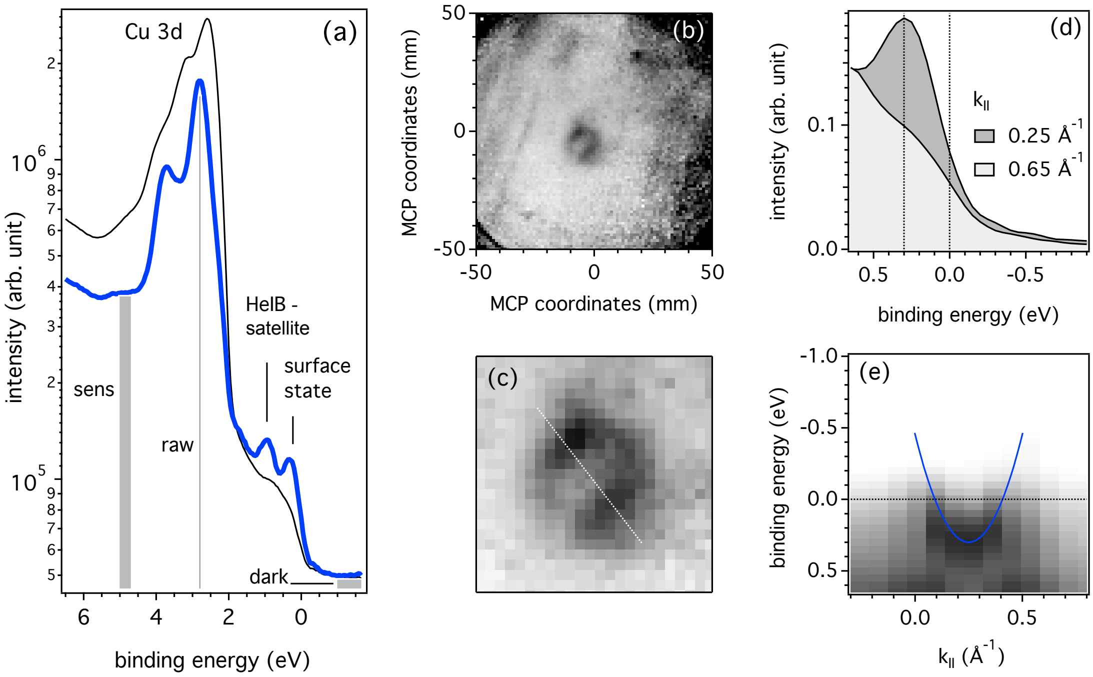

Figure 9: (a) Angle-integrated (*thin line*; ± 43°) and angle-resolved (*bold line*; ± 3°) valence band spectrum of Cu(332) close to $\overline{\Gamma}$, measured with $h\nu = 21.21$ eV. Note the logarithmical intensity scale. (b) Fermi surface map of Cu(332) for a pass energy of 10 eV and 15 s data acquisition time. High intensities are given in darker grey. (c) Zoom on the Shockley surface state at the center of the SBZ. (d) Angle-resolved photoemission spectra around E_F, for two different $k_{||}$ along $\overline{\Gamma}$-$\overline{M}$, revealing the binding energy maximum of the Shockley surface state at 300 meV. (e) Energy versus momentum cut along the *dashed line* in (c) and corresponding parabolic fit (*solid line*) of the dispersing surface state.

parallel to the optical axis of the mirror, would seriously lower the angular resolution and increase the signal-to-noise ratio.

The positioning of the sample, the light spot and the aperture is an iterative process. A first alignment on a well known surface electronic structure such as the Shockley surface state of a copper surface is helpful. This is followed by angular resolved analyzer normalization measurements as well as energy calibration measurements which are executed on a Ag(poly) sample.

During the whole data acquisition including the taking of a detector sensitivity map and the energy calibration measurements all the detector voltages and hence the pass energy are kept constant, except for U_{sample} and U_{G1} which allow to scan the probed kinetic energy of the photoelectrons. The whole alignment procedure can be subdivided into the following steps, according to the flow chart in Fig. 8.

1. The alignment procedure starts with the calibration of the sample position relative to the detector and to the direction of the incident light source using first the He-lamp and second the laser beam followed by the adjustment of the aperture position. The iterative adjustment

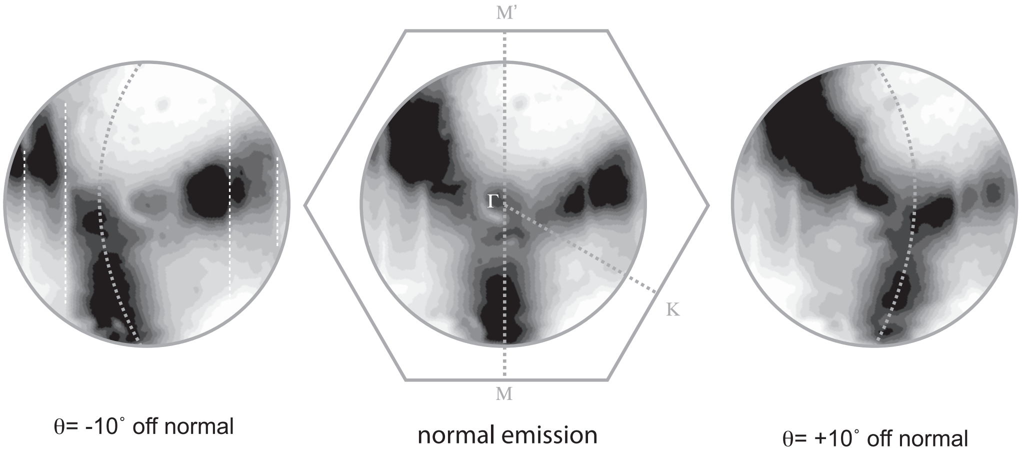

Figure 10: Constant energy cuts from the bulk 3d bands projected on a Cu(332) surface, measured with $h\nu = 21.21$ eV at a pass energy of 10 eV, at a binding energy of 3.5 eV and 20 s exposure time per snapshot. *Left-hand side* for $\theta =$ -10° off normal, *central image* for normal emission and *right-hand side* for $\theta = +10°$ off normal. *White dashed lines* mark the segmentation of the ellipsoidal mirror.

steps are first performed by optimizing the sample current I_{sample}, second by optimizing the angle integrating screen current I_{screen}[10] and finally third by monitoring the angular distribution of the Cu(332) Shockley surface state (Fig. 9). The energy calibration is based on the well known band structure of the Cu(332) surface together with the Fermi edge of the poly crystalline Ag surface.

2. Measurement of the three-dimensional stack of photoelectron intensity distributions $I_{raw}(x, y, E_B)$ at an analyzer pass energy of typically 9 eV, by taking snapshots ranging from 1 s to 90 s data acquisition times for the chosen values of kinetic energy.

3. Dark count subtraction and detector normalization: A fixed background $I_{dark}(x, y)$ is measured above E_F, caused by read-out noise of the CCD-chip, stray light on the CCD in the visible range generated by the pulsed laser light source and dark counts. Inhomogeneities in the amplification of the MCP, position dependent variations of the phosphor efficiency on the screen as well as spatial transmission differences of the seven gold grids have to be corrected from the raw data. In order to account for that $I_{sens}(x, y)$ has to be measured in a spectral region with less band structure where inelastically scattered secondary electrons average out all the angle-resolved information from the specific electronic structure of the sample, as illustrated with *vertical grey bars* in Fig. 9 (a). Finally the raw data normalization is given

---

[10] The measured I_{screen} can be estimated by $I_{screen} = I_{sample} \cdot \delta$, it should be in the order of several nanoamperes, starting from a typical photoelectron current of 5 nA for the HIS He-lamp, a fraction of 25 % for the solid acceptance angle (±43 °) compared to the whole emission hemisphere of the sample, a total grid transmission of $(0.81)^8$ and an amplification factor of the MCP in the order of 10^4.

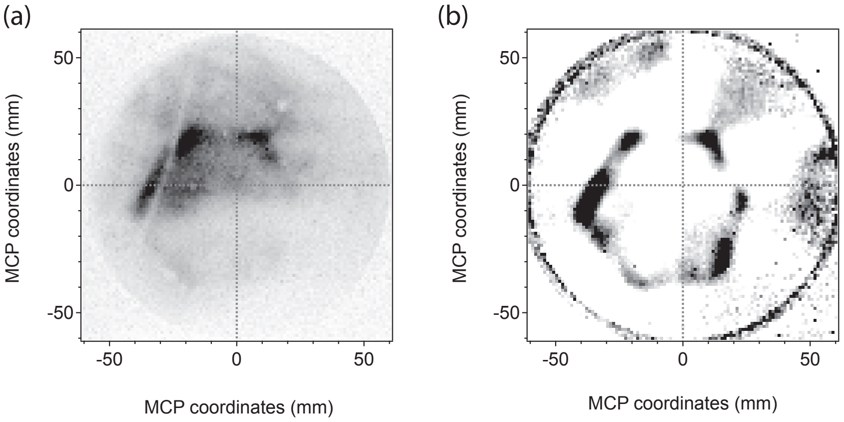

Figure 11: Raw data (a) and (b) Fermi surface maps normalized with Eq. 13 of Cu(332), measured with $h\nu = 40.8\ eV$ at an analyzer pass energy of 27 eV, within 30 s data acquisition time.

by [2,3]:

$$I_{norm}(x,y) = \frac{I_{raw}(x,y) - I_{dark}(x,y)}{I_{sens}(x,y) - I_{dark}(x,y)} \tag{13}$$

The difference between the raw data of a Cu(332) FSM in Fig. 11 (a) and the corresponding normalized data in (b) clearly point out the importance of such a normalization processing. Note that the cross section for the Shockley surface state at $h\nu = 40.8$ eV is relatively small and that the prominent hexagonal feature at E_F is due to the bulk Cu *sp*-band crossing the Fermi level.

4. Angular warping caused by reflection at the ellipsoidal symmetry was analytically calculated in Ref. [34]. Most importantly the distortions in θ can be compensated for by titling the detector by a fixed angle $\alpha_{MCP} = 14.62°$, as shown in Fig. 6. Still a slight strain in the ϕ-mapping [2, 3] has to be corrected for nummerically in the sense of a coordiante transformation from $I_{norm}(x', y')$ to $I_{norm}(x, y)$, as described elsewhere [34].

5. The detection geometry after the second focal point and accordingly after the aperture defines the transformation from position (x, y) on the screen to the emission angle (θ, ϕ):

$$\begin{pmatrix} x \\ y \end{pmatrix} = d_{MCP} \cdot \tan\theta \begin{pmatrix} \cos\phi \\ \sin\phi \end{pmatrix}, \tag{14}$$

whereas $d_{MCP} = 62$ mm is the distance between the MCP and the lower focal point.

6. Finally the photoelectron distribution as function of kinetic energy E_{kin} and the momentum parallel to the surface $(\hbar k_x, \hbar k_y)$ can be obtained by (see Sec. 2.1.1)

$$\begin{pmatrix} k_x \\ k_y \end{pmatrix} = \frac{1}{\hbar}\sqrt{2m_e E_{kin}} \cdot \sin(\theta) \begin{pmatrix} \cos(\phi) \\ \sin(\phi) \end{pmatrix} \quad . \tag{15}$$

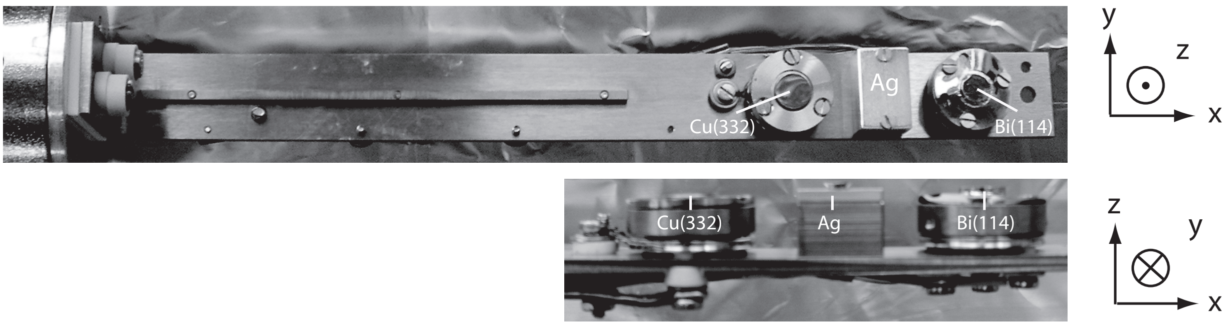

Figure 12: Picture of the latest EDA sample holder: three samples are mounted at the end of the rather simple sample holder made of a copper-beryllium alloy. The copper and bismuth crystals are mounted on top of a "Swiss-Stub" [23] sample holder to meet the requirement of compatibility with the VG ESCALAB 220 [23] at University of Zürich and the COPHEE spectrometer [35] at the Swiss Light Source. Hence the absolute orientation of the different crystal axes of the samples is already known from previous XPD measurements. Furthermore the Cu(332) sample can be resistively heated up to 1100 K. Sample holders and the rectangular silver surface are contacted with each other and floated with respect to the manipulator by means of isolating Al_3O_2 ceramics. U_{sample} of the copper and bismuth crystal can be varied independently from the sample holder potential in order to avoid stray fields. Note that the height of all three sample surfaces has to be exactly the same for ensuring identical imaging conditions. Furthermore all ceramic parts are shielded from the incident light by conductive material, *e.g.* tantalum foil, in order to avoid charging of the insulating parts.

Such an alignment requires a special sample holder, shown in Fig. 12, with the three different samples mounted. It is possible to switch between the samples by just changing the longitudinal sample holder position.

3.4 Energy resolution

Mainly three different terms limit the energy resolution of the present detector configuration, all together adding up to an overall energy resolution of the analyzer ΔE_{EDA} given by:

$$\Delta E_{EDA} \approx \frac{1}{2}\sqrt{\Delta E^2_{spherical} + \Delta E^2_{elliptical} + \Delta E^2_{\Phi}}. \tag{16}$$

The three contributions are sketched in Fig. 13.

- $\Delta E_{spherical}$: The finite spot size of the light source on the sample surface causes an energy broadening, as shown in Fig. 13 (a) and given by

$$E_{min} = \frac{e \cdot U_{G1}}{cos(\alpha)} \approx e \cdot U_{G1}\left(1 - \left(\frac{r}{R_{G1}}\right)^2\right) \tag{17}$$

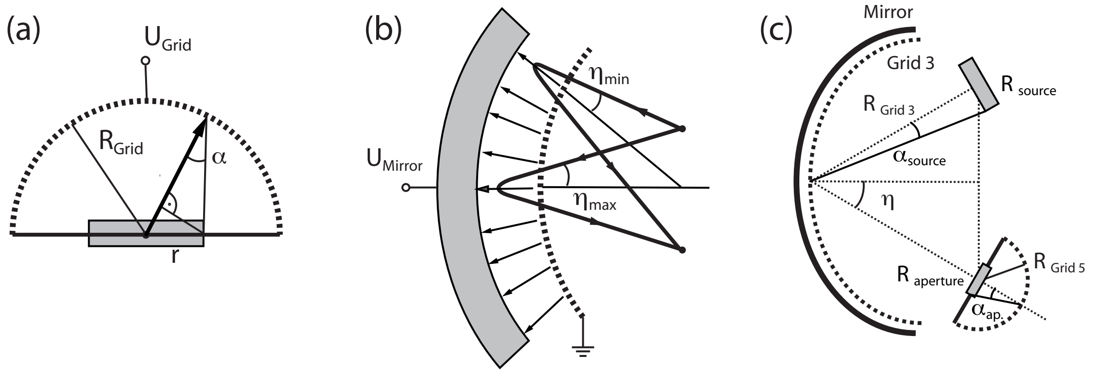

Figure 13: (a) Image broadening due to a finite spot size, leading to an energetic broadening $\Delta E_{spherical}$. (b) Photoelectron trajectories (*black solid lines*) for maximal η_{max} and minimal η_{min} incident and reflection angle, resulting in $\Delta E_{elliptical}$ according to Eq. 19. (c) Schematic illustration of the angular broadening caused by the finite size of the light spot in the upper and of the aperture in the lower focal point of the ellipsoidal mirror.

$$\frac{\Delta E_{spherical}}{E_{pass}} \approx \sqrt{\left(\frac{r_{source}}{R_{Grid1}}\right)^4 + \left(\frac{r_{aperture}}{R_{Grid5}}\right)^4} \tag{18}$$

which amounts to 2 % for a 3.5 mm UV spot and 0.1 % for a 0.1 mm laser spot

- $\Delta E_{elliptical}$: The concentric ellipsoidal mirror and G_3 are equipotential surfaces with electrical field vectors perpendicular to both surfaces, symbolically marked as arrows in Fig. 13 (b). It is obvious that two photoelectrons with different E_{kin} and different incidence angles η_{max} and η_{min}, especially at the center and at the edge of the mirror, can have the same momentum parallel to this field and thus both fulfill the necessary condition

$$e \cdot U_{Mirror} \;=\; cos(\eta)^2 \cdot E_{kin} \tag{19}$$

for being reflected at the low pass mirror M_0, M_1 and M_2. This gives rise to an energy broadening $\Delta E_{elliptical}$ given by

$$\frac{\Delta E_{elliptical}}{E_{pass}} \;=\; \left(\frac{1}{cos(\eta_{max})^2} - \frac{1}{cos(\eta_{min})^2}\right). \tag{20}$$

The calculated relative energy broadening $\Delta E_{elliptical}/E_{pass}$ of the center segment with the corresponding maximal $\eta_{max} = 10.6°$ and minimal incident angle $\eta_{min} = 9.0°$ amounts to 1 %. Without fragmentation of the ellipsoidal mirror and thus η_{max} of 13.5° the relative broadening would increase up to a value of 3.2 %.

- ΔE_{Φ}: Variations in the workfunction Φ for different solid angles on the mirror surface and on the gold grids can be caused by surface inhomogeneities and contaminations, leading to an energy broadening ΔE_{Φ}. Unfortunately not all the parts of the detector are coated with

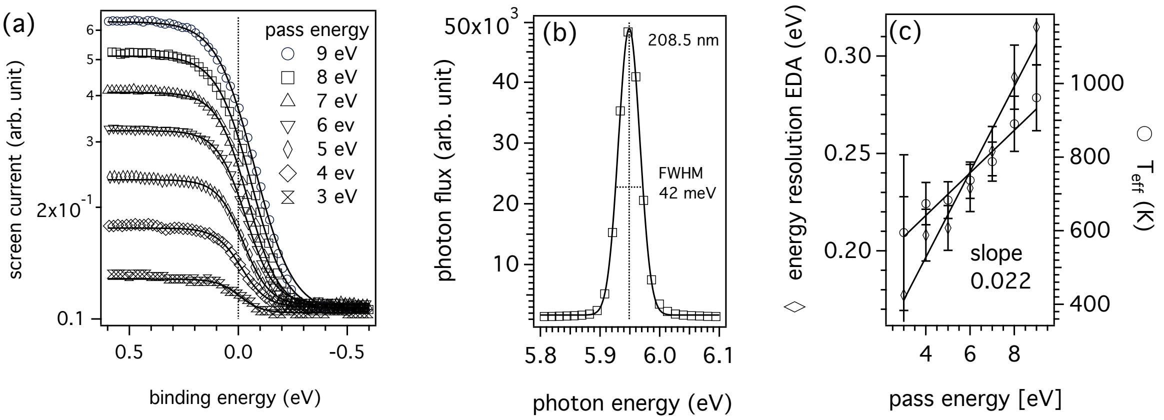

Figure 14: (a) Measured Fermi edges for different pass energies E_{pass} between 3 eV and 9 eV, taken with 6 eV photons with a a spectral distribution of (b). (c) Fitted effective temperature T_{eff} of the Fermi tail and the corresponding extracted detector energy resolution ΔE_{EDA}.

graphite. For example the mirrors M$_0$, M$_1$ and M$_2$ consist of uncoated aluminum which may oxidize. Since the detector was exposed to ambient air pressure for several years it is likely that the energy resolution was degraded significantly after the years. Nevertheless this contribution is hard to quantify but can be estimated from the difference between the calculated first two points and the measured energy broadening of the structures.

In conclusion the energy resolution of the EDA is predominantly limited by the ellipsoidal reflection characteristics. The mainly intrinsic $\Delta E_{elliptical}$ sets a principle lower boundary, leading to a value of 1.1 % for a laser beam waist of 100 μm, corresponding to a calculated overall energy resolution of the detector of about 100 meV at a given pass energy of 9 eV.

3.4.1 Energy resolution as function of pass energy

It turns out from Eq. 18 and 20 that the absolute energy resolution ΔE_{EDA} linearly depends on the chosen pass energy E_{pass}. Fig. 14 (a) presents measured Fermi edges from a polycrystalline Ag surface, taken with $h\nu = 6$ eV for different pass energies E_{pass} between 3 eV and 9 eV respectively. Fitting the Fermi distribution leads to an effective temperature T_{eff} which can be decomposed into a thermal contribution and an experimental broadening ΔE_{exp} according to

$$T_{eff} \;=\; \sqrt{\left(\frac{\Delta E_{exp}}{4k_B}\right)^2 + T^2} \quad . \tag{21}$$

The spectral width $\Delta E_{hv} \approx 42$ meV of the 6 eV laser pulses in Fig. 14 (b) and total detector resolution ΔE_{EDA} add up quadratically to the total experimental resolution ΔE_{exp} as

$$(\Delta E_{exp})^2 \;=\; (\Delta E_{hv})^2 + (\Delta E_{EDA})^2 \quad . \tag{22}$$

Plotting the resulting ΔE_{exp} from the fitted T_{eff} as function of E_{pass} in Fig. 14 (c) leads to a slope of 2.2 % with an offset of 110 meV and hence to an energy resolution of 350 meV according to Fig.

14 for 9 eV pass energy. The deviation from the estimated relative broadening of 1.1% could either be explained by the quantitatively unknown contribution of work function inhomogeneities ΔE_Φ or by the fact that the segmentation of the ellipsoidal mirror into five subparts with 3 distinct mirror voltages U_{M1}, U_{M2} and U_{M3} does not fully improve the resolution.
Lowering the pass energy E_{pass} improves on one hand the absolute experimental energy resolution but compromises the signal-to-noise ratio on the other hand, as can be directly seen from the decreasing photoelectron intensity at E_F in Fig. 14 (a) for decreasing pass energies. Nevertheless, from experience, a constant E_{pass} of 9 eV turned out to be a good trade-off between both competing effects.

3.4.2 The high pass unit

The applied potential U_{G5} sets the upper boundary for the band pass ΔE by [2]

$$eU_{G5} \;=\; E_{pass}\cdot\left(1-\left(\frac{r_A}{R_{G5}}\right)^2\right)-\frac{1}{2}\Delta E\;. \tag{23}$$

The voltages of the neighboring grids U_{G4} and U_{G6} are set to ground in order to provide a field free propagation from the aperture to the high pass unit as well as from the high pass to the MCP, respectively. Angle-integrated photoemission spectra from the Bi(114) surface at $\overline{\Gamma}$ for different band pass widths ΔE by varying U_{G5} are shown in Fig. 15 (a). As expected from Eq. 23 the energy resolution represented by the width of the Fermi edge linearly depends on the band pass, as shown in Fig. 15 (b). The function of the high pass unit can be demonstrated by the rather structure less *bold line* in Fig. 15 (a), measured for U_{G5} set to ground, corresponding to $\Delta E \approx 10$ eV. The first derivative of this spectrum with respect to the binding energy is shown in Fig. 15 (c), revealing the same spectral features as the spectrum taken for a narrow band pass $\Delta E = 0.02$ eV. Comparison of both curves in Fig. 15 (c) hence confirms the benefit arising from the use of a high pass filter.

3.5 Angular resolution

A direct comparison between an angle-integrated (±43°) and an angle-resolved spectrum (±3°) is shown in Fig. 9 (a). The angle-resolved mode is necessary to resolve the Shockley surface state of Cu(332) close to $\bar{\Gamma}$. The angular resolution of the EDA $\Delta\alpha_{EDA}$ is limited by the size of the aperture and the beam waist of the light spot on the sample, as illustrated in Fig. 13 (c). Both contributions sum up quadratically according to

$$\Delta\alpha_{EDA}=\sqrt{\Delta\alpha^2_{source}+\Delta\alpha^2_A} \tag{24}$$

where the individual contributions of the spot size $\Delta\alpha_{source}$ and the aperture $\Delta\alpha_A$ are given by

$$\Delta\alpha_{source}=\arctan\left(\frac{r_{source}}{R_{G3}}\right)\;;\quad \Delta\alpha_A=\arctan\left(\frac{r_A}{R_{G5}}\right) \tag{25}$$

leading to an angular resolution of 1.8° and 2.8° for the 0.1 mm laser spot and for the 3.5 mm wide UV spot of the He-discharge lamp, respectively.

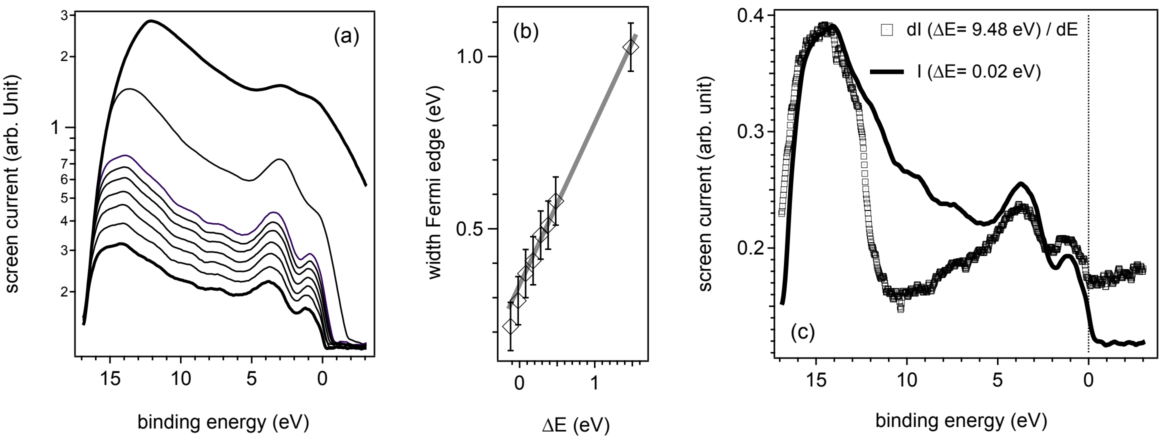

Figure 15: (a) Angle-integrated valence band spectra (I_{screen} versus E_B) of the Bi(114) surface centered at $\overline{\Gamma}$ and $h\nu = 21.21$ eV, for different widths of the band pass ΔE as plotted in (b), set by U_{G5}, and the corresponding extracted energy width of the Fermi edge in (b). (c) Direct comparison between a spectrum $I(0.02\ eV)$ taken for 20 meV band pass width (*solid line*) and the first derivative $dI(\Delta E = 9.48\ \text{eV})/dE$ with respect to the energy of a spectrum taken with a bandpass width of 9.48 eV (*open markers*; high pass voltage set to ground).

3.6 Characterization at low photon energy

3.6.1 Intensity dependent mapping of the Cu(332) surface state

Mutual Coulomb repulsion in densely packed photoelectron clouds propagating in vacuum distort the initial kinetic energy and the momentum of the photoelectrons. These distortions are called space-charge effects [36–38]. Shifts in kinetic energy and the energetic broadening of distinct spectral features caused by space-charge effects will be discussed in detail in Sec. 4.5.3. Constant energy cuts (Fig. 16) and angle-integrated 2PPE spectra from the vicinal Cu(332) surface (Fig. 17 a), reveal strong spectral distortions already for less than 10^3 photoemitted electrons per pulse [11], namely shifts towards higher kinetic energies for the Shockley surface state. By tripling the pulse energy from 3 nJ to 9 nJ at constant pulse width of 105 fs the kinetic energy of the surface state shifts by 100 meV towards higher kinetic energies, as shown in the inset of Fig. 17 (a). Nevertheless the corresponding angular distribution in Fig. 17 (b) remains surprisingly unaffected for a pulse density $< 10^4$ photoelectrons, as can be seen from the width of the surface state crossing through the Fermi level in Fig. 17 (b). For more than 10^4 photoelectrons per pulse the detected line width of the surface state parabola is dramatically broadened, visible in the one-dimensional intensity cut versus detector coordinate for 200 nJ pulse energy. This finding legitimates lateral Coulomb repulsions to be neglected for densities of about 10^3 photoelectrons per laser pulse in the space-charge model of Sec. 4.5.3.

---

[11] The number of 10^3 photoelectrons per pulse has been deduced from the measured sample current for a pulse energy of 100 nJ in Fig. 16 and Fig. 17 (a).

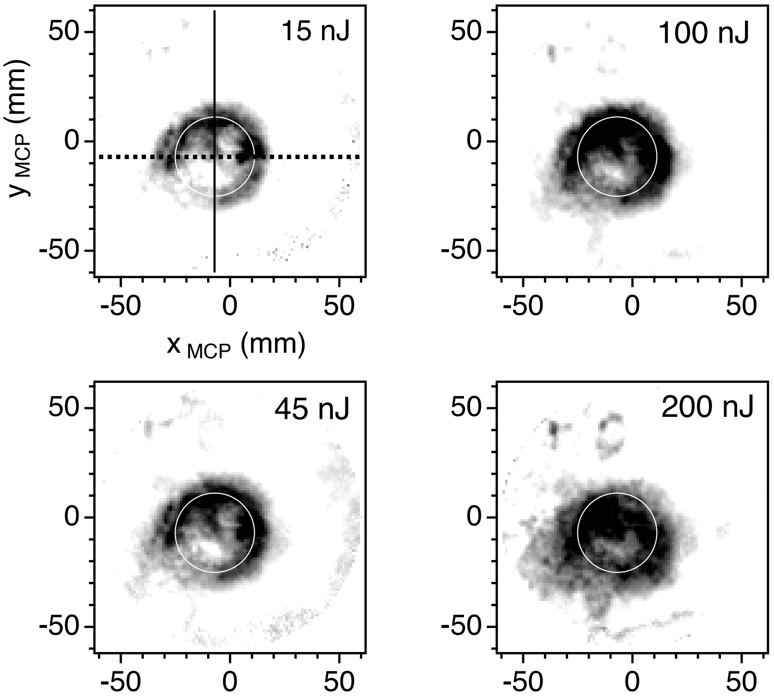

Figure 16: Fermi surface maps revealing the Shockley surface state of Cu(332), taken for different light intensity between an energy of 15 nJ and 200 nJ per pulse by means of direct 2PPE.

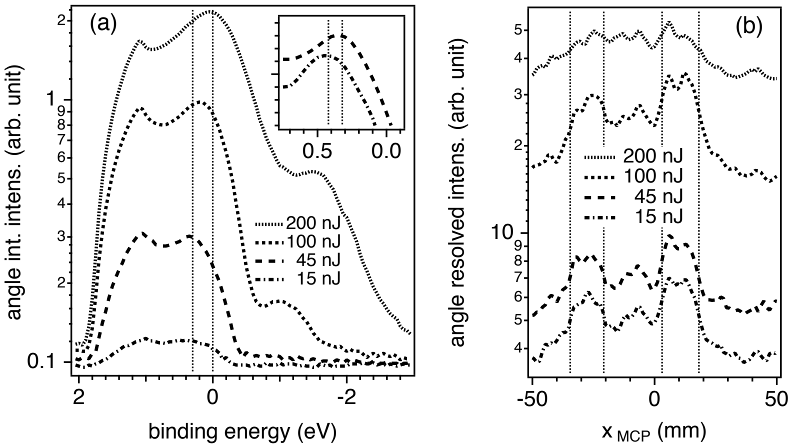

Figure 17: (a) Angle-integrated spectra: I_{screen} versus binding energy. *Vertical lines* denote the Fermi level and the band bottom of the Shockley surface state close to $\bar{\Gamma}$. *Inset* zooms into the surface state for a light fluence below and above the space-charge limit, respectively. (b) Constant energy cuts along the horizontal *dashed line* in Fig. 16 for different laser pulse intensities between 15 nJ and 200 nJ. *Vertical lines* serve as guide to the eye for the space-charge induced lateral broadening of the angular distribution of the surface state electrons.

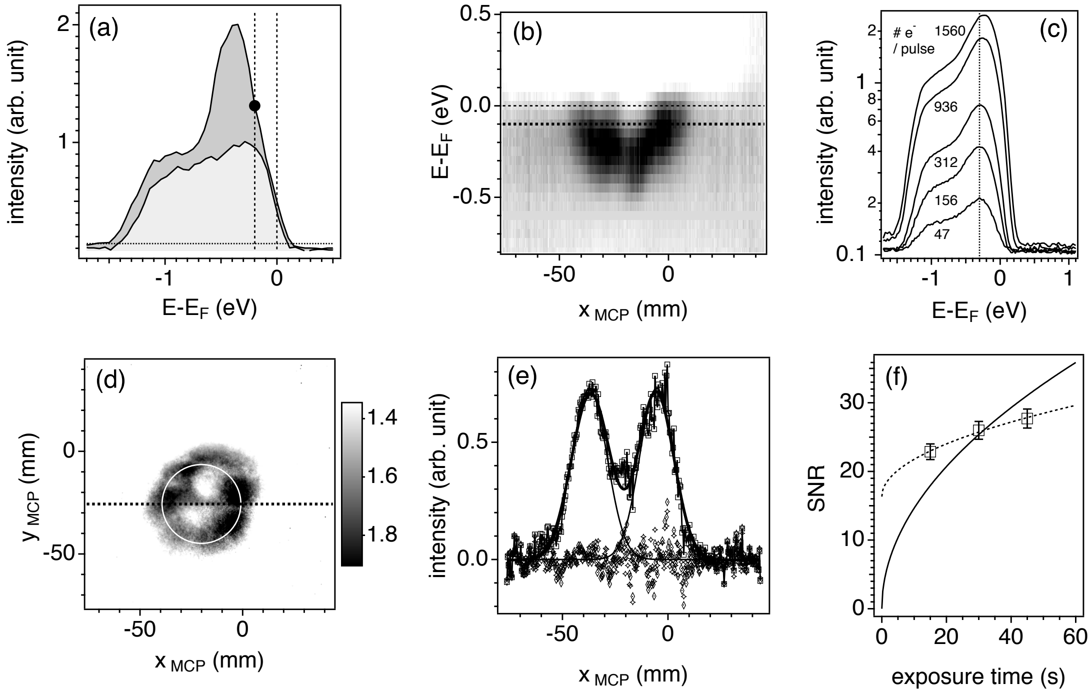

Figure 18: (a) Angle-resolved 1PPE spectra with 6 eV laser pulses, taken at (k_x, k_y) = (0.2, 0) Å^{-1} (*dark grey area*) and at (k_x, k_y) = (0.6, 0) Å^{-1} (*light grey area*) with a data acquisition time of 15 s. (b) Energy versus momentum along $\overline{\Gamma}$-$\overline{M}$. (c) Angle-integrated 1PPE spectra for different 6 eV laser pulse intensity. Note that a number of 300 electrons per pulse is at the space-charge limit. (d) Constant energy contour of the Shockley surface state of Cu(332) at -100 meV binding energy. (e) Fermi level cut (*empty quadratic markers*) along k_x and corresponding double Gaussian fit (*solid line*), leading to a statistical deviation (*empty diamonds*) between fitted and measured values. (f) Signal-to-noise ratio (SNR) for 15 s, 30 s and 45 s data acquisition time, plotted together with the theoretical $\sqrt{n}$ dependence from Eq. 27 without (*solid line*) and with offset (*dashed line*).

3.6.2 Signal-to-noise ratio

One way to characterize the EDA data quality as function of data acquisition time is by evaluation the so called signal-to-noise ratio (SNR) which can be defined as [39]

$$SNR := \frac{\mu}{\sigma} \propto \sqrt{n}\ ; \quad \mu = \sum_{i=1}^{n} \frac{x_i}{n}\ ; \quad \sigma = \sqrt{\sum_{i=1}^{n} \frac{(x_i-\mu)^2}{n}}. \tag{26}$$

Usually the SNR quantifies the ratio of mean value μ_{sig} of the signal to the standard deviation of the background σ_{back}, or between μ_{sig} and the standard deviation of the signal σ_{sig}. The $\sqrt{n}$-dependency of the SNR directly follows from the definition of σ and μ in Eq. 27 and the central limit theorem [12].

Regarding TR-ARPES experiments as possible application for the EDA detector the imaging quality at low pass energies[13] for pulsed low-energy photon sources, such as the fourth-harmonic 6 eV probe pulses, is decisive.

Again the parabolically dispersing Cu(332) surface state, with its binding energy maximum at 300 meV and an almost circular Fermi surface crossing with radius 0.2 Å^{-1} [40] has been mapped with 6 eV pulses. The light fluence was kept slightly below the space charge limit of 300 electrons per pulse, corresponding to the *black curve* in (c), providing the maximal distortion free yield and thus the maximal statistics.

The measured dispersion along $\overline{\Gamma}$-$\overline{M}$ in Fig. 18 (b) as well as the constant energy contours at a binding energy of 100 meV in (d) are consistent with the experimental description of Baumberger *et. al* [40].

The cut $I(k)$ at constant energy E_F along $\overline{\Gamma}$-$\overline{M}$ (Fig. 18 e) reveals the two Fermi level crossings at 0.05 Å^{-1} and 0.45 Å^{-1} from the surface state band. In this context the SNR can be defined as the ratio of the fitted peak intensity I_{max} to the standard deviation of the measured values from the fitted double-Gaussian as function of k

$$SNR \ = \ I_{max} \ / \ \sqrt{\sum_k (I_k - I_{gauss})^2 \ / \ k} \quad , \tag{27}$$

as shown in Fig. 18 (e). This value should then provide an estimate on the sensitivity of the k-resolved photoelectron mapping. TR-ARPES measurements target small transient changes in the occupied band structure $I(E, k, t)$ and hence require a dynamical range of several orders of magnitude. The SNR in k-direction sets an upper limit for the accessible dynamical range of the EDA, by using 6 eV photons.

The rather low SNR values of 23, 26 and 28 for data acquistion times of 15 s, 30 s and 45 s in Fig. 18 (f) show a significant deviation from the $\sqrt{n}$-dependence.

In conclusion, an average SNR of 20 sets a lower boundary for detectable transient band structure changes in TR-ARPES measurements using the EDA in the angle resolved mode. Meaning that laser pulse induced transient changes of the occupied and unoccupied band structure have to amount more than 5 % of the strongest occupied band structure features around E_F in order to be distinguished from background fluctuations.

---

[12] The central limit theorem states that the mean of a sufficiently large number of independent random variables tends to be normally distributed [39]. In other words: $\lim_{n\to\infty} P(Z_n \leqslant z) = \Phi(z)$, whereas $\Phi(z)$ is the normal distribution and $Z_n = \left(\sum_{i=1}^{n} X_i - \mu \right) / \sigma$ is the standard score.

[13] The SNR studies have been performed for a pass energy of 9 eV since the best compromise between energy resolution and photoelectron yield has been achieved for this value, as discussed in Sec. 3.4.1. Furthermore MCP voltages were set to 0.2 kV and 1.2 kV respectively, subsequently followed by a 3.6 kV phosphor screen voltage.

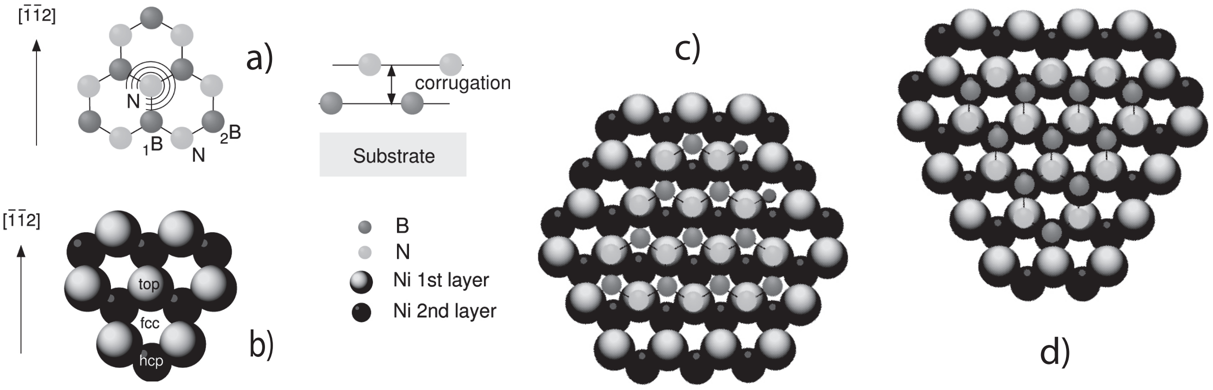

Figure 19: (a) Hexagonal boron nitride. The first and second boron neighbors of the center N atom are indicated. The hexagonal honeycomb sheet structure is visible. (b) The first and the second layer of Ni(111). The three different bonding positions fcc, *hcp* and *top* are labeled. *c*) (N,B) = (top, fcc): The nitrogen atoms sit on top of the atoms of the outermost Ni surface layer, the boron atoms on the fcc-hollow sites. *d*) (N,B) = (top, hcp): nitrogen atoms on top of the outermost Ni atoms, boron atoms on the *hcp* site. From Ref. [41].

4 Hexagonal boron nitride on Ni(111)

4.1 Structure

Hexagonal boron nitride (h-BN) is a wide band gap material that has a simple crystal structure and electronic configuration. Yet, in spite of numerous studies over several decades, there is still considerable controversy about details of its electronic structure and in particular its optical properties. The system used throughout this chapter consists of a monolayer of hexagonal boron nitride (h-BN) deposited on Ni(111).

4.1.1 Geometric structure of h-BN/Ni(111)

X-ray photoelectron diffraction (XPD) was used together with scanning tunneling microscopy (STM) to examine the structure, and photoelectron spectroscopy (XPS) to determine the chemical composition of the h-BN monolayers [41, 42]. After charge transfer, a boron and nitrogen atom pair is isoelectronic to a pair of carbon atoms. Boron nitride forms on Ni(111) a graphene-like honeycomb sheet (Fig. 19). The small lattice misfit between Ni(111) (2.49 Å) and h-BN (2.50 Å) of -0.4% allows for epitaxial growth, where the layer is slightly corrugated perpendicular to the Ni(111) surface (Fig. 19). Density functional theory (DFT) calculations [43] yield two possible structural configurations with the nitrogen atom on top of the outermost Ni atoms and the boron atom either on the fcc- or on the hcp-hollow site (Fig. 19 (c) and (d)). According to the XPD and STM results of Auwärter [42] the structure with the boron atoms sitting on the fcc-hollow sites is energetically more favorable. However, the small energy difference between the two configurations compared to $k_B T$ at monolayer growth temperatures (1050 K) may also lead to *hcp* domains.

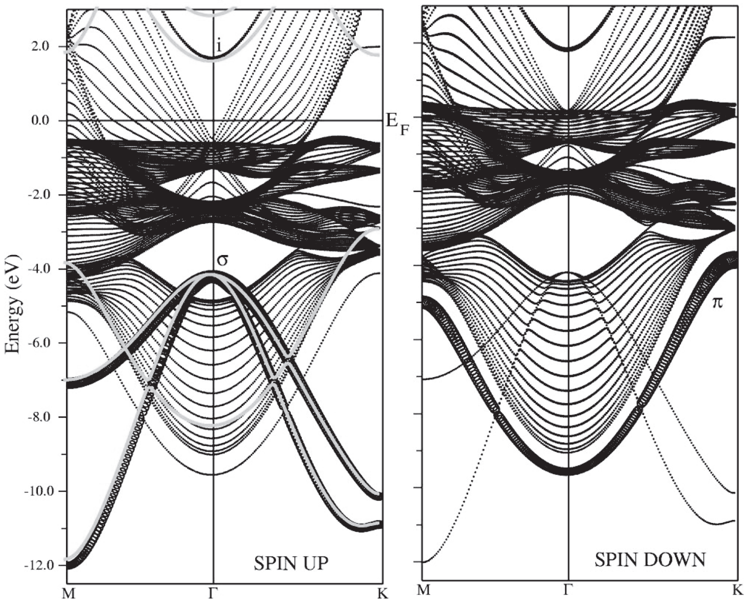

Figure 20: Band structure of h-BN/Ni(111) along $\bar{M}$-$\bar{\Gamma}$-$\bar{K}$ within DFT by Grad *et al.* [43]. The spin up and spin down subbands are plotted seperately. The thick *grey lines* indicate the bands of a freestanding h-BN monolayer. Graph from Ref. [43].

XPD was also used to determine the existence of *hcp* domains [41].

4.1.2 Electronic structure of *h*-BN/Ni(111)

h-BN/Ni(111) provides at least three additional electronic energy bands σ_1, σ_2 and π below E_F compared to bare Ni(111), seen as BN related peaks in the DFT calculations by Grad *et al.* [43] (Fig. 20) and in the He Iα normal emission spectrum (Fig. 21 (a), π_1 and π_2 are degenerated at $\bar{\Gamma}$). The binding energies are listed in Table 2 (values from Auwärter [41], in agreement with the ones of Nagashima [44]). The σ and π band are well separated from the Ni $3d$-bands and far from the Fermi level. Thus they do not contribute directly to the conductivity of the system. In this sense the h-BN monolayer is an insulator. Density functional theory (DFT) predicts the first h-BN related conduction band at a negative binding energy of 1.6 eV above E_F. This state is termed an interface-state band (labeled with i in Fig. 20). No significant changes upon h-BN formation

	$\pi(\bar{\Gamma})$	$\sigma_{1,2}(\bar{\Gamma})$	$i(\bar{\Gamma})$
Experiment: E_B [eV]	10.0	5.3	-
Theory ↑: E_B [eV]	9.60	4.25	-1.63
Theory ↓: E_B [eV]	9.61	4.23	-1.75

Table 2: Binding energies of the π, σ_1, σ_2 bands and the interface-state band i at the center of the Brillouin zone. Experimental data from ARPES as well as theoretical obtained from DFT [43].

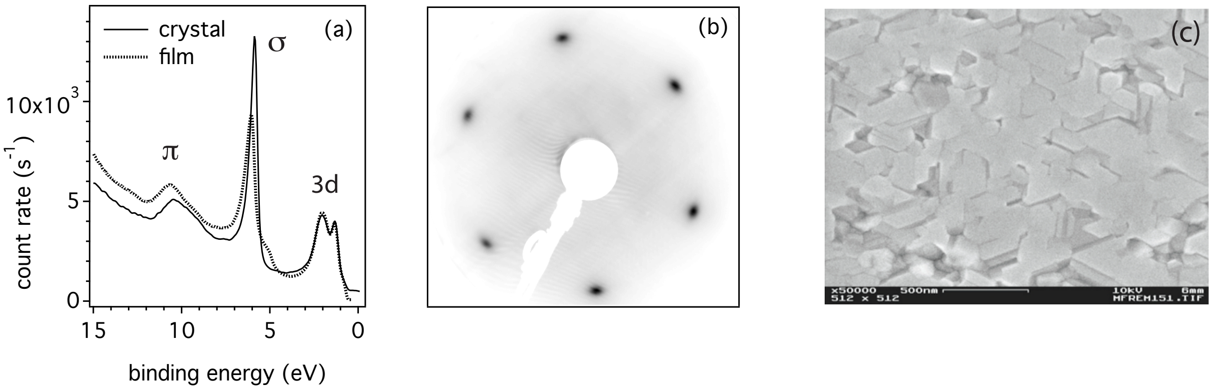

Figure 21: (a) UP spectra of h-BN on the Ni(111) single crystal (*solid line*) and on the 80 nm thick Ni film (*dotted line*), both revealing the Ni d-bands as well as the occupied π- and σ-band of the BN monolayer. (b) LEED pattern and (c) SEM image of the 80 nm thick Ni film (2.2 μm × 1.7 μm).

are found for the dispersion, the exchange splitting (Table 3) and the energy position of the sp- and $3d$-bands of Ni. The unoccupied interface state i and the h-BN π-band are exchange split by an amount of $\Delta E_{ex}(i) \approx 120$ meV at $\bar{\Gamma}$ [45] and $\Delta E_{ex}(\pi) \approx 260$ meV (at $\bar{K}$), respectively [41].

	sp-band: Δ_{ex} [meV]	3d-band: Δ_{ex} [meV]
Ni(111)	250 ± 20	290 ± 25
h-BN/Ni(111)	250 ± 20	296 ± 30

Table 3: Experimentally observed exchange splitting for bare Ni as well as for a hexagonal boron nitride monolayer coverage (from Ref. [41]).

The UPS normal emission spectrum also indicates a decrease of the work function from 5.35 eV on bare Ni(111) to 3.55 eV on h-BN/Ni(111) [41] (3.6 eV in Ref. [46]). The h-BN layer is polarized by the Ni substrate such that dipoles at the surface form lowering the workfunction according to Ref. [47]. Charge transfer in the order of 0.06 electrons per unit cell from BN to the unoccupied minority d-bands of Ni occurs [43]. The spin polarization drops and the magnetic moment is reduced in the top Ni layers by 0.08 μ_B shown by calculated layer-resolved magnetic moments [43].

4.1.3 h-BN film preparation on Ni(111) and experimental characterization

The h-BN monolayers on a Ni(111) single crystal as well as on a 80 nm thick nickel film and the corrugated h-BN layer on a Rh(111) film were grown under ultrahigh vacuum conditions (base pressure of 10^{-10} mbar) by chemical vapor exposure to ∼100 L (1 Langmuir = 10^{-6} torr sec) of borazine at a surface temperature of 1070 K [44, 48]. The quality of the h-BN monolayer was

verified by UPS (Fig. 21 a), XPS and LEED (Fig. 21 b) [42]. Moreover, the work function of the sample was constantly monitored during the laser measurements by recording 2PPE spectra over the full energy range. During all experiments no changes of the work function were observed, thus no optically induced desorption of the hexagonal boron nitride monolayer occured under the intense pump pulse radiation. The h-BN monolayers remained stable over several days at room temperature and even at temperatures up to 900 K and thereby permitted long measurement periods under reproducible conditions [49]. The sample temperature was controlled by means of a PID-controller and measured by means of a Raytek pyrometer and a thermocouple. Unless otherwise stated all time-resolved measurements were taken at room temperature.
The epitaxial 80 nm thick nickel film has been grown on an $Al_2O_3(0001)$ substrate by M. Schreck and S. Gsell (in Augsburg). In order to improve the surface quality for the subsequent heteroepitaxial metal growth, $Al_2O_3(0001)$ crystals with dimensions of 10 x 10 x 0.5 mm^3 were subject to a high temperature annealing step at 1473°C for 16 h in air. Afterwards, the Ni films were deposited by electron-beam evaporation with a typical thickness of 80 nm at a substrate temperature of 350°C in high vacuum (10^{-6} mbar) [50]. X-ray diffraction measurements show a two-times three-fold symmetry related to two domains of (111) oriented surfaces, one rotated by 60° with respect to the other. The low mosaicity of the film can be characterized with scanning electron microscopy (SEM) by a tilt of 0.37°, a twist of 2.8° and a domain size of 200 – 300 nm of the individual crystallites (Fig. 21 c). The film thickness was characterized by Rutherford backscattering.

4.1.4 Image potential states on *h*-BN/Ni(111)

An electron in front of a metallic surface at a distance z induces a positive charge density in the metal surface. Since the electrical field parallel to the metallic surface must vanish, the electrical field on the vacuum side is the same as the one produced by the electron plus an opposite charge (image charge) placed at a distance $2z$ away from the electron (Fig. 22 a). The attractive image force between the electron and its image charge is given by a Coulomb-like image potential approaching the vacuum energy E_{vac} for large distances [51].

$$V(z) = E_{vac} - \frac{e^2}{4\pi\epsilon_0}\frac{1}{4z} \tag{28}$$

On the other side bulk band gaps may forbid the penetration of the electron into the metal. An example is the large bulk band gap along $\overline{\Gamma}$-$\overline{L}$ from the Fermi level up to roughly 6 eV above the Fermi level in the case of Ni (Fig. 20). Thus the electron waves get trapped by being reflected back and forth between the crystal barrier (band gap) and the image potential. This one-dimensional potential well leads to an infinite series of Rydberg-type bound states, localized perpendicular to the surface, with energies:

$$E(n) = E_{vac} - \frac{E_1}{(n+a)^2}, \quad n = 0,1,2,.. \quad E_1 = \frac{R_H}{16} = \frac{13.605\ eV}{16} = 850\ meV \tag{29}$$

The factor 1/4 in the potential (Eq. 28) leads to a reduction in the binding energies by a factor of 1/16 as compared to the hydrogen atom. Taking into account that the phase of the electron

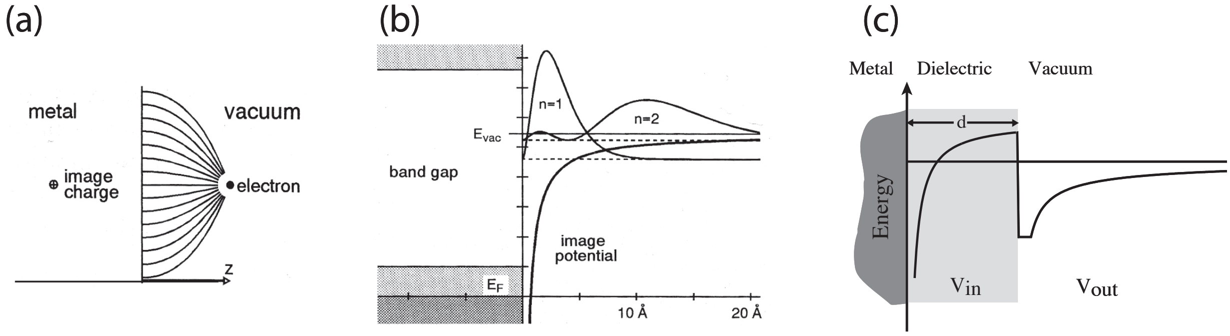

Figure 22: (a) The electric field produced by an electron in front of a metal surface can be described by the concept of an image charge. (b) The attractive image potential as function of the distance from the metal surface leads to a series of bound states if the electron cannot penetrate into the metal due to a band gap. For the lowest two states the square of the wave function is shown. (c) The presence of a dielectric layer on top of a metal surface screens the electric field of the image charge leading to a flattened potential outside the metal-dielectric interface. ((a) and (b) are from Ref. [56] and (c) from Ref. [55])

wavefunction can change upon reflection at the crystal (by the amount of ϕ_C) and at the image potential (ϕ_B), an empirical correction parameter a has to be introduced. This so called "quantum defect" was found to be 0.14 in the case of Ni(111)[14]. Echenique and Pendry [52] derived Eq. 29 (also done in Refs. [53, 54]) with an analytical model, using the phase accumulation condition $\phi_B + \phi_C = 2\pi n$ for bound states (where n is an integer).

Furthermore the presence of a dielectric capping layer on top of a metal surface modifies the image potential in Eq. 28 by a factor of $1/\epsilon$ within the dielectric layer and by (ϵ-1)/(ϵ+1) outside of the dielectric layer, respectively, due to dielectric screening of the electrical image field [55]. Hence the resulting flatter potential on the vacuum side of the metal-dielectric interface leads to lower binding energies, reduced by a factor of (ϵ-1)/(ϵ+1). Assuming a dielectric constant of $\epsilon_\perp = 5$ for the hexagonal boron nitride layer perpendicular to the Ni(111) surface reduces the binding energy of the $n = 1$ image potential state (IPS) from 0.85 eV in the case of bare Ni to 0.6 eV in the case of h-BN/Ni(111), in good agreement with the results of two-photon photoemission (2PPE) experiments [46].

---

[14] The calculated value a bases on the experimentally deduced binding energy of the $n = 1$ Rydberg state on Ni(111) [46]

4.2 Interface states in single layer *h*-BN on metal surfaces

The unoccupied band structure of *h*-BN/Ni(111) has previously been explored in this group with femtosecond TR-2PPE spectroscopy in a two-color setup by Muntwiler *et al.* [46]. Two distinct, dispersive intermediate states have been observed at the origin of the surface Brillouin zone: a BN-related interface state at 1.51 eV above the Fermi level, which forms the conduction band, and an image potential state (IPS) at 0.65 eV below the vacuum level. The lifetimes of the two unoccupied states are measured to be 260 fs for the image potential state and 110 fs for the interface state. The remarkably high values can be explained by the very small overlap of the corresponding wave functions with the nickel bulk states [46].

This chapter further focus on the interface state which can be discussed within two theoretical frameworks.

On one hand DFT calculations by Grad *et al.* [43] predict such a BN-related interface state for the *h*-BN/Ni(111) surface, in analogy to the interlayer states in bulk BN. The DFT calculations include the atomic structure of the BN monolayer but neglect the attractive image potential experienced by an electron within or outside of the *h*-BN/Ni(111) interface.

On the other hand calculations within the dielectric continuum model (DCM) predict beside the image potential states an additional state with higher binding energy. DCM includes the screening of the image potential by the dielectric layer but neglects the atomic structure of the dielectric layer, respectively. Insulating thin adsorbate layers on metal surfaces have widely been studied by means of TR-2PPE [55, 57, 58]. For example the energetics and lifetimes of unoccupied image potential states at adsorbate-covered surfaces, like *e.g.* physisorbed Xe and N_2 overlayers on Cu(111) [57], have been investigated. Calculations in the framework of DCM [57] complete the quantitative understanding of these states, revealing the fact that they are for low coverages spatially located at the adsorbate-vacuum interface. This fact termed these states so called interface states.

However, in the case of the BN-related interface state it is a priori not clear whether the experimentally observed state by means of TR-2PPE corresponds to the state predicted by DFT or DCM.

4.2.1 Spectral identification of the interface state

The monochromatic spectra in Fig. 23 (a) for different *p*-polarized photon energies between $h\nu = 2.70$ eV (460 nm) and 2.38 eV (530 nm) reveal two distinct peaks. The first peak between 3.85 eV and 4.15 eV above the Fermi energy E_F belongs to an indirect 2PPE process via an *h*-BN related unoccupied intermediate state. The second peak between 4.5 eV and 5.1 eV is due to a direct 2PPE transition initially excited from the occupied Ni *d*-bands (Λ_3), most likely via a virtual intermediate state into the vacuum.

The origin of a spectral feature from either occupied or unoccupied states in the 2PPE spectra can be obtained by varying the photon energy of the laser pulses [59]. Changing the photon energy by the amount of ($\Delta h\nu$) should affect the kinetic energy of the photoelectrons by either

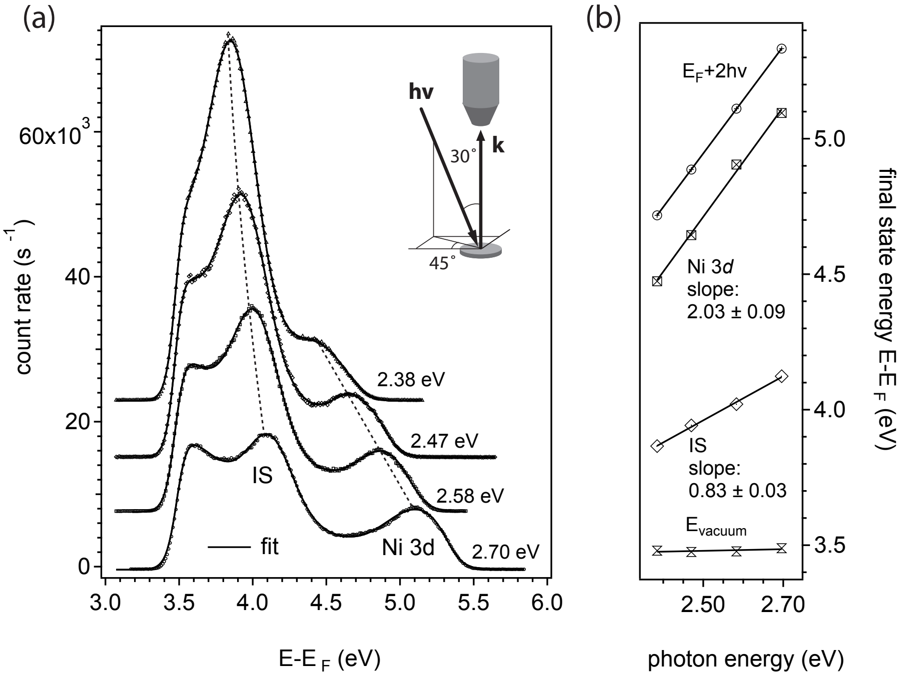

Figure 23: (a) Monochromatic 2PPE spectra for different photon energies between 2.70 eV and 2.38 eV. The positions of the two peaks are denoted by *dashed lines*. The spectra have been normalized by the direct 2PPE yield of the bulk *3d*-bands of nickel. The *inset* schematically shows the present detection geometry. (b) Measured final state energy positions of the secondary cut off (open triangles), the interface state (IS, open diamonds), the direct 2PPE transition from the Ni *3d*-band (open squares) and the Fermi level probed by two times $h\nu$ (open circles) as function of photon energy $h\nu$. Slopes of 1 or 2 in the linear fits (straight lines) indicate unoccupied or occupied states, respectively.

$\Delta E_{kin} = 2(\Delta h\nu)$ for a direct 2PPE transition from an occupied state or by $\Delta E_{kin} = 1(\Delta h\nu)$ from indirect 2PPE via an unoccupied intermediate state above the Fermi level E_F. Note that for strongly dispersing bands the dispersion perpendicular to the surface along $k_\perp$ has to be taken into account.

Nevertheless the second peak quite precisely shifts with $2(\Delta h\nu)$ (slope of 2.03 ± 0.09 in Fig. 23 b) and thus corresponds to a direct 2PPE excitation from the occupied Λ_3 initial state within the d-bulk bands of nickel, at 0.29 eV binding energy.

The measured kinetic energy of the first peak shifts with a slope of $(0.83 \pm 0.03) \cdot (\Delta h\nu)$, which is close to $1(\Delta h\nu)$, it belongs to an indirect 2PPE excitation via the interface state whose binding energy is found to be 1.5 eV above E_F. This interface state has been theoretically predicted by DFT [43, 60–62] and experimentally found by Muntwiler *et al.* [46]. According to the DFT calculations, this state is spatially located *between* the topmost Ni layer and the boron nitride layer. Pumping the interface state with photon energies between 2.38 eV and 2.7 eV creates a photohole in the occupied spectral region between 0.88 eV and 1.2 eV below E_F. The binding

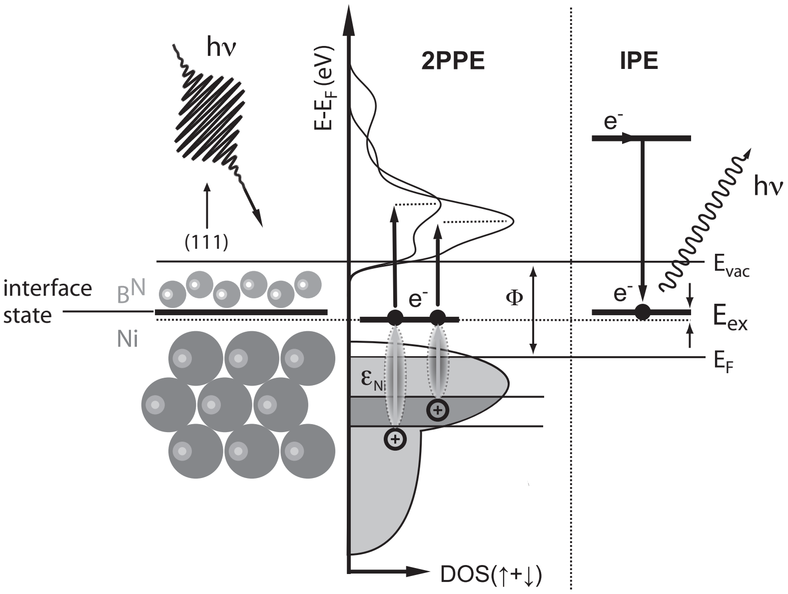

Figure 24: *Left-hand-side*: Comparison of 2PPE and inverse photoemission processes: the interface state (*bold line*) is located between the Ni(111) surface and the boron nitride monolayer. *Center*: Schematic 2PPE excitation from the occupied nickel d-bands via the interface state into the vacuum. The shaded ellipses around the transitions denote the mutual Coulomb attraction between the electron in the interface state and the corresponding photohole in the d-bands, defining the exciton binding energy E_{ex}. *Right-hand-side*: Population of the interface state from a high-energy time reversed LEED state in a inverse photoemission process under emission of a photon.

energy of the h-BN σ-band is 5.3 eV at $\bar{\Gamma}$ [43] and therefore exciton excitation within the insulating boron nitride layer can be excluded. The initial states for the excitation into the interface state rather lie in the bulk d-bands of nickel. This is corroborated by the decreasing intensity of the interface state transition for increasing photon energies which agrees to the decreasing density of states (DOS) in nickel from $E_{binding} = 0.88$ eV to 1.2 eV below E_F. The situation is schematically illustrated in Fig. 24.

4.2.2 The dielectric continuum model (DCM)

In a dielectric continuum model [57], adsorbate layers are modelled by a dielectric slab in front of a metal surface. The dielectric screening ϵ of the adsorbate layer modifies the image potential of the metallic substrate. An outward shift of the IPS wave functions and thus a reduced overlap with the metallic substrate bands leads to lifetimes by one order of magnitude larger as compared to bare metal surfaces [55].

In the case of a h-BN monolayer an Ni(111) the image potential modified by the dielectric continuum (Fig. 25 a) according to Ref. [57] with ϵ set to 5, an over layer thickness of 2.5 Å and an

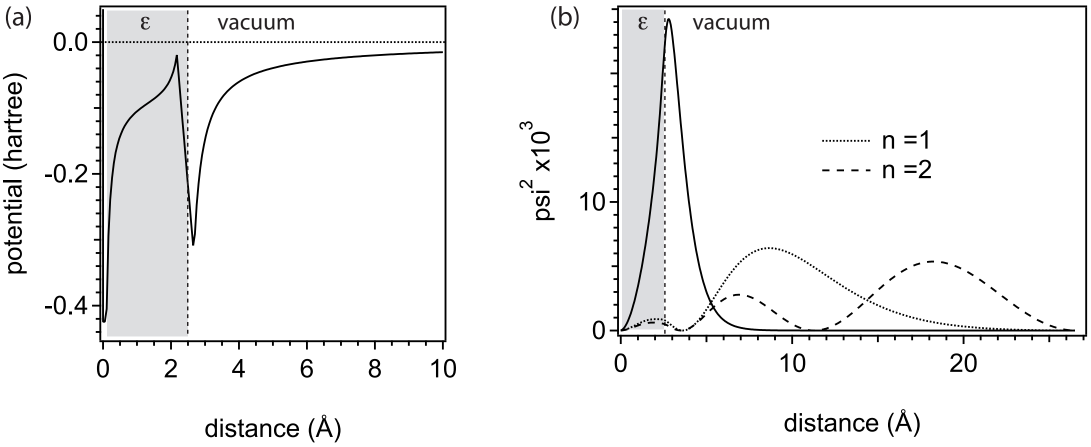

Figure 25: (a) Model image potential, modified by a dielectric slab of 2.5 Å thickness (*grey area*) in front of a metal surface as function of distance from the surface, linearly interpolated at the vacuum-dielectric interface. (b) Wave function squares of the $n = 1$ and $n = 2$ IPS (*dotted lines*) as well as of an additional state (*solid line*) with higher binding energy and spatially located at the BN-Ni interface. Figures with courtesy of M. Muntwiler.

electron affinity of 2 eV (relative to the vacuum level) leads to an additional solution (*solid line* in Fig. 25 b) of the Schrödinger equation, spatially located at the vacuum-dielectric interface, at a binding energy of 1.15 eV above E_F. Since the adsorbed boron nitride monolayer is treated as three-dimensional homogenous dielectric slab in the DCM model the reliability of the obtained energy eigenvalues is limited. However, this calculation by Muntwiler indicates the existence of an additional state at the h-BN/Ni(111) interface similar to the image potential states. The measured feature in the 2PPE spectra could be identified with this state but it is a priori not clear whether the measured state corresponds to the one predicted by DFT or to the one predicted by the dielectric continuum model.

4.2.3 Energy dispersion of the interface state

The dispersion of the h-BN-derived interface band has been measured by first pumping an electron from the $3d$-bands resonantly into the interface state and subsequently into the vacuum by means of two photons from the same pulse with a photon energy $h\nu = 2.70$ eV. Measurements taken at different polar angles θ_m along $\bar{\Gamma}$-$\bar{K}$ are shown in Fig. 26 (a). The measured polar angle θ_m deviates from the real emission angle θ_e due to the applied bias voltage and can subsequently be corrected for by applying Eq. 10. The measured distributions are mapped to E versus $k_{||}$ according to $\hbar k_{||} = \sqrt{2m_e E_{kin}} \sin\theta_e$. Gaussian profile fits from the raw spectral data lead to the energy positions $E_{int}(k_{||})$ of the interface state from which the effective mass m^* is obtained by fitting the parabola $E_{int}(k_{||}) = E_0 + (\hbar k_{||})^2/2m^*$, shown in Fig. 26 (b). An effective mass for the interface state of $1.08 \pm 0.12\ m_e$ was obtained which is slightly higher than the value $1.05 \pm 0.15\ m_e$ from IPE. DFT calculations by Grad *et al.* predicted an interface state band centered at $\bar{\Gamma}$ with

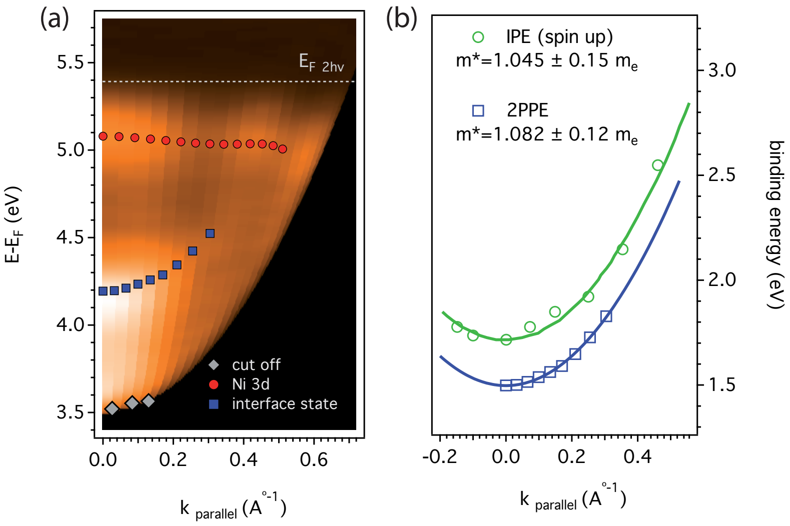

Figure 26: (a) Dispersion along the $\bar{\Gamma}$-$\bar{K}$ direction of the occupied Ni 3d-band (circles) and the unoccupied h-BN related interface state (squares). (b) Fitted energy position of the interface state obtained from IPE (open circles) and monochromatic 2PPE (open squares) versus parallel momentum $k_{||}$.

a positive effective mass of 0.73 m_e (see Table 4).

4.3 Comparison to inverse photoemission data: Excitonic effect?

A direct comparison of 2PPE and IPE measurements at the interface state band bottom at $\bar{\Gamma}$ reveals a difference in binding energy of 190 meV (Fig. 26 b). In inverse photoemission the interface state is populated by an extra electron from a time-reversed LEED state above the vacuum level (electron addition spectrum). In contradiction to that, the transient population of the interface state by means of 2PPE is equivalent to an electron-hole pair at the interface between the nickel surface and the boron nitride monolayer. Mutual Coulomb attraction between the electron in the

method	$E - E_F$ at Γ (eV)	m^*/m_e
DFT	1.75 ↓; 1.63 ↑	0.76
IPE	1.83 ↓; 1.7 ↑	1.05
2PPE (1.55 eV + 3.1 eV)	1.51	0.43
2PPE (2 $*$ 2.7 eV)	1.50	1.08

Table 4: Summary of the calculated and measured effective masses and energy positions at $\bar{\Gamma}$ of the interface state in h-BN/Ni(111) by means of spin resolved DFT [43], spin resolved IPE [45], bichromatic 2PPE [46] and monochromatic 2PPE in the present work. Note the binding energy difference of 200 meV between IPE and 2PPE, respectively.

interface state and the photohole in the nickel d-band may lead to a higher binding energy and, thereby, account for the difference of 190 meV between 2PPE data and IPE results.

This comparison and the according interpretation is not a priori devious since discrepancies of up to 0.5 eV have been reported between optical excitation energies and the corresponding energy difference as obtained from direct and inverse photoemission. For example, direct-photoemission [63] and IPE [64] investigations on the Si(111) (2×1) surface reconstruction show a surface-state band gap at $\bar{J}$ of 0.75 eV, which is 0.3 eV higher than the optical transition energy [65]. Such a large exciton binding energy can be explained by the surface localization of these states: *ab initio* calculations [66] confirmed the optical spectrum including the electron-hole interaction. This 'surface exciton' formed from the antibonding π-bonded surface states D_{down} reveals a binding energy which is more than one order of magnitude larger than in bulk Si (0.015 eV). Spatial confinement of both the electron and the hole at the surface leads to a large overlap between the single-particle wave functions and thus to an increased binding energy in the case of a 'surface exciton' [66]. Time-resolved 2PPE measurements [67] resolved on a similar Si(100) (4×2) reconstruction a surface exciton band 0.14 eV below the upper edge of the band gap. In another example an analogous discrepancy at the $\bar{X}$ point on GaP(110) [68, 69] has even found to be in the order of 0.5 eV.

In the simplest representation, the Coulomb potential of a photohole experienced by the electron within a dielectric layer is given by [70]

$$V_{e-h} = -\frac{e^2}{4\pi\epsilon_0}\frac{1}{\epsilon(k_\perp)r} \tag{30}$$

corresponding to a hydrogen problem with a dielectric constant $\epsilon(k_\perp)$, and a distance r between the electron and the photohole. The resulting modified Rydberg binding energies are then

$$E_{ex}(n) = \frac{\mu^*}{m_e \cdot \epsilon(k_\perp)^2}\frac{1}{n^2}E_{Rydberg} \qquad n = 1, 2, 3, ... \tag{31}$$

with $E_{Rydberg} = 13.605$ eV, a reduced mass μ^*, defined by $(1/\mu^*) = (1/m_e^*) + (1/m_h^*)$ and the calculated dynamic polarizability $\epsilon(k_\perp) = 19$ along the nickel [111]-direction [71], produced by screening of the photo excited electron in the interface state at $k_\perp = 1.55$ Å^{-1}. Together with the free electron like nature of the interface state electrons with effective mass $m_e^* = 1m_e$ and an effective hole mass $m_h^* = 3m_e$ in the rather flat nickel $3d$-bands, one can estimate the largest $n = 1$ excitonic binding energy to be 28 meV. This value is smaller by one order of magnitude than the measured difference in binding energy. However, the discrepancy may be explained by the localization at the surface and the corresponding stronger overlap of the single particle wave functions of the excited electron and the photohole. Rohlfing and Louie [66] calculated for the (2×1) reconstruction of a Si(111) surface an excitonic binding energy $E_{ex} = 0.26$ V at the surface which is to be compared to the value of 0.015 eV for the bulk.

Combining the Coulomb potential in Eq. 30 and the influence of the periodic crystal potential on the electron-hole pair with reduced mass μ leads to a rather delocalized Mott-Wannier exciton description of the quasiparticle electron-hole excitation. The corresponding eigenfunctions should then be wave packets consisting of Bloch functions of the interface state and of the nickel d-bands with an envelope function ψ_n. The energy eigenvalues E_n can be obtained by solving the hydrogen-like Schroedinger equation [70] for ψ_n

$$\left(-\frac{\hbar^2\nabla_r^2}{2\mu}-\frac{e^2}{\epsilon|\mathbf{r}|}\right)\psi_n=\left(E_n-E_{cb}-\frac{\hbar^2\mathbf{k}^2}{2(m_e^*+m_h^*)}\right)\psi_n$$

where E_{cb} is the binding energy of the conduction band bottom. Thus the Rydberg-like series can be written as

$$E_n\left(\mathbf{k}\right)=E_{cb}-\frac{\hbar^2\mathbf{k}^2}{2(m_e^*+m_h^*)}-E_{ex}(n)\qquad n=1,2,3,... \tag{32}$$

However, comparing the measured dispersion of the interface state band with the one expected from Eq. 32 reveals an inconsistency between the measured effective mass $m^* = 1.08\cdot\ m_e$ and $(m_e^*+m_h^*) = 4\cdot m_e$ as expected from the exciton binding energy calculation in Eq. 32.

This is indeed an argument against an excitonic excitation in the interface state. Note that the finding of an almost free electron like dispersion is also in contrast to the non-dispersive behaviour of the well known charge-transfer excitons in organic semiconductors [7] and excitonic bands on bare silicon surfaces [67].

But on the other hand the effective mass of the interface state seems to depend on the photon energy of the pump pulse and changes from a value of $0.43\cdot m_e$ to a value of $1.08\cdot m_e$ by increasing the pump photon energy from 1.55 eV to 2.7 eV (Table 4). Within the framework of an exciton excitation this finding is consistent with an increasing effective mass m_h^* for increasing binding energies of the photoholes. Systematic measurements of the dispersion relation within the photon energy range of resonant interface state excitation could clarify this argument further.

4.3.1 Conclusion

2PPE experiments allow to tackle the binding energy and the dispersion of an unoccupied interface state on an atomically flat *h*-BN layer on Ni(111) by means of resonant excitation from the bulk 3*d*-bands of the Ni substrate. DFT calculations and dielectric continuum model calculations both predict the existence of such an interface state. In the case of DFT calculations the state is spatially located between the *h*-BN layer and the Ni surface and in the case of the dielectric continuum model the state is predicted to be at the BN-vacuum interface, respectively.

A large binding energy difference of 190 meV between IPS and 2PPE measurements raises speculations about an excitonic pairing of the interface electron with the remaining photohole in the Ni *d*-band, leading to an enhanced binding energy in the case of 2PPE. However, this assumption is not supported by the almost free electron like dispersion of the interface state and the relatively long lifetime of 110 fs [46] compared to typical hole-lifetimes in transition metals.

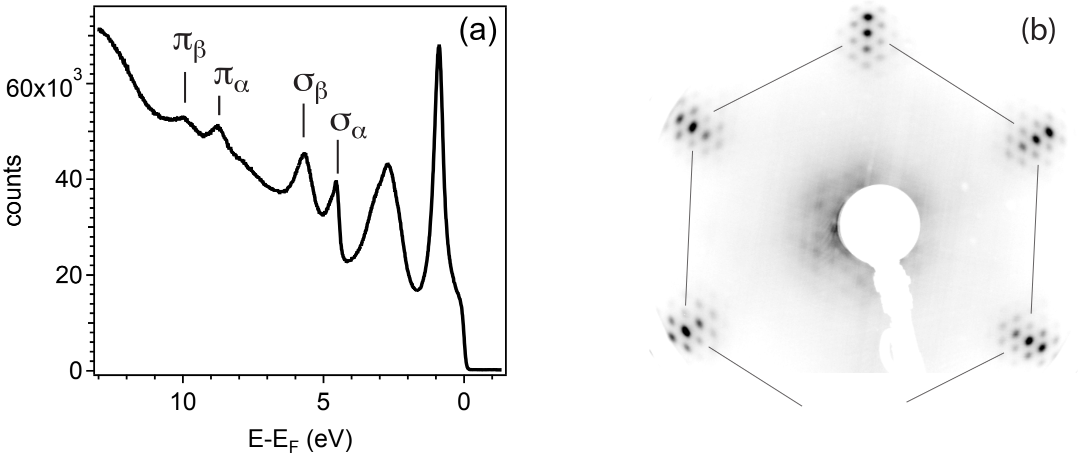

Figure 27: (a) Normal emission UP spectra from *h*-BN/Rh(111) taken with $h\nu = 21.21$ eV. Band splitting into σ_α and σ_β, as well as into π_α and π_β at $\overline{\Gamma}$ due to the corrugated superstructure is clearly visible, as investigated in detail in Ref. [48, 78]. (b) LEED pattern, for an electron energy of 60 eV, revealing the principle spots of the Rh(111) substrate, each one being surrounded by the nanomesh supperlattice spots.

4.4 Interface states on the *h*-BN/Rh(111) nanomesh?

Different hexagonal boron nitride (*h*-BN) monolayers grown on the hexagonal (111) surfaces of transition metals, such as on Ni [42–44], Rh [48, 72], Ru [73, 74], Pd [75] and on Mo(110) [76], have been investigated in the past few years.

Unlike the flat boron nitride single layer on Ni(111), already introduced in this chapter, a different lattice mismatch and bonding strength between the *h*-BN layer and the metal substrate lead in the case of Rh(111) to a self-assembled hexagonal network with a large periodicity of 3.2 nm and a pore or hole size of 2 nm [48]. The strongly corrugated (0.55 Å) *h*-BN layer on the Rh(111) surface has theoretically been modeled by means of DFT calculations, revealing a competition between metal-BN attraction and the elastic properties of the insulating *h*-BN layer as cause for the given final geometry [77]. The experimentally observed splitting of the BN σ band and BN π band into two sub-bands, separated by roughly 1 eV from each other at the $\overline{\Gamma}$-point (Fig. 27 (a)), is directly related to the corrugation [48, 78]. σ_β and π_β found at higher binding energies stem from the BN sites which are closely attached to Rh (*pores*), while σ_α and π_α belong to the more weakly bonded BN sites (*wires*). The resulting splitting is saturated at a bonding length difference of 0.55 Å [77], in good agreement with the found height differences of the corrugation in the STM studies.

In analogy to the splittings found in the occupied electronic structure of *h*-BN one might expect similar signatures in the unoccupied band structure. First spectroscopic and time-resolved experiments [79] indicate the existence of an unoccupied state with a binding energy of 1.4 eV above the Fermi level at $\overline{\Gamma}$. Unfortunately the signal was rather weak due to a non-resonant

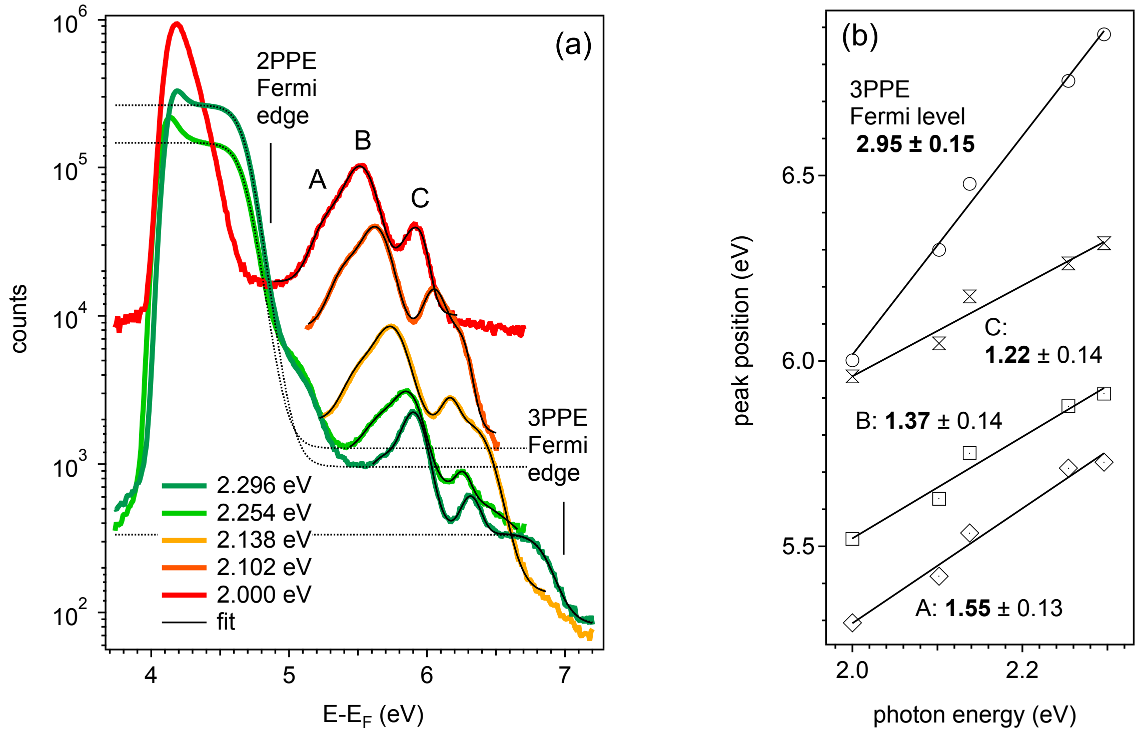

Figure 28: (a) Monochromatic 3PPE spectra from *h*-BN/Rh(111) for different photon energies between 2 eV and 2.3 eV, measured at the VG ESCALAB 220 [23]. Note that the logarithmic plot of the measured 3PPE spectra reveals a rather large dynamic range of 4 orders of magnitude. (b) Fitted Gaussian peak positions as a function of photon energy $h\nu$. The fitted slope of 3 corresponds to direct 3PPE from the Rh(111) Fermi edge via virtual intermediate states. Three peaks labeled with A, B and C reveal slopes between 1 and 2 and can thus be identified as unoccupied intermediate states of *h*-BN/Rh(111).

excitation by means of a fundamental photon from a Ti:sapphire pulse with an energy of 1.554 eV and subsequent probing with the corresponding SH photon (3.108 eV). According to the Rh(111) bulk band structure measured in Ref. [80] one might speculate that this state could be resonantly pumped by means of 2 eV photons from an occupied Rh surface resonance band, lying 0.6 eV below E_F at the zone center $\overline{\Gamma}$.

Indeed the 3PPE spectra in Fig. 28 (a), for a single photon energy between 2 eV and 2.3 eV, reveal three peaks, denoted as A, B and C. The peaks were fitted by means of three Gaussians and a Fermi function (Fig. 29 a). The peak positions are plotted as function of the single photon energy $h\nu$ (Fig. 28 b). The linear slopes of 1.55(13), 1.37(14) and 1.22(14) indicate the unoccupied character of states A, B and C which are either pumped by $h\nu$ and subsequently probed by $2\times h\nu$, or pumped by $2\times h\nu$ and subsequently probed by $h\nu$, respectively. The corresponding possible binding energies above E_F are summarized in Table 5 and marked as horizontal lines in Fig. 29 (b).

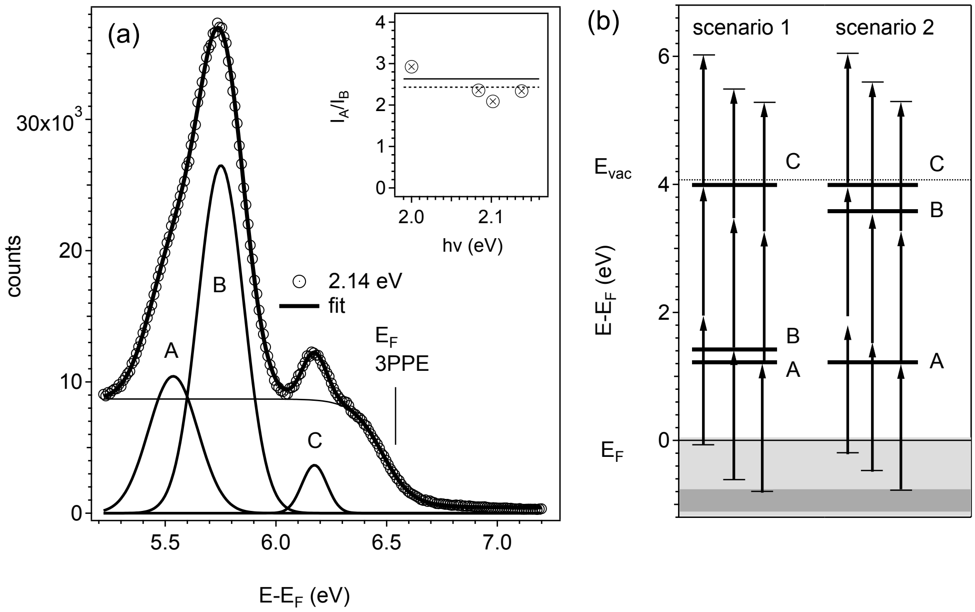

Figure 29: (a) Monochromatic 3PPE spectrum for $h\nu = 2.14$ eV, decomposed into three Gaussian peaks A, B and C and a Fermi-Dirac distribution. *Inset*: plot of the ratio between the integrated intensity of peak B and A measured for four different photon energies between 2 eV and 2.14 eV. The obtained mean value (*dashed line*) of 2.43(25) is close to the measured ratio between σ_β and σ_α of 2.63(2) on h-BN/Rh(111) by Corso et al. [48, 78]. (b) Schematic energy level overview, obtained from the measurements in Figs. 28 (a) and (b).

Two possible scenarios will be presented in order to explain the origin of the three peaks.

	2P probe: E-E$_F$ (eV)	1P probe: E-E$_F$ (eV)	slope: E vs. $h\nu$	m* (m$_e$)
A	1.22	3.38	1.55(13)	-
B	1.42	3.58	1.37(14)	1.045(9)
C	1.84	3.99	1.22(14)	0.91(6)

Table 5: Possible binding energies of the measured features A, B and C for a direct 2PPE (*first column*) and for a 1PPE probing process (*second column*), respectively. In the *third column* the slopes of the linear energy shifts with photon energy $h\nu$ are listed, obtained from the fits in Fig. 28 (b), while the *last column* contains the effective mass, measured in Fig. 30.

First scenario: Peaks A and B could possibly be identified as interface states. In analogy to the presence of a single layer of *h*-BN on a Ni(111) surface, as discussed in Sec. 4.2, one could expect a similar interface state for *h*-BN/Rh(111), spatially located in between the top layer of the Rh(111) surface and the *h*-BN layer. Furthermore corrugation induced splitting of the occupied σ and π bands allows to speculate about a possible splitting of the unoccupied interface state on *h*-BN/Rh(111) which would explain the appearance of two peaks in the spectrum instead of only

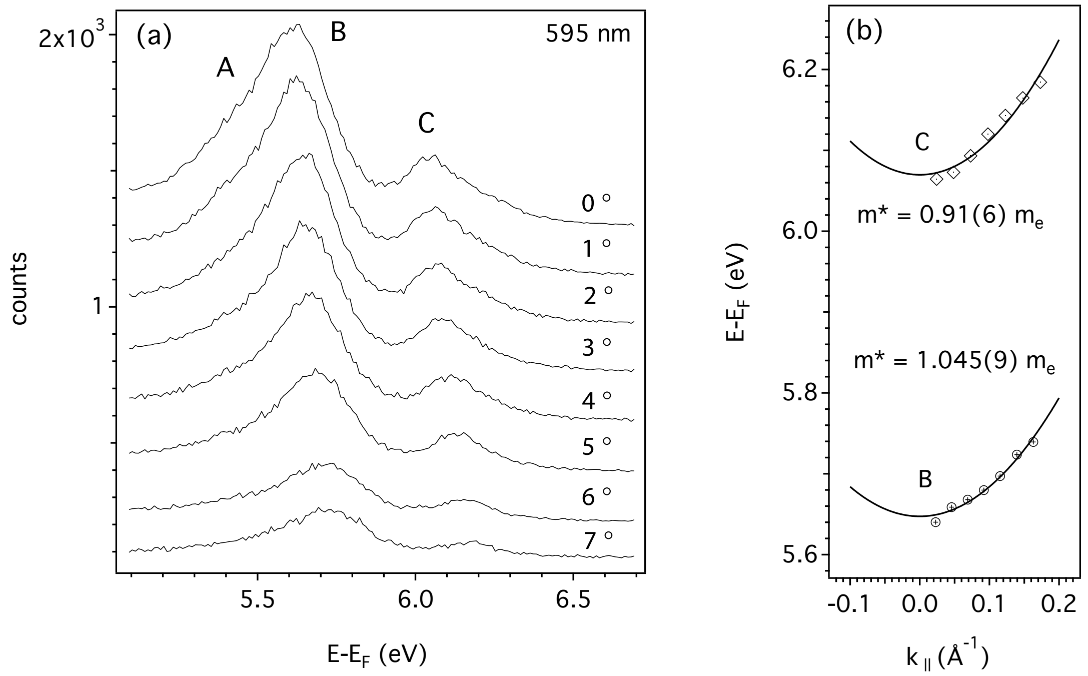

Figure 30: (a) Monochromatic 3PPE spectra (2.084 eV; 595 nm) for different polar emission angles θ between 0° and 7° taken with a bias voltage of -10 V. (b) Fitted peak positions of the unoccupied bands B and C as function of parallel electron momentum $k_{||}$ along $\overline{\Gamma}$-$\overline{M}$ and corresponding parabolic dispersion fits, leading to an effective electron mass of $m^*(B) = 1.05(1) \cdot m_e$ and $m^*(A) = 0.91(6) \cdot m_e$, respectively.

one.

Several indications such as the binding energy, the integrated photoelectron intensity ratio between peaks A and B, as well as the measured effective mass for peak A in angle resolved 3PPE can be used to verify this assumption: In the case of a 2PPE probing process the energy position above E_F of 1.22 eV for peak A and 1.42 eV for peak B in Table 5 would be rather close to the value of 1.5 eV found for the unoccupied interface state on *h*-BN/Ni(111). Furthermore, Corso *et al.* found a ratio of 2.63(2) between the integrated photoelectron intensity of the σ_β (pores) and the σ_α (wires) bands at $\overline{\Gamma}$ [48, 78]. Note that the mean ratio of 2.43(25) between the integrated intensities of peaks A and B for four different photon energies between 2 eV and 2.14 eV (inset of Fig. 29 a) is close to that value. Last but not least the extracted effective mass $m^* = 1.05(1) \cdot m_e$ of peak B from the parabolic dispersion (Fig. 30 b) matches quite well the one from *h*-BN/Ni(111) of $m^* = 1.05(2) \cdot m_e$ obtained from IPE and $1.08(1) \cdot m_e$ from 2PPE. The origin of peak C is not clear. The photon energy dependence of the peak position in Fig. 28 reveals a slope of 1.22 which suggests that the appropriate intermediate state is initially pumped by two photons and subsequently probed by absorption of one photon. In this case, the energy position would then amount to 3.99 eV above E_F, in close proximity of the vacuum level E_{vac} at 4.07 ± 0.01 eV above

E_F (shown in Fig. 29). Still under the assumption that peak A and B belong to a pair of splitted interface states, peak C could be explained by the presence of unoccupied bands of h-BN close to the vacuum level. DFT calculations of a system consisting of 7 layers of Rh(111) between 4 layers of h-BN (two on each side), shown in Ref. [79], are well reproducing the occupied σ and π bands and reveal a series of BN-related unoccupied states. One predicted state with the band bottom at 3.84 eV above E_F and almost free electron like effective mass would be a good candidate for peak C.

Second scenario: The large Rh bulk band gap along $\bar{\Gamma}$-$\bar{L}$ between 0.89 eV and 8.65 eV above E_F, calculated in Ref. [81], would in principle allow the existence of a discrete Rydberg series of image potential states (IPS) on the Rh(111) surface. With respect to E_{vac} the binding energies of peaks B and C amount to 490 meV and 80 meV respectively. Considering Eq. 29 for the energy eigenvalues of the Rydberg series of image potential states on a bare metal surface and the correction factor (ϵ-1/ϵ+1) [15] in the case of a dielectric overlayer with $\epsilon_{\perp} = 5$ [82] and an empirical quantum defect $a = 0.08$ leads to resulting binding energies of 485 meV and 130 meV for the $n = 1$ and the n = 2 IPS, respectively. However, this approach would not explain the origin of peak A.

Summary Surface morphology and electronic characteristics of the h-BN layers strongly depend on the given substrate. In contrast to the flat h-BN/Ni(111) system, h-BN forms a corrugated superstructure on Rh(111), which is also reflected in the electronic structure of the occupied BN-related states. According to the interpretation in the first scenario 3PPE investigations on h-BN/Rh(111) give evidence for the existence of a split pair of interfaces states in analogy to the split occupied σ states. This finding is supported by the measured binding energies, the found dispersions and the relative ratio of both spectral features. However, a second scenario arguing that two of the three peaks belong to the series of image potential states, can not fully be excluded at the present status.

---

[15] Note that the correction factor (ϵ-1/ϵ+1) amounts to 1 in the case of an ideal metal with ϵ = -∞ and thus can be neglected for most bare metal surfaces.

4.5 Disentanglement of electron dynamics and space-charge effects

The following Section contains the published manuscript of: D. Leuenberger, H. Yanagisawa, S. Roth, J. Osterwalder and M. Hengsberger, *Disentanglement of electron dynamics and space-charge effects in time-resolved photoemission from h-BN/Ni(111)*, Physical Review B **84**, 125107 (2011), DOI: 10.1103/PhysRevB.84.125107

The transient structural, electronic and magnetic responses of a condensed-matter system to the pertubation by intense femtosecond pulses have been successfully studied by time-resolved photoemission (TR-PE) in numerous experiments. Prominent recent examples are the transient melting of a charge density wave in $TbTe_3$ [83], the photo-induced vaporization of a charge-ordered state in 1T-$TiSe_2$ [84,85] and the ultrafast demagnetization in ferromagnetic thin films of nickel [12] or cobalt [13]. In all these studies, the system is excited by an intense (usually infrared) light pulse and the evolution of the spatial, electronic or magnetic structure is subsequently probed by means of a second-, fourth-, or higher-harmonic pulse with photon energies between 3 eV and 43 eV. Moreover attosecond streaking experiments on solid surfaces [86] also deal with high fluences in the order of several mJ/cm^2.

At such high excitation densities a high photoelectron background due to direct multi-photon absorption from the infrared pump pulse severely distorts the spectra in time-resolved experiments. On their drift to the detector after emission, all electrons interact strongly, exchanging kinetic energy due to mutual Coulomb repulsion. This leads to shifts and broadening of the spectral distribution, a phenomenon called space-charge effects. Previously, Siwick and co-workers studied quantitatively the effects of Coulomb repulsion in propagating charged clouds in electron guns [36]. The velocity and, thereby, temporal broadening of such electron pulses limits the time resolution in time-resolved electron microscopy or time-resolved electron diffraction experiments. More recently, Passlack *et al.* measured the $\sqrt{N}$ dependence (N denotes the number of simultaneously emitted electrons) of the spectral broadening of a Shockley surface state on Cu(111) with angle-resolved photoelectron spectroscopy [37]. Similar observations were made in experiments using undulator based 3rd generation synchrotron radiation [87] or free-electron lasers [88,89], where in particular high-brilliance free-electron laser sources provide photons in the extreme ultraviolet up to the soft x-ray regime with extremely high pulse densities and high photoelectron yields.

The goal of the present work is to disentangle space-charge effects from the underlying dynamics probed in multi-photon transitions from a model system on a femtosecond timescale. Two-color pump-probe experiments were carried out with intense infrared (800 nm, 'red') pump pulses at a fluence of 3 mJ/cm^2 and frequency-doubled ('blue') probe pulses. The investigated system is a Ni(111) surface covered by a perfectly lattice-matched monolayer of hexagonal boron nitride h-BN. The unoccupied electronic structure of h-BN/Ni(111) has recently been studied in our group by means of time-resolved two-photon-photoemission (TR-2PPE) [46] and by spin-resolved inverse photoemission (SR-IPE) [45]. Two distinct intermediate states between the Fermi level and the vacuum level have been detected in 2PPE, both populated by excitation from the $3d$-bands of

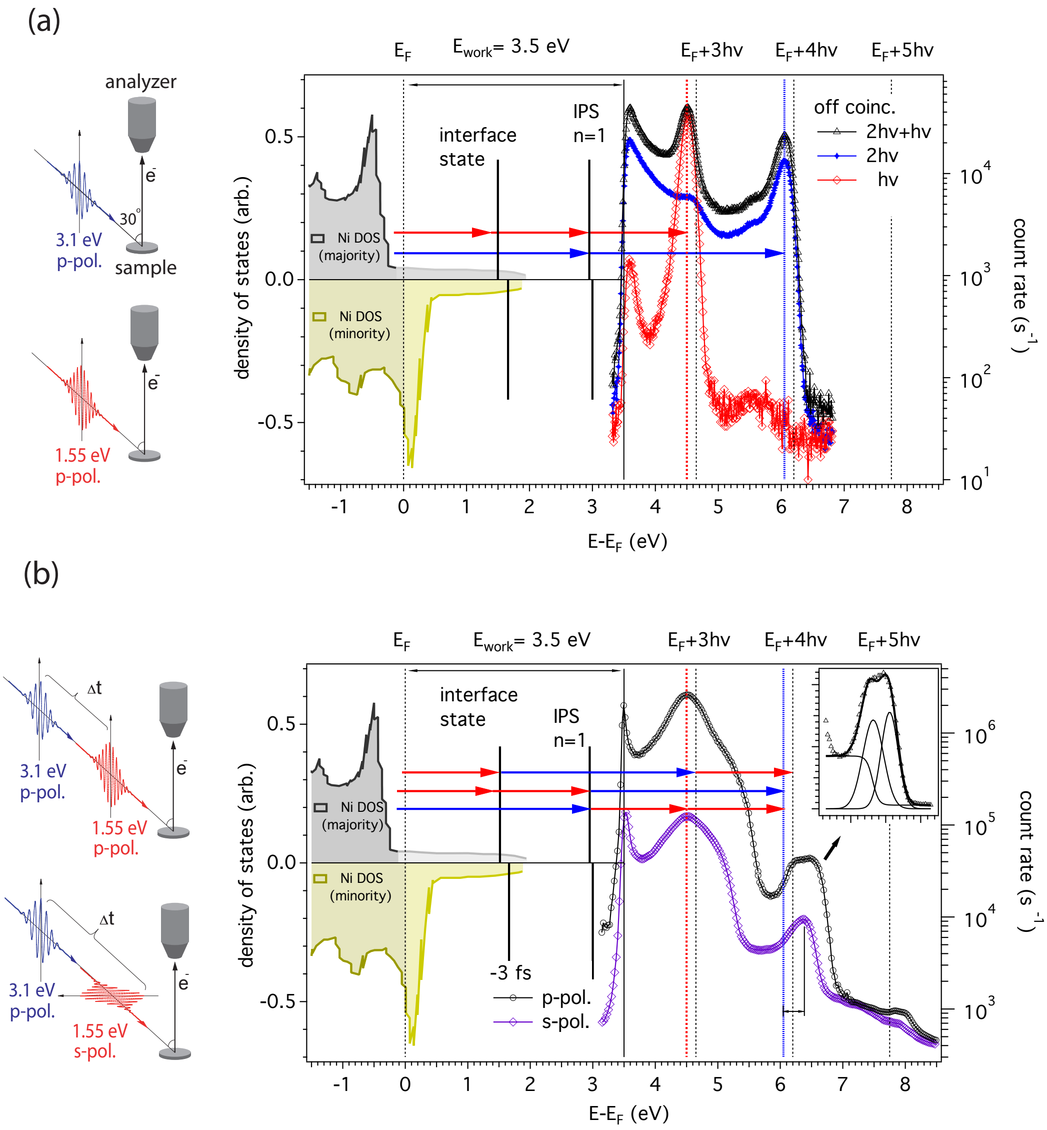

Figure 31: Spectra and direct transitions. Left-hand-side: measurement geometry with the corresponding light polarization. Right-hand-side: a) Monochromatic photoelectron spectra at $\bar{\Gamma}$ for p-polarized fundamental light (1.55 eV; open diamonds), p-polarized SH light (3.1 eV; open circles) and a bichromatic spectrum using both wavelengths for large time delay (open triangles). b) Bichromatic photoelectron spectra at zero delay between the p-polarized SH pulse and the intense fundamental pulse (open circles p, open squares s-polarized light). The initial states (occupied DOS of Ni) and the unoccupied intermediate states of the indicated multi-photon transitions are given. Inset: In the case of the p-polarized fundamental the IPS signal exhibits two peaks (fitted by two Gaussians). The low energy peak corresponds to an excitation via the IPS, the one at higher kinetic energy via the interface state.

Ni(111). One of these intermediate states is the *n=1* image potential state (IPS) of the nickel substrate with a remarkably long lifetime of 261 fs, the other one is a h-BN-derived interlayer or interface state with a lifetime of 107 fs [46].

4.5.1 Spectroscopy

The *monochromatic* 2PPE spectrum of h-BN/Ni(111) taken at normal emission with blue light exhibits two peaks (see Fig. 31 (a)), which were previously investigated by Muntwiler et al. [46]. The first one at 6.1 eV and the second one at 4.65 eV above E_F are both pumped from the initial states Λ_1 and Λ_3 lying in the bulk d-bands of nickel into the IPS and the interface state, respectively. Owing to the large band gap of more than 5 eV, the occupied σ and π valence bands of h-BN are out of reach of the experiment. The populated IPS is subsequently probed by absorption of a second photon as indicated by two horizontal arrows in Fig. 31 (a).

The second peak at 4.65 eV above E_F corresponds to a h-BN related unoccupied interface state theoretically predicted by density-functional theory (DFT) [43, 60–62] and discussed in detail in the previous Sec. 4.2.

A similar spectrum is obtained if only red light is used: here the low photon energy of 1.55 eV implies that only three- and four-photon processes contribute to the spectrum shown in Fig. 31 (a). At 4.51 eV a fairly strong feature shows up, which according to its energy position could involve both, the IPS and the interface state. The bichromatic spectrum shown on top in Fig. 31 (a), was taken using photons of both wavelengths, but for large time delays between both pulses in order to suppress all processes involving both wavelengths. As a consequence, the spectrum represents the sum of both monochromatic spectra.

4.5.2 Time-resolved experiments

In Fig. 31 (b), data are shown which were taken for both, pump and probe pulses arriving at the same time on the sample, that is at zero delay. Three striking differences with respect to the data off coincidence, *e.g.* for large delay as in Fig. 31 (a), can be observed: First, the intensity at 4.51 eV is greatly enhanced, second a broad shoulder of extra intensity is piling up at its high energy side. The third observation is that the position of the IPS peak is shifted from 6.1 eV to 6.4 eV. Moreover, in the spectra taken with p-polarized pump light in Fig. 31 (b), the peak splits into two components as shown in the inset of Fig. 31 (b).

Regarding the dominant feature appearing at 4.51 eV, we note that the difference in energy between the IPS and the interface state is 1.42 eV, hence close to the fundamental photon energy of $h\nu = 1.55$ eV (see discussion above). This means that two possible excitation pathways lead from the very same initial state to the same final state, as already conjectured in Ref. [46]: one channel corresponds to a $red - blue$ process via the interface state, the second passing through the IPS in a $blue - red$ sequence. Interference between both channels leads to a strong resonance observed in the data shown in Fig. 31 (b). For the following it is important to note that the overall yield strongly increases for p-polarized pump light when pump and probe pulses overlap temporally, the same being true but to less extent for s-polarized pump light.

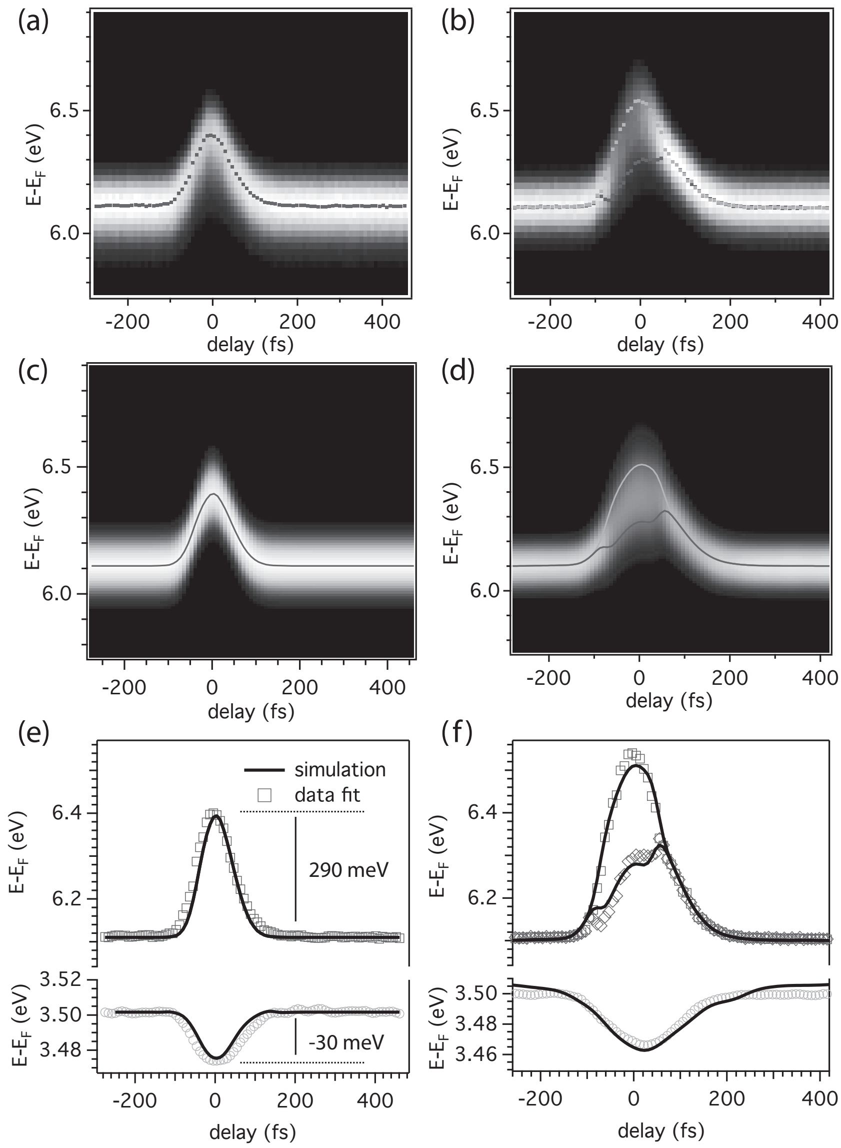

Figure 32: Greyscale plot of the photoemission intensity and corresponding simulations from the IPS as function of final state energy (vertical axis) and time delay with respect to s-polarized (data in (a), simulations in (c)) and p-polarized (b, d) fundamental pump pulses. The peak positions as found by fitting Gaussians, are superimposed as solid symbols. In the bottom panels, the fitted energy positions of the peaks and of the secondary cut-off (open circles) are plotted as function of time delay for s-polarized (e) and p-polarized (f) pump pulses together with the results of the space-charge simulations (solid lines).

In the following discussion of the time-resolved data, we will mainly focus on the feature around 6.1 eV. The spectra are plotted against energy and time delay for s- and p-polarized pump light in Fig. 32 (a) and (b), respectively. Again, around zero delay the position of the peak shifts towards higher energy and recovers approximately 200 fs after the pump pulse. In the data taken for p-polarized pump light in Fig. 32 (b), the intensity of the IPS apparently decreases for small negative delays giving rise to the double-peak structure already observed in Fig. 31 (b). The two peaks are separated by 235 meV at delay zero. Anticipating the results of the simulations, the one at lower kinetic energy belongs to a $blue - blue$ transition via the IPS, whereas the one at higher energy to a $red - blue - red$ transition via the interface state, which appears at slightly higher energy (see Fig. 34). Both peaks shift towards higher energy for small delays. While the hot-carrier dynamics associated with the high excitation density were the target of this study, the fact that many electrons (of the order of one thousand per pulse) are emitted simultaneously implies that the energy shifts are caused by Coulomb interactions during the drift of the photoelectrons to the detector. In order to recover the underlying dynamics in the solid, a model was developed to account for such space-charge effects.

4.5.3 Space-charge disk model

For a quantitative analysis of the effects related to Coulomb repulsion during the drift to the detector, we recorded the photoelectron spectra using blue pulses for delays in the range between -280 fs and 420 fs with respect to a *s*-polarized (Fig. 32 (a)) and a *p*-polarized red pump pulse (Fig. 32 (b)). In the very first instance, when all electrons are released from the sample within roughly the duration of the probe pulse, each electron experiences some acceleration depending on the precise moment of emission. Since the latter is a result of a stochastic process, the energy distribution is only broadened. At later stages during drift, the spatial distribution of the electron cloud represents the velocity distribution, *e.g.* the spectrum. In a simplified picture the fastest electrons are pushed forward by the space charge cloud behind, while the slowest electrons are decelerated by the space charge in front. Therefore, the net acceleration depends on the longitudinal spatial position of the electrons and, thereby, on the velocity or else the kinetic energy of the electrons.

As a result, the kinetic energy of the IPS gradually shifts towards higher energies and the total energy shift depends on the absolute number of electrons emitted simultaneously. The total shift of the IPS reaches its maximum for delays at which the photoyield is the highest, *e.g.* close to zero delay: $\Delta E_{kin} = E_{kin}(0\text{ fs}) - E_{kin}(-300\text{ fs}) = 290$ meV, as plotted in Fig. 32 (e). At the same time, the maximum of the inelastically scattered secondary electrons is shifted in the opposite direction ($\Delta E_{kin} = -30$ meV) upon going from negative delays to 0 fs and fully recovers for positive delays $\Delta t > 300$ fs.

To model these space-charge effects for each delay step Δt, we sliced the photoelectron spectrum into a series of 2D disks [36,37] with the thickness given by the kinetic energy spread in each disk and with the radius $R = 50\,\mu$m corresponding to the laser beam waist on the sample taking into account the second order nonlinearity of the 2PPE process [37]. The cartoon in Fig. 33 (a) and 33 (b) depicts three of them, the fastest disk for the IPS, the central one for the resonance at 4.51 eV and the slowest disk for the secondary electrons. In the simulation *e.g.* the IPS was sliced into 91 disks corresponding to energy steps of 18 meV between two neighboring disks.

The total charge and the charge density $\rho(\Delta t)$ of each disk was computed from the measured total sample current I_{sample} and the measured photoelectron spectrum $A(E, \Delta t)$ for each delay

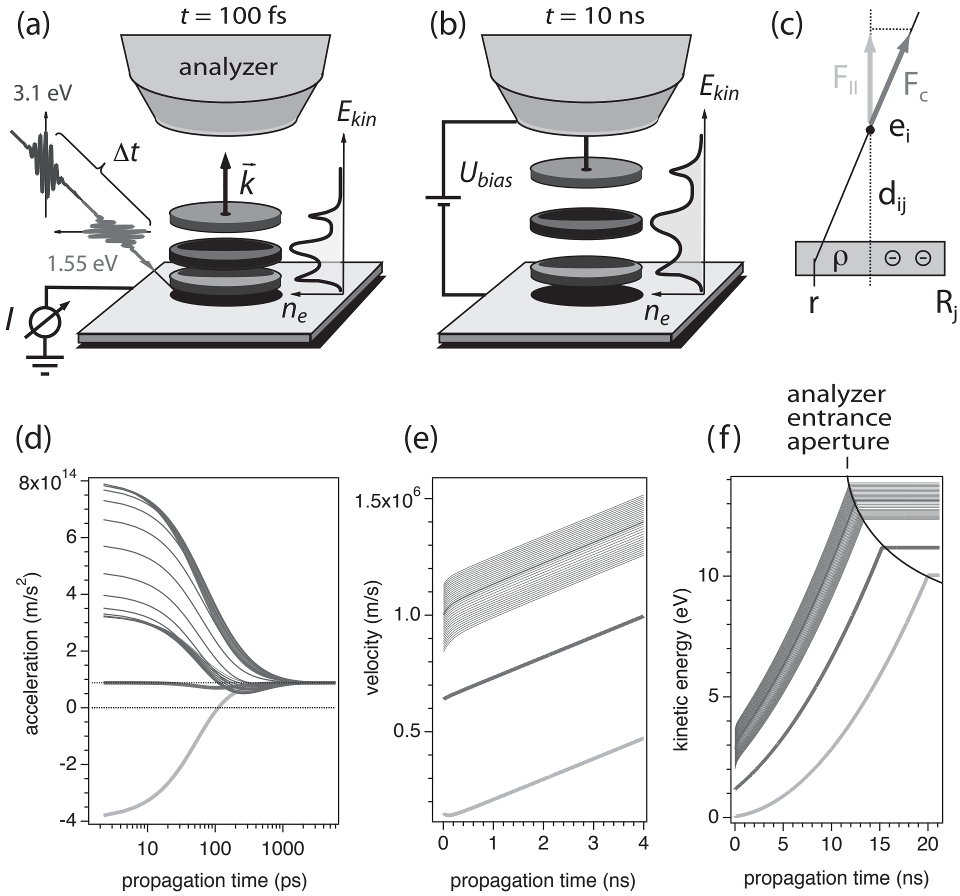

Figure 33: Simplified sketch of the space-charge model. The three dominant spectral features are represented by charged disks of photoemitted electrons corresponding to the IPS transition (top most disk, highest velocity), the resonant transition at $E_F + 3h\nu$ (center disk) and the inelastically scattered electrons from the secondary cut off (slowest disk) directly after emission (a) and after 10 ns drift (b). (c) Superposition of the repulsive coulomb forces amongst all the spectral features along the propagation direction to the analyzer leads to space-charge induced broadening and energy shifts of the photoelectrons, exemplified here as the Coulomb force exerted by a space charge disk with radius R and charge density ρ onto a single electron e^- at a distance d. Calculated acceleration (d), velocity (e) and kinetic energy (f) of the IPS (upper trajectories), the resonance at 4.51 eV (central trajectory) and the secondary electrons (lowest trajectory) as function of propagation time towards the analyzer. For the IPS, all single trajectories are shown, for the other disks, only the motion of the center of gravity is plotted for the sake of clarity.

step Δt. Starting point for each delay Δt were energy positions of the three peaks according to a spectral distribution measured off coincidence (Δt <-200 fs) and hence at a non-distorted low fluence condition. The relative intensity of the three spectral features for the simulation, namely, the IPS, the resonance, and the secondary cut off at a certain delay Δt have then been obtained from the measured delay dependent photoelectron intensities $A(E, \Delta t)$. For each of the three spectral features integration over the distinct spectral range leads then to the delay dependent spectral weight $\omega(\Delta t)$ of the particular feature *e.g.* for the IPS:

$$\omega(\Delta t)_{IPS} = \frac{\left[\int_{5.8\ eV}^{7.2\ eV} A(E,\Delta t) dE\right]}{\left[\int_{0}^{\infty} A(E,\Delta t) dE\right]}. \tag{33}$$

Finally the total number of photoelectrons per delay step Δt given by the measured sample current $I_{sample}(\Delta t)$ has been distributed amongst all the slices in the weighted spectrum. As an example, a current of 78 pA at zero delay and 250 kHz repetition rate corresponds to $N = 1950$ photoelectrons per pulse.

The initial angular distribution of the photoelectrons, defined by the opening angle of the emission cone θ_e, and the electron trajectories under the influence of the applied bias field [24] then determine the temporal evolution of the radius $R(t)$ and thus of the charge density $\rho(t)$ on the way to the detector [90]. In a first approximation we neglect the lateral Coulomb repulsion and assume the charge density to be homogeneous over the whole 2D-area [36].

Finally the Coulomb force $F_{c\|}^{ij}$ along the propagation direction exerted by the charge in disk j with radius R_j and comprising a fraction n_j of the total photoelectron yield onto a test electron e_i at a distance d_{ij} (see Fig. 33 (c)) is then given by

$$\begin{aligned} F_{c\|}^{ij}(t) &= \frac{n_j\, e^2}{4\pi\varepsilon_0} \cdot \int\limits_0^{R_j(t)} \int\limits_0^{2\pi} \frac{d_{ij}(t)\cdot r}{(r^2 + d_{ij}^2(t))^{3/2}} \cdot dr\, d\varphi \\ &= \frac{n_j\, e^2}{2\pi\, R_j^2(t)\, \varepsilon_0} \cdot \left(1 - \frac{d_{ij}(t)}{\sqrt{R_j^2(t) + d_{ij}^2(t)}}\right) \end{aligned} \tag{34}$$

In the next time step of the numerical integration, each disk of photoelectrons i is then accelerated by the superposition of all mutual coulomb forces of all disks $j \neq i$ and by the externally applied bias field between sample surface and analyzer entrance aperture ($U_{bias} = -10$ eV over a distance D of 0.02 m):

$$m_e\, a_i(t) = \frac{e \cdot U_{bias}}{D} + \sum_j F_{c\|}^{ij}(t) \tag{35}$$

The initial kinetic energy E_{kin}^i of the photoelectrons just outside the surface was directly taken from spectra taken at low fluence: typically, values of 2.73 eV and 1.11 eV were used for the IPS and the resonance, respectively. The mean energy of the secondary electrons was set to 65 meV. Effects of the attractive image potential on the propagating spectral distribution have been discussed in previous publications [87,88,91] but were neglected in the present work. Acceleration $a(t)$, velocity $v(t)$, position $x(t)$ and kinetic energy $E_{kin}(t)$ were iteratively calculated using Eqns. 34 and 35 for each time step of 2 ps for the drift between sample surface and detector entrance as shown in panels (d) through (f) of Fig. 33. The results of the simulations for time delays between -280 fs and 420 fs are shown in Fig. 32 (c). The calculated shift in kinetic energy $\Delta E_{kin} = 290$ meV and the additional broadening of the IPS by 28 meV between negative and zero delay are in excellent agreement with the experimentally obtained values of 280 meV and 30 meV, respectively. Note that the more complicated case of the p-polarized pump pulse in Fig. 32 (b), (d) and (f) will be discussed in Sec. 4.5.4.

Throughout the simulation, only the opening angle of the emission cone was *a priori* not known, because solely one angle should be used for the whole electron distribution in order to keep the calculations as simple as possible. The simulation was carried out for various values and the values were compared to results of angle-resolved 2PPE data afterwards. We obtained emission cones with opening angles of 6° and 10° for p- and s-polarized pump light, in very good agreement with previous experimental results [46].

As expected from the calculated accelerations in Fig. 33 (d) most of the energy exchange by means of Coulomb repulsion occurs within 1 ns after emission (in agreement with [36,37,85]). The bunch of decreasing trajectories in Fig. 33 (d) represents the energetically sliced IPS into charged sub disks. Intrinsic broadening of the IPS is caused by slightly different slopes within the bunch. All curves shown in Fig. 33 (d) converge asymptotically towards the same value, which is given by the external bias field applied between sample and analyzer entrance aperture. Eventually, it takes then 12 ns for the fastest and roughly 20 ns for the slowest electrons to reach the detector aperture, denoted by bended line perpendicular to the traces in Fig. 33 (f).

4.5.4 Dynamics beyond the space-charge model

The good agreement between the results of the space-charge model and the experimentally observed energy shifts suggests that the space-charge model catches the main physics in the time range within the pulse overlap, when the total yield strongly rises. The observed splitting of the IPS transition for negative delays and p-polarized fundamental infrared light (c.f. Figs. 31 (b) and 32 (b)) cannot be explained, however, by space-charge alone.

In order to get more insight, the spectral distribution between 5.9 and 6.6 eV above E_F was fitted by two Gaussians in the delay range between -80 fs and 60 fs (see the two distinct lines in Fig. 32 (f)). The fact that it essentially appears at negative delays means that the blue photons have to arrive before the red photons for the transition to happen. The only possibility beside the *blue-blue* and the *blue-red-red* transitions, both via the IPS with the same final energy, is given by a *red-blue* transition via the interface state followed by the absorption of another *red* photon in order to be excited to its final energy. Because of the high pump intensity, red photons are abundant as soon as the red pulse turns on. Hence, the peak measured at higher kinetic energy belongs to a *red-blue-red* transition first pumped by $h\nu$ into the interface state and subsequently probed by simultaneous adsorption of a $2h\nu$ and a $h\nu$ photon (sketched in Fig. 34 (a)). The 3PPE transition probability for this process as function of time delay Δt between $h\nu$ and $2h\nu$ is denoted as $P_{h\nu-2h\nu-h\nu}(\Delta t)$. It depends on the lifetime of the interface state ($\tau = 107$ fs) and the temporal widths of the two pulses.

Assuming the second peak component to be the result of the additional 3PPE transition we can write the transition probability by means of the intensity correlation function of the pulses as

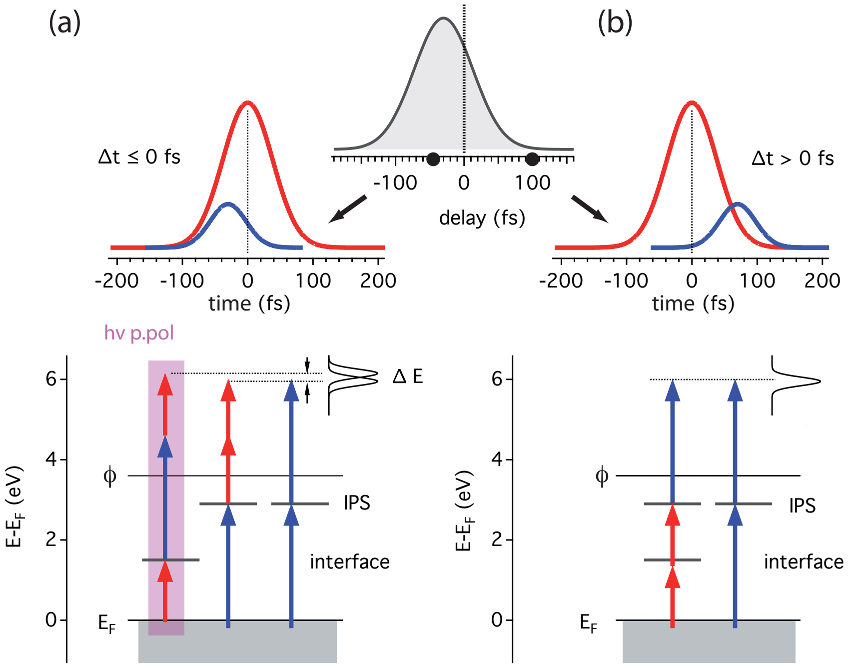

Figure 34: Possible 2PPE and 3PPE transitions with final free photoelectron energies around 6 eV for *p*-polarized fundamental (1.55 eV) and SH (3.1 eV) for small negative (a) and positive (b) time delays between fundamental and SH pulses. The gray shaded curve depicts the transition probability (Eq. 36) for a $red-blue-red$ 3PPE transition involving the interface state like shown by the arrows of the left most transition.

follows:

$$S_0(\Delta t, t_0) \;=\; \int_{t_0}^{\infty} I_{2h\nu}(t-\Delta t)\, e^{-\frac{t-t_0}{\tau}}\, I_{h\nu}(t)\, dt,$$

where $\tau = 107$ fs denotes the lifetime of the intermediate interface state, and finally:

$$P_{h\nu-2h\nu-h\nu}(\Delta t) \;\propto\; \int_{-\infty}^{\infty} I_{hv}(t_0)\, S_0(\Delta t,\, t_0)\, dt_0. \qquad (36)$$

I_{hv} and I_{2hv} are assumed to be Gaussians with full widths at half maximum (FWHM) of 108 fs and 70 fs for $h\nu$ and $2h\nu$, respectively (compare Sec. 2.1.5). Eq. 36 then yields a approximately Gaussian form for $P_{h\nu-2h\nu-h\nu}$ with the peak maximum at -30 fs and an FWHM of 67 femtoseconds (grey shaded areas in Fig. 34). We apply now the space-charge model for $N = 2400$ photoelectrons per pulse at zero delay corresponding to a sample current of 96 pA using the measured spectral distributions as function of delay time Δt and the calculated transition probability $P_{h\nu-2h\nu-h\nu}(\Delta t)$ from Eq. 36 for the 3PPE process. In contrast to the simulation with *s*-polarized red light we add now in the case of a *p*-polarized red pulse a second peak 130 meV above the *blue-blue* transition (via IPS) corresponding to the *red-blue-red* transition (via interface state), weighted in intensity by the distribution $P_{h\nu-2h\nu-h\nu}(\Delta t)$. For an average emission cone of ±6°

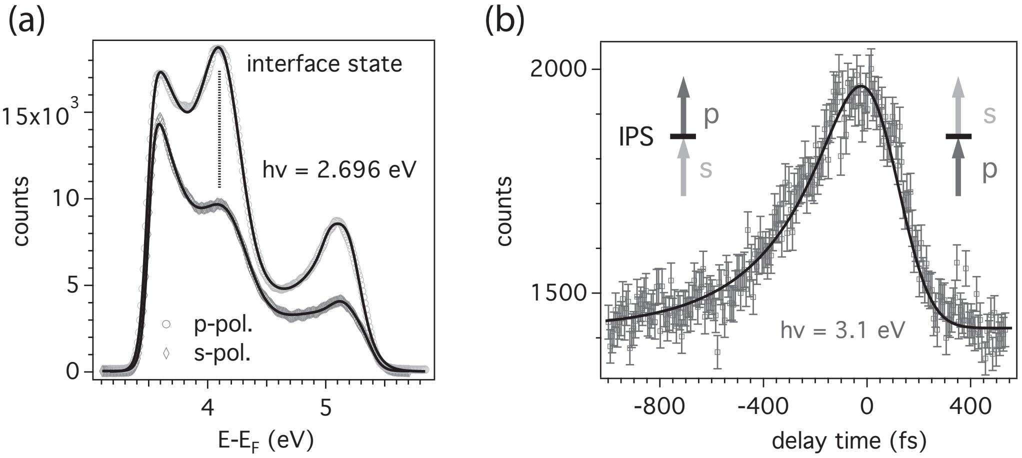

Figure 35: Time-resolved spectroscopy from interface and image potential states. (a) Monochromatic 2PPE spectra taken with either linearly $p-$polarized (open circles) or $s-$polarized (open squares) pulses with $h\nu = 2.696$ eV. The interface state as intermediate state and initial Ni d-states are observed at 4.1 eV and at 5.1 eV above E_F, respectively. (b) Cross-correlation curve of the $n = 1$ image potential state as function of delay between the $s-$ and $p-$polarized SH pulses. The photon sequence is indicated, the solid line is the solution of the rate equation for a lifetime of $\tau = 265$ fs.

opening, the calculation well reproduces the measured data as can be seen from comparing Figs. 32 (b) and 32 (d). Without space-charge effects the final kinetic energy of the *blue-blue* transition and the *red-blue-red* transition would be separated by 130 meV. Mutual Coulomb repulsion between the emitted photoelectrons with slightly different kinetic energy and the slightly different acceleration caused by the other electrons at lower kinetic energy leads to a maximum difference ΔE_{kin} of 235 eV in the experimental data and 230 meV in the simulations for 0 fs time delay. Fig. 32 (f) shows the calculated and measured peak positions of these two features superimposed over the full time scale.

Further evidence for the assumption of a 3PPE process via the interface state comes from polarization dependent measurements. This transition only occurs in the case of a p-polarized red pulse. The measured photoemission intensity is proportional to the square of the matrix element

$$T_{fm} = \langle \psi_f | A \cdot \nabla | \psi_m \rangle,$$

where ψ_m is the intermediate interface state and ψ_f denotes a free-electron final state. Pure hexagonal BN has D_{6h} symmetry [61]. The corresponding interface state belongs to the Γ_1^+ representation in the notation of Robertson [92] and is even under reflection σ_h at the mirror planes [60]. Thus T_{fm} is finite only for p-polarized light [26, 60]. Indeed, monochromatic 2PPE measurements with 2.7 eV photon energy show a strong polarization dependence of both the intermediate interface state and the initial Ni $3d-$bands as can be seen in Fig. 35 (a).

The same approach can be used to disentangle pump and probe pulses in monochromatic 2PPE experiments: The IPS, which has the same parity under reflection at the mirror planes as the interface state, can only be probed using p-polarized light. The pump, however, can be of either polarization, as initial states of different symmetry are available leading to finite momentum matrix elements also for s-polarized excitation [93]. Data for a two-photon sequence of same photon energy but different polarization are shown in Fig. 35 (b): here, negative delays correspond to s-polarized pump and p-polarized probe, and positive delays to the opposite sequence. The transient photoemission intensity is asymmetric with respect to zero delay showing an exponential decay with a time constant of 265 fs towards negative delays. We conclude that the IPS can only be observed using p-polarized excitation light in accordance with our analysis of the interface state above. The time constant is in excellent agreement with the IPS lifetime found in previous experiments [46]. It is noted in passing that as a consequence, the 4PPE transition observed at around 8 eV (*red-blue-red-red* in Fig. 31 (b) can only be detected in the case of a p-polarized fundamental pulse.

Conclusion: Hexagonal boron nitride on Ni(111) represents an excellent model system for two-photon photoemission as it provides two well-separated unoccupied states of different character with high transition matrix elements for low-energy photons of suitable polarization.

In this work we present data taken with multi-photon photoemission under high excitation density. Three- and four-photon processes can be observed at high fluences of typically $> 10^{13}$ photons per pulse or 3 mJ/cm^2. These transitions can be switched on and off by choosing either linearly p- or s-polarized red pulses, respectively, owing to the even parity of the intermediate state wave function under reflection at the mirror planes of the surface. The measured probability amplitude of a particular three-photon transition can be calculated using the known lifetime of the involved intermediate states and the cross correlation width of the femtosecond laser pulses.

Due to the large number of photoelectrons per pulse space-charge related energy shifts of up to about 300 meV occur in the measured spectra. These space-charge distorted spectra can be fully reproduced by simulating the propagation of a charged-disk ensemble representing the energy distribution of the photoelectrons in a simple model as function of pump-probe delay. All input parameters for these calculations can easily be obtained from the experiment itself allowing the underlying electron dynamics inside the solid to be disentangled from the space-charge effects. We anticipate that this kind of data treatment will be essential for future studies using high-intensity streaking fields in attosecond experiments [86] or at free-electron laser sources [88].

4.6 Image potential states as probe for ferromagnetic order

4.6.1 Spin dependent Image Potential States

As already introduced in Sec. 4.1.4 unoccupied image potential states (IPS) can be considered as standing electron waves trapped between a crystal barrier due to a bulk band gap and the barrier associated with the image potential of an electron [52, 94]. They can be found on many metal surfaces, including those of the ferromagnetic $3d$-transition metals [95, 96]. Located a few Angstrom outside a ferromagnetic surface they are sensitive to the surface magnetization [97]. The exchange-split bandstructure of the substrate lifts the spin degeneracy and leads to different energies $E^{\uparrow,\downarrow}$ of image potential states for the two spin directions. At the center of the surface Brillouin zone the binding energies follow closely the Rydberg-like series

$$E_n^{\uparrow,\downarrow} = E_{vac} - \frac{0.85eV}{(n + a^{\uparrow,\downarrow})^2}, \tag{37}$$

with $a^{\uparrow}$ and $a^{\downarrow}$ the spin-dependent quantum defects [98]. Spin-resolved inverse photoemission data for the $n = 1$ IPS on ferromagnetic substrates reveal exchange splittings $\Delta E_{ex} = E\uparrow$ - $E\downarrow$ in the range of 20 to 80 meV [99,100]. These values are supported by polarization-dependent two-photon photoemission experiments [101,102]. In spin-resolved two-photon photoemission studies [97,103] different lifetimes for majority and minority IPS on ferromagnetic Fe and Co thin films have been measured, what gives insight into spin-dependent quasielastic and inelastic scattering processes. Furthermore the temperature dependence of the spin polarization demonstrates that these states are true probes of the near-surface magnetization [49].

4.6.2 Ultrafast demagnetization

An interesting topic in modern solid state physics is the optical excitation of magnetically ordered systems on a femtosecond time scale. Beaurepaire *et al.* reported in 1996 experiments on the magneto-optical behavior of nickel thin films after pulsed laser (60 fs) irradiation [11]. Roughly half of the magnetic moment per Ni atom was lost within the first picosecond. These results have been confirmed by several groups [104, 105]. Since all-optical experiments might be explained by effects other than an ultrafast decrease of the magnetization [106, 107], further methods like time-resolved photoemission [12, 13] and time-resolved x-ray magnetic circular dichroism (XMCD) [15] have been applied in this field to cross check the magneto-optical measurements. For instance it was shown by Rhie et al. [12] by time-resolved photoelectron spectroscopy that the magnetic exchange splitting between majority and minority spin $3d$-bands in a Ni film collapses on a time scale of ~300 fs following a femtosecond laser pulse. The goal of the present work was to verify whether the IPS found in front of a ferromagnetic surface can be used as probe for this ultrafast phenomenon.

Two distinct intermediate states between Fermi and vacuum level have been detected in 2PPE, both populated out of the $3d$-bands of Ni(111) by absorption of low-energy photons. One of these intermediate states is the *n=1* IPS of the nickel substrate with a remarkably long lifetime of

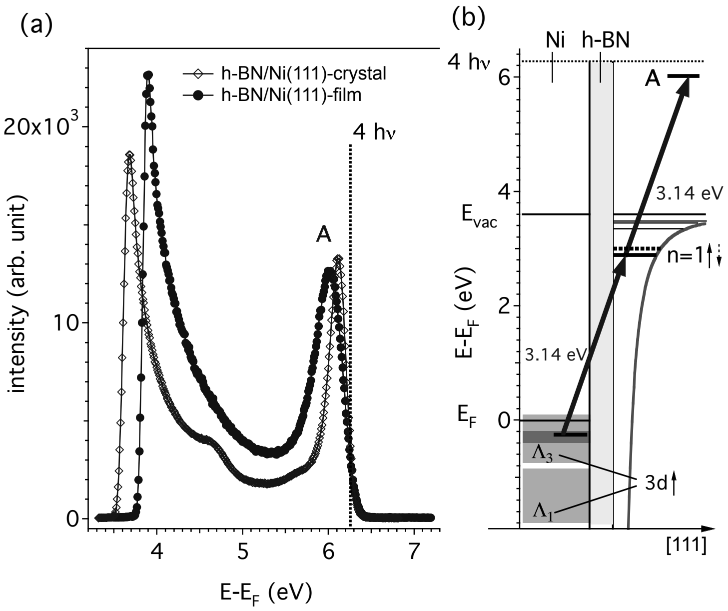

Figure 36: (a) Monochromatic ($h\nu = 3.1$ eV) 2PPE normal emission spectra from a *h*-BN monolayer on a Ni(111) bulk crystal (open diamonds) and on a 80 nm thick Ni(111) Al_2O_3(0001) film with the IPS peak labeled A. (b) Schematic sketch of the observed 2PPE transition with the majority Ni-3*d* band as initial state and the $n = 1$ majority IPS as intermediate state.

270 fs, providing a possible probe for the magnetic state of the surface [46]. Moreover, the h-BN monolayer renders the Ni(111) surface rather inert and permits extended measuring times without surface contamination. In order to suppress the dissipation of the optically deposited energy by ballistic electron transport away from the probed volume [28] and to assure demagnetization of the whole film, an 80 nm thick Ni(111) film grown on Al_2O_3(0001) has been used. While the thicknesses of the ferromagnetic films used in previous ultrafast demagnetization experiments were of the order of a few monolayers up to 15 nm, a compromise was sought between the well defined surface structure of single crystals and the small thickness of strained ultrathin films because the formation of a hexagonal boron nitride monolayer requires a well defined (111) surface structure.

4.6.3 Spectroscopy

In the following the focus will be on a transition from the majority 3*d*-bands of nickel (initial state), via the unoccupied majority $n = 1$ IPS (intermediate state) into a free electron final state by absorption of two blue photons ($h\nu = 3.1$ eV). The 2PPE spectra are shown in Fig. 36 together with the transition scheme. The IPS is labeled with A in Fig. 36. The single crystal spectra are identical to the 2PPE data shown in the preceding chapter but are slightly different for the film sample: The work function of the film (3.855 eV) is higher than the one of the crystal sample (3.6 eV). This is probably due to the higher defect density in the Ni film which might compromise the compactness of the *h*-BN monolayer. Likewise, the secondary electron peak is enhanced in the film sample, masking entirely the small peak at 4.65 eV above the Fermi level which had been attributed to the boron nitride interface state in the h-BN/Ni(111) monolayer system [46].

4.6.4 Temperature dependent data

To test the sensivity of the IPS transition to the magnetism of the sample, series of bichromatic (3.1 eV and 1.55 eV photons) and monochromatic (3.1 eV photons) 2PPE spectra like those depicted in Fig. 37 (a) and (b) were taken while heating up and cooling down the sample through the critical temperature T_c= 631 K of bulk nickel. The energy position of the IPS is plotted in Fig. 37 (c) and (d) against the sample temperature. The curves for both types of samples show a kink close to T_c, which clearly indicates the temperature dependent magnetic phase transition at the Curie temperature T_c at 631 K for the Ni(111) single crystal and at 610 K for the 80 nm thick Ni-film sample.

Above T_c the peak related to the IPS shifts towards higher energies with increasing temperatures (shown in Fig. 37) with a slope of 0.122 meV/K on the single crystal and a slope of 0.057 meV/K on the nickel film. The behavior above T_c corresponds well to a thermally induced energy shift, as previously observed by Paniago *et al.* [108] in the case of the Shockley surface state on Ag(111), and can be reproduced by using the phase model of Echenique and Pendry [52], and Smith [94] for the case of the nickel crystal. Hence the difference between the crystal and the film values can at least partially be explained by invoking the thermal lattice expansion of nickel and sapphire substrate, respectively [49].

Below T_c the collapsing exchange splitting of the $3d$-bands and of the $n = 1$ IPS contributes to the change in peak position, thus producing a kink in the curve. Since the final peak position is dominated by the energy position of the intermediate state, one can determine a magnetic shift of the IPS on h-BN/Ni(111). This magnetic shift is obtained by subtracting the extrapolated thermal shift from the total one and by fitting the resulting data to the magnetization curve of nickel [109], phenomenologically described with $M(T)/M(0) \propto (T_c - T)^\beta$ with $\beta = 0.37$ for bulk nickel at $T \approxeq T_c$, as shown in Fig. 37 (e). In the case of the nickel film the fitted value $\beta = 0.6$ is higher than in the bulk case which is not yet fully understood. The tendency of the observed magnetic shift towards higher energy with increasing sample temperature suggests that the signal has majority character. Indeed preliminary spin-resolved measurements of a resonant two-color 2PPE transition on h-BN/Ni(111), involving the IPS as one of the intermediate states excited by the same photon energy, confirm its majority character [110]. The magnetic shift of 36 meV, observed for the single crystal sample between room temperature and T_c (Fig. 37 e), thus provides a rough estimate of the majority contribution to the exchange splitting of the $n = 1$ IPS on h-BN/Ni(111). The value is of the same order of magnitude as 2PPE results of Fischer *et al.* for the IPS on clean Ni (Δ $E_{ex} < 40$ meV, at $\bar{\Gamma}$) [102] and results of inverse photoemission studies by Passek and Donath [99]. For the 80 nm film sample one obtains a room temperature value of the order of 25 meV by extrapolating the curve of Fig. 37 (f). These data thus demonstrate that the investigated 2PPE IPS transition is sensitive to the ferromagnetic phase change in nickel and may therefore be used to probe laser pulse induced ultrafast demagnetization in this system.

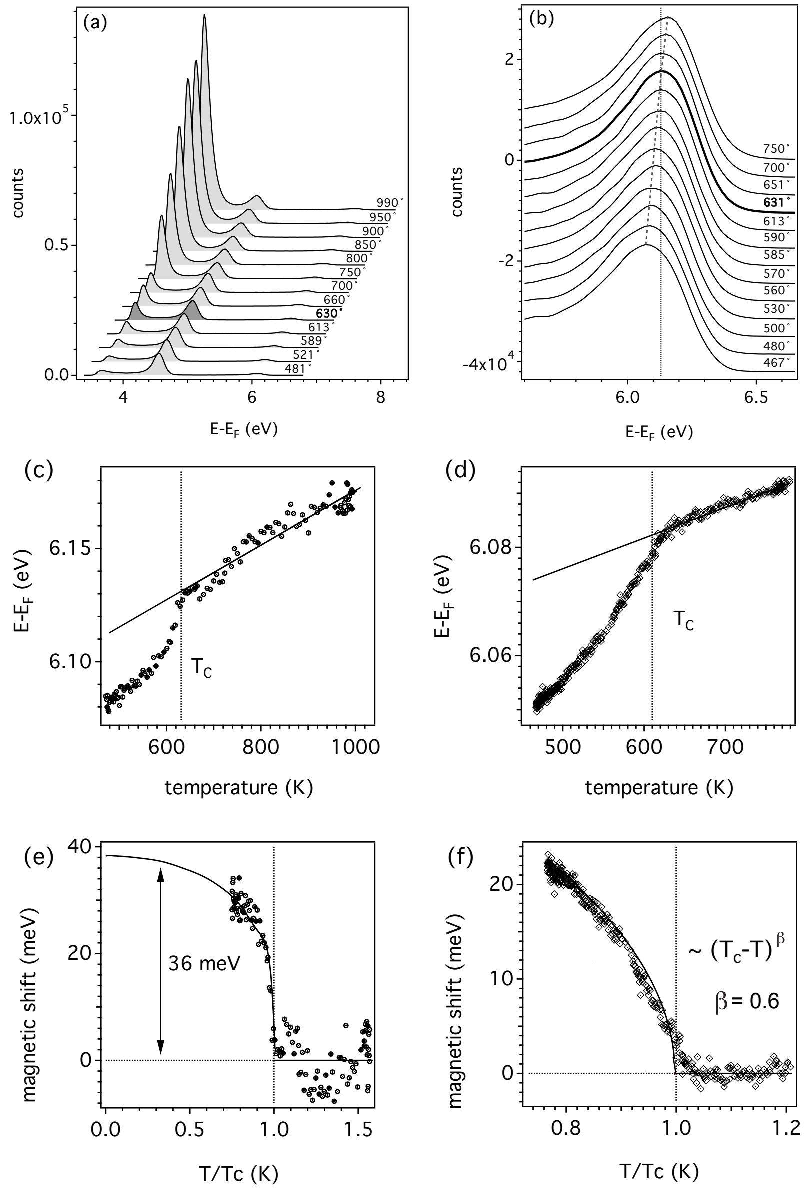

Figure 37: (a) Bichromatic red-blue 2PPE spectra, taken from a *h*-BN monolayer on a Ni(111) single crystal, for different surface temperatures across the ferromagnetic phase transition at $T_c = 631$ K. Note the strong increase of the secondary cut off with increasing sample surface temperatures up to 1000 K. This behavior has been identified as a contribution from one-photon photoemission out of the thermally excited Fermi tail of the Ni surface, by absorption of one photon with an energy of 3.1 eV [49]. (b) Blue-blue spectra zoomed on the IPS peak of a *h*-BN/Ni(111)-film as function of surface temperature. Fitted final state position of the IPS transition recorded from the Ni-crystal (c) and from the 80 nm thick Ni-film (d) with respect to the Fermi level as function of the sample temperature. (e) and (f) "Magnetic shift", obtained by subtracting the measured positions from the extrapolated values of the linear thermal shift above T_c. Note the normalized temperature scale T/T_c. A bulk magnetization curve of nickel was fitted to the data in (e) and a power law $(T_c - T)^\beta$ in (f).

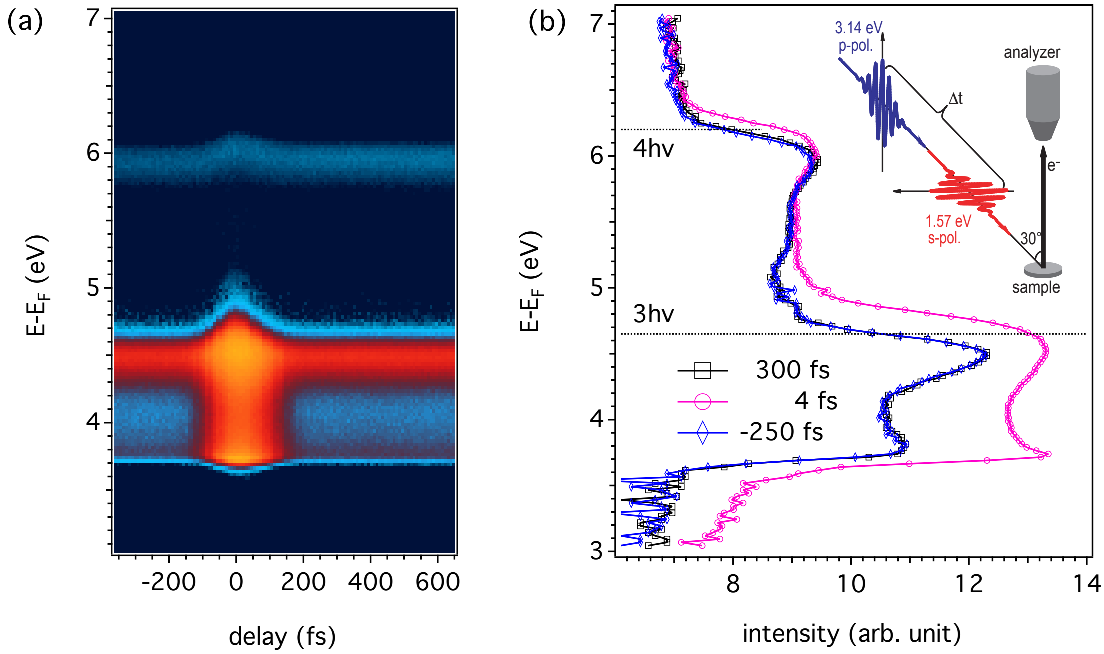

Figure 38: Time-resolved 2PPE data from h-BN/80 nm Ni(111)/Al$_2$O$_3$. (a) False-colour plot of the 2PPE intensity as function of energy (vertical axis) and delay time (in the range between -400 fs and +600 fs) with respect to a pump pulse at zero delay. (b) Three selected spectra were logarithmically plotted corresponding to constant delay cuts at -250 fs, 4 fs and +300 fs delay time. Inset: Schematic drawing of the experimental setup using s-polarized pump and p-polarized probe pulses incident under 30° on the sample. The photoelectrons were detected in normal emission.

4.6.5 Time-resolved 2PPE

Time-resolved 2PPE was applied in order to study optically induced ultrafast demagnetization processes on h-BN/Ni(111). The electrons were excited by an intense pump pulse (fundamental; 800 nm; s-polarized) and after a fixed time delay their transient spectrum was probed by a 2PPE process (frequency doubled probe pulse; 400 nm; p-polarized). In Fig. 38 a series of 2PPE spectra from the h-BN/Ni(111)-film sample is shown, which was recorded for various time delays between -400 and +600 fs. The time scale was chosen such that for positive (negative) time delays the probe pulse follows (preceedes) the pump pulse. The measured bichromatic spectra in Fig. 38 (b) differ from the monochromatic (3.1 eV) 2PPE spectrum of the Ni(111) film in Fig. 36 (a). A significant but delay independent multi-photon photoemission background due to the fundamental (1.5 eV) pump pulse as exemplified by the appearance of the 3PPE peak from the fundamental pulse at 4.5 eV was observed. The strong resonance involving the IPS, which was previously observed in bichromatic 2PPE spectra [46], is strongly suppressed because of dipole selection rules (s-polarization of the pump pulse). In the time-resolved spectra shown in Fig. 38 the IPS appears

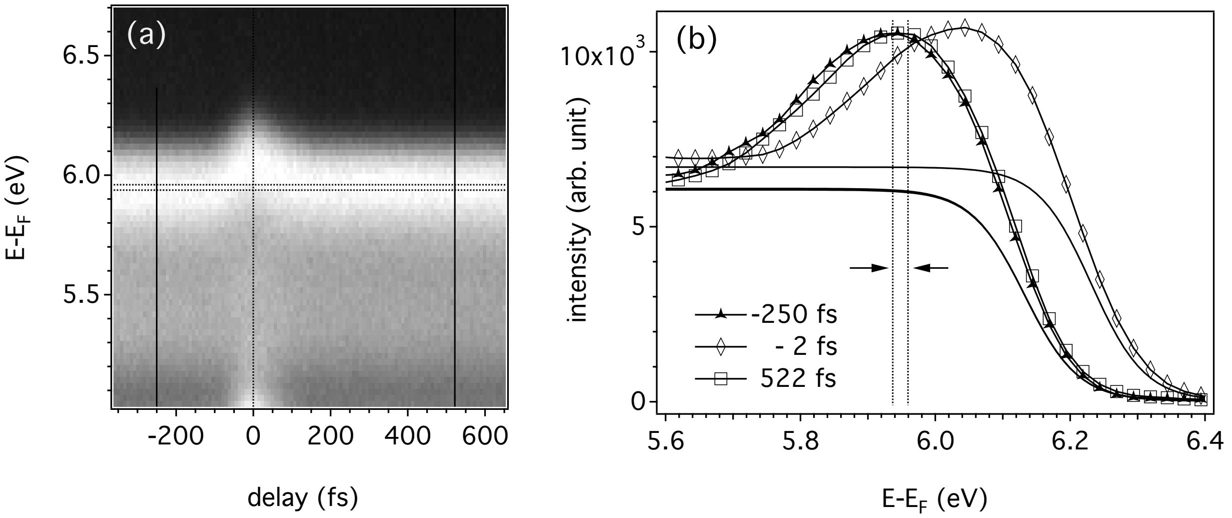

Figure 39: (a) Zoom of Fig. 38 (a): Plot of the transient IPS photoelectron intensity versus time delay. (b) Three depicted photoelectron spectra for -250 fs (*solid triangles*), in coincidence (*empty squares*) and for a positive time delay of 300 fs, with the corresponding fitted direct 2PPE Fermi edge (*solid line*) at $4h\nu$.

at about 5.95 eV for negative time delays. Around coincidence (from -100 to +100 fs) strong broadening and a shift of about 100 meV towards higher energies occur. In this time window, the 2PPE spectra are dominated by the dynamics of the hot electron distribution inside the solid state surface and the presence of mutual Coulomb repulsions between the photoelectrons after the emission into vacuum (as already shown in Fig. 32 (a) in Sec. 4.5.3).

In order to get further insight into the hot electron dynamics the excitation density caused by the intense pump pulse was calculated. At a number of $5 \cdot 10^{12}$ photons per pump pulse impinging within an area of $8 \cdot 10^{-9}\text{m}^2$, probing a sample volume of 10^{13} atoms, and using a photoexcitation cross section for Ni 3d-electrons as extrapolated from the Yeh-Lindau tables [111] to low photon energies ($\sigma_{3d}^{f}(1.55\text{eV}) \approx 0.3$ Mb $= 3 \cdot 10^{-23}\text{m}^2$), an excitation density of 0.02 electrons per pulse and atom was estimated. Within a factor of 2-3 this value is in agreement with the excitation density of 0.05 electrons per pulse and atom calculated via the optical constants of nickel. [16]

Thus the pump pulse creates a transient non-equilibrium electron distribution above the Fermi level E_F which appears in the 2PPE spectra above 6.2 eV (blue-blue Fermi edge) and 4.65 eV (red-blue Fermi edge), shown in Fig. 38. The numeric solution of the rate-equation of the excited population using a crosscorrelation width of 119 fs yields an energy dissipation timescale of 32 fs (electron-electron scattering, in agreement with [112,113]). The electronic excess energy $\varepsilon_e(t)$ per

---

[16] For the calculations the following optical constants have been used: reflectivities at 30° incidence for 400 nm 0.74 (s-polarized) and 0.66 (p-polarized), for 800 nm 0.85 (s-polarized) and 0.81 (p-polarized), an absorption volume which corresponds to a cylinder with a waist of 100 μm and a penetration depth of 140 Å (for 800 nm), refractive indices for nickel are 2.49 (800 nm) and 1.6 (400 nm) and absorption coefficients (imaginary parts of the refractive indices) for nickel are 4.45 (800 nm) and 2.4 (400 nm) [82].

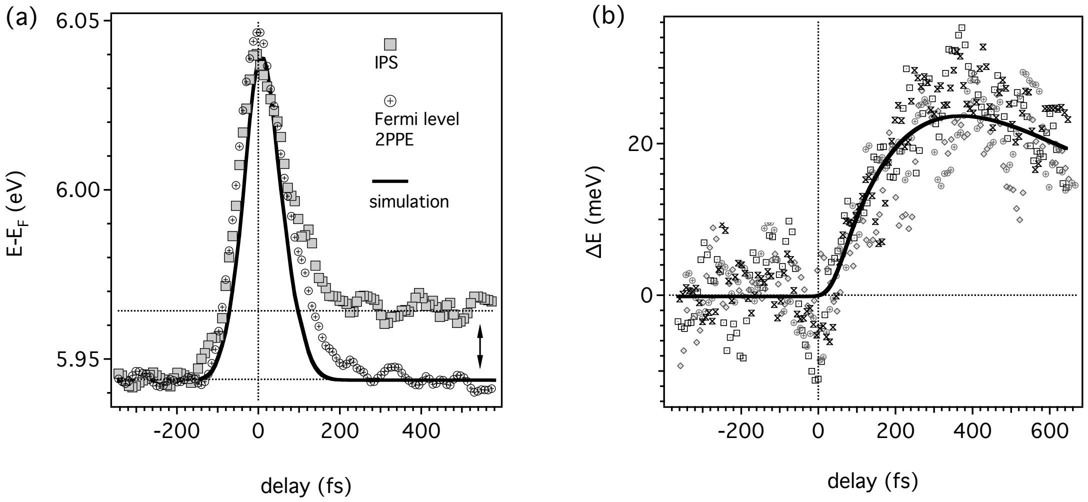

Figure 40: (a) Measured peak position of the IPS (*open squares*), the underlying direct 2PPE Fermi edge position (*open circles* plotted with an offset of -250 meV for comparison) and resulting IPS peak position from the space-charge simulation (according to Ref. [38], *solid line*) vs. delay time for the 80 nm thick Ni(111) film. (b) Magnetic shift of the IPS vs. delay time (*markers*) and corresponding double exponential fit (*solid line*).

excited sample volume (10^{-16}m^3) is given by $C_e \cdot T_e$. Using an average heat capacity for the electronic system of $C_e = \gamma \cdot T_e$ [11] and an effective $\gamma = 4500$ Jm^{-3}K^{-2} (extracted for a temperature range between 300 and 1000 K from [114]) the absolute electronic heat capacity of the excited volume can be estimated by linear interpolation to be $C_{e,V}$(300 K) = 135 pJ K^{-1} and $C_{e,V}$(631 K) = 285 pJ K^{-1}. This allows the transient electronic temperature in coincidence $T_e(t = 0$ fs) to be calculated: T_e reaches a value of 705 K and thereby clearly exceeds the Curie temperature in coincidence.

The spectral region around 6.2 eV (in Fig. 39) was fitted by a single Gaussian for the IPS peak and a Fermi distribution belonging to a direct blue-blue transition, as shown in Fig. 39. For the 80 nm film sample the resulting transient IPS peak positions are presented in Fig. 40 (a). The strong shift in the order of 100 meV at zero time delay is caused by space-charge effects during the drift of the photoelectrons in the vacuum. According to the propagation dynamics of a femtosecond electron packet [36,38], the highest (lowest) energy features in the 2PPE spectrum shift towards higher (lower) kinetic energies due to repulsive space charge effects at temporal coincidence between both pulses, when the total photoelectron yield rises strongly.

The space charge simulations have been applied as described in detail in Ref. [38] and Sec. 4.5.3 to the measured transient spectral distributions in Fig. 38. The resulting IPS peak position is computed as function of time delay for a maximal number of 530 photoelectrons per pulse at zero delay as deduced from a measured sample current of 22 pA and into an emission cone of 10°, plotted in Fig. 40 (a). The calculated space-charge distortion of the IPS peak position solely occurs for delays between -100 fs and +200 fs and vanishes for delays longer than +200 fs. Both the transient Fermi edge position as well as the IPS position are reproduced by space-charge induced shifts in a time frame between -100 fs and +50 fs. While the space-charge model catches the main physics in the time range of the pulse overlap, the IPS peak position reveals a slight but significant difference in energy of about 25 meV for delays larger than 200 fs compared to delays smaller than -200 fs (compare the spectra in Fig. 39 b and fitted IPS positions in Fig. 40 a). A contribution to this peak shift due to charging of the sample by the large photoelectron release caused by the incident pump pulse can be excluded since the secondary electron cut off stays precisely at the same energy for delays larger than 200 fs as for delays smaller than -200 fs. Since the transient Fermi edge position is solely influenced by space-charge effects over the whole measured time range one can obtain a space-charge independent shift of the IPS by subtracting the transient Fermi edge position as function of time delay, shown in Fig. 40 (b). The resulting curve can be fitted by a double exponential function $E(t) = \Delta E(1 - exp(-t/\tau_1)) \cdot exp(-t/\tau_2)$ with the corresponding time constants found to be $\tau_1 = 310$ fs and $\tau_2 = 820$ fs and a magnetic shift of $\Delta E = 32$ meV.

One might relate this space charge independent shift towards higher energies in Fig. 40 (b) to a magnetic shift of the $n = 1$ IPS on a time scale of $\tau_1 = 310$ fs and thus as an evidence for a laser pulse induced reduction of magnetization in h-BN/Ni(111). Rhie *et al.* [12] observed a collapse of the magnetic exchange splitting of the Ni-3d bands in thin films, following a femtosecond laser pulse with a time constant of 300 ± 70 fs. Since the spin splitting of an IPS is primarily a consequence of the exchange processes in the 3d-bands of the Ni substrate [115], the present observation confirms the expected dynamical behavior.

Beaurepaire et al. introduced a phenomenological three-temperature model [11] describing the magnetization by a spin temperature T_s, which equilibrates via energy exchange with the electron (T_{el}) and phonon baths (T_L). The general understanding of an ultrafast demagnetization process is that after a femtosecond optical pulse the induced nascent nonequilibrium electron gas thermalizes to a Fermi distribution by electron-electron-scattering within a few 100 fs, followed by a subsequent energy transfer to the lattice due to electron-phonon interactions (within 0.1-10 ps). An Elliot-Yaffet type spin-orbit induced spin-flip mechanism [116] in electron-phonon scattering events (as schematically illustrated in Fig. 41) was shown to explain the ultrafast demagnetization dynamics in model calculations [14, 117] and was experimentally observed in thin cobalt [13] and thin Ni films [14, 118] on a time scale faster than conventional electron-phonon energy transfer. Fig. 42 shows the calculated transient evolution of T_{el}, T_s and T_L by Koopmans *et al.* for electron-phonon scattering processes accompanied by three different spin-flip probabilities. The lattice acts in this case as a sink for the angular momentum transferred from the electronic system and allows for angular momentum conservation during the demagnetization process. This is corroborated by XMCD measurements on a 15 nm thick Ni-film by Stamm *et al.* [15] excluding the rapid transfer between spin and orbital momentum to be a relevant dissipation pathway for angular momentum transfer away from the spin subsystem. The disorder of the spin system can be described by a phenomenological spin temperature T_s. In the present case the spin temperature reaches a value of $T_s = 550$ K at 400 fs as inferred from the magnetic shift of 25 meV and the calibration curve

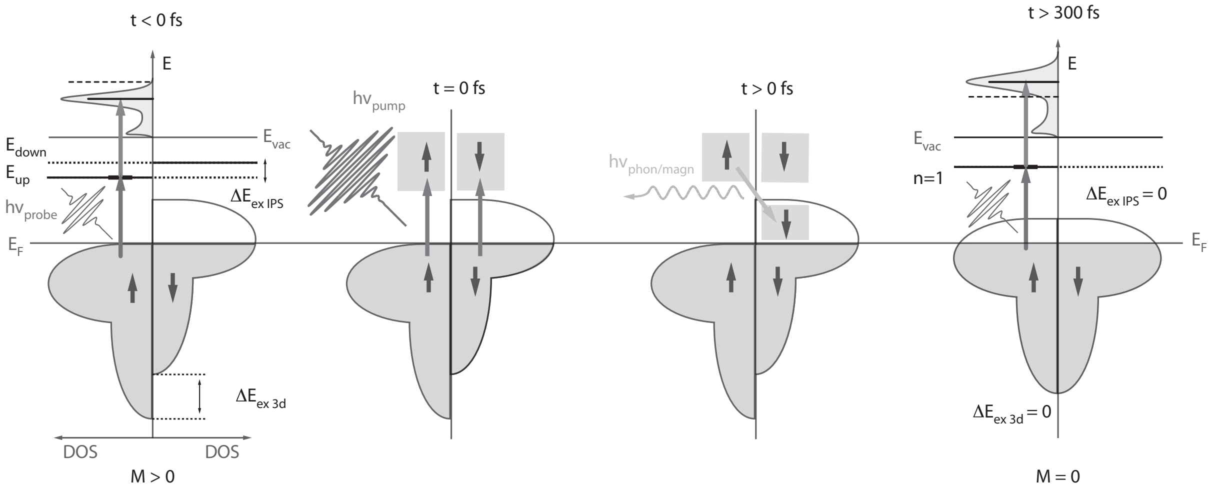

Figure 41: Schematic drawing of a possible ultrafast demagnetization process in an itinerant band ferromagnet like Ni. $t < 0$ fs: The ferromagnetic state of Ni below the critical temperature T_c is represented by the exchange splitting $\Delta E_{ex\ 3d}$ between the occupied Ni $3d$ majority-band ($\uparrow$) and minority-band ($\downarrow$), inducing an exchange splitting $\Delta E_{ex\ IPS}$ in the unoccupied $n = 1$ image potential state. At $t = 0$ fs: the absorption of an intense infrared laser pulse creates a transient hot electron population above the Fermi level. The excited electronic system relaxes through thermalization by means of electron-electron scattering within the first 100 fs, followed by subsequent spin-flip processes, predominantly from spin-up ($\uparrow$) to spin-down ($\downarrow$) electrons due to the larger unoccupied DOS for minority electrons ($\downarrow$) around E_F. After 300 fs the transient paramagnetic phase is reflected by the vanished exchange splitting of the $3d$-bands. The according collapse of the IPS exchange splitting $\Delta E_{ex\ IPS}$ causes a spectral shift of the 2PPE transition via the majority part of the IPS away from E_F in the order of 20 meV, estimated from temperature dependent measurements.

in Fig. 37 (f). The electronic temperature T_e exceeds the Curie temperature of the film sample in coincidence (705 K) and thus fulfills the requirements for ultrafast demagnetization.
This interpretation is further corroborated by the lack of a transient magnetic shift in the case of the single-crystal Ni(111) sample for the same experimental conditions (Ref. [38] and Fig. 32 (e)). An interpretation for that could be the hot carrier diffusion in the direction normal to the surface and into the bulk. These processes remove a significant part of the energy deposited in the sampled volume within the first 100 fs. This is in contrast to the case of the film sample where hot electron transport is suppressed due to the small sample thickness and the insulating character of the underlying substrate [28, 119]. Transverse heat loss through ballistic electron propagation in the direction parallel to the surface is in both cases negligible on the femtosecond time scale, given the beam spot diameter is ~100 μm [11].

Conclusion: In conclusion the $n = 1$ majority IPS can be used as probe for the ferromagnetic order in a h-BN/80 nm Ni(111)-film sample. Static temperature-dependent measurements reveal

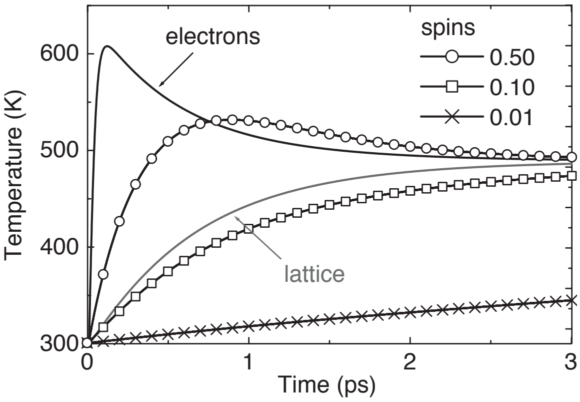

Figure 42: Simulated evolution of electron (T_{el}), lattice (T_L) and spin temperature (T_s) after complete infrared laser pulse irradiation at t = 100 fs, for three different spin-flip probability values α as indicated. T_{el} and T_L are only displayed for $\alpha = 0.5$. Graph from Ref. [14].

its sensitivity to the ferromagnetic phase transition, with the peak shift following the surface magnetization curve of nickel. Dynamic measurements give evidence for a collapse of the substrate induced exchange splitting on a time scale of 300 fs after the impact of an intense infrared laser pulse, thus monitoring the quenching of the Ni magnetic moment on a ultrafast time scale. This result is corroborated by the analysis of the transient excess energy in the electronic system.

5 Bi(114)

5.1 The quasi one-dimensional Bi(114) surface: an introduction

5.1.1 Geometric structure

A convenient way to obtain the truncated bulk structure of the (1×1) unreconstructed vicinal Bi(114) surface is rotating the bismuth crystal 15.2° around the $(1\bar{1}0)$ axis away from the (001) direction toward (111). The resulting model is shown in Fig. 43 (a). The dashed lines indicate the (1×1) unit cell in real space with a size of 4.55 Å × 14.18 Å [16]. Characteristic straight atomic rows terminate the surface along the $(1\bar{1}0)$ direction, at the edge of the vicinal terraces. As a matter of fact the mirror plane in the y-direction perpendicular to atomic lines is the only symmetry element of the surface. The mirror plane in y-direction is also represented by the one-dimensional vertical line through the center of the X-ray photoelectron diffraction (XPD) pattern in Fig. 44. It is the only symmetry plane visible in the two-dimensional XPD pattern, which was measured at the kinetic energy of the Bi $4f_{3/2}$ core levels. Stereographically projected diffraction spots on this line correspond to the (111), (112), (114), (001) and the $(\bar{1}\bar{1}2)$ scattering directions, all lying in the mirror plane, respectively.
Comparison of the structure model to the low temperature STM images with atomic resolution by the group of J. I. Pascual (Fig. 45 b and c) indicate a larger corrugation along y, perpendicular to the rows. Wells *et al.* found that the structure can best be fitted to the data by simply removing the 4 highest lying atoms from a doubled (1×2) unit cell (Fig. 43 b). Two remaining protruding atomic rows along the x-direction then strongly enhance the one-dimensional character of the surface. The 4.55 Å × 28.4 Å large unit cell, between two of the topmost atomic rows, is marked in the STM picture in Fig. 43 (c) as pink dashed square.

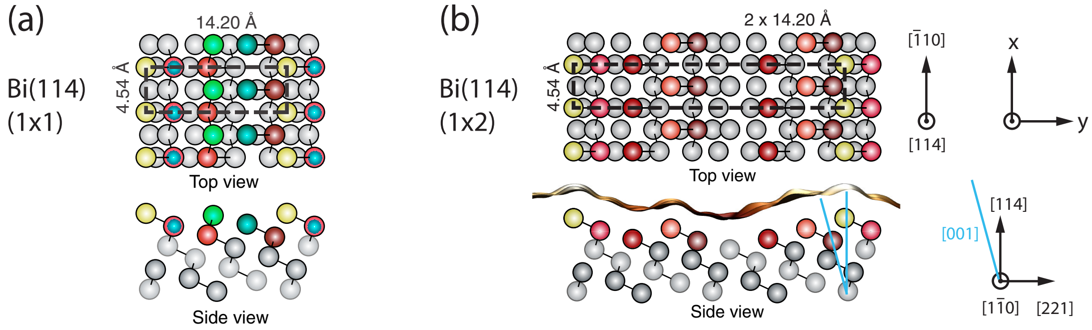

Figure 43: (a) Truncated bulk structure of the Bi(114) surface and the corresponding (1×1) unit cell, marked as *dashed line*. Thin *solid lines* between the bismuth atoms indicate the pseudo covalent bonds of the bismuth double layer structure. The x-direction parallel the atomic rows along $(1\bar{1}0)$ corresponds to $\bar{\Gamma}$-$\bar{X}$, and the y-direction along (221) to $\bar{\Gamma}$-$\bar{Y}$, respectively. (b) Atomic model of the (1×2) surface reconstruction. Taken from Ref. [16].

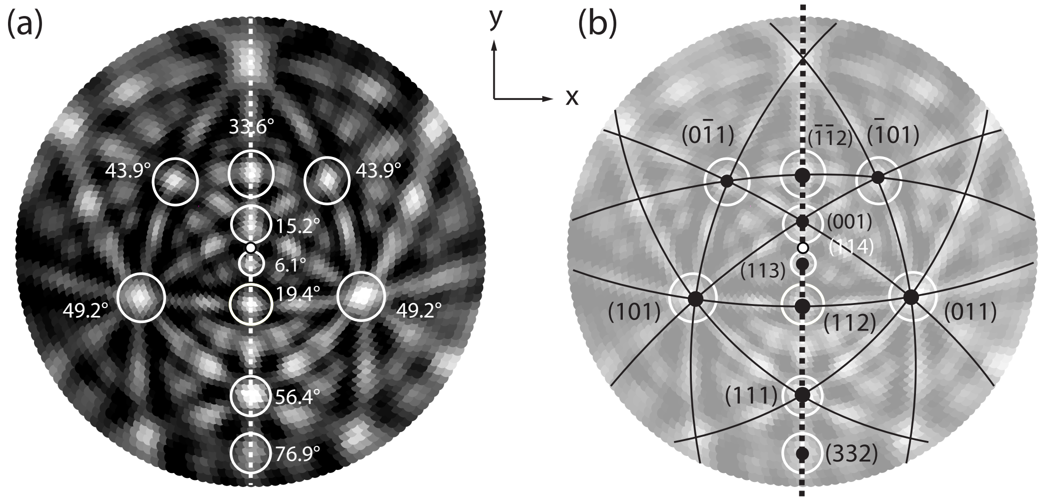

Figure 44: X-ray photoelectron diffraction pattern (XPD) of the Bi(114) surface, measured at the VG ESCALAB [23] at the kinetic energy of the Bi $4f_{3/2}$ core level. *Vertical dashed line* denotes the projection of the only symmetry plane of the Bi(114) surface, along the y-direction and perpendicular to the characteristic one-dimensional atomic rows.

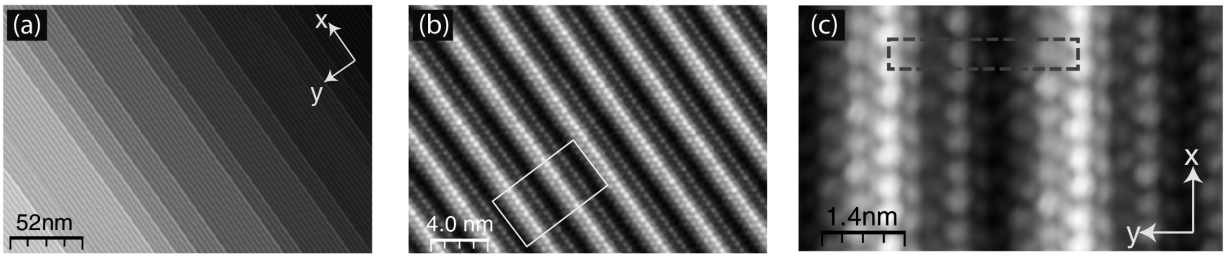

Figure 45: (a-c) STM images of the Bi(114) surface, for different sample biases close to E_F. (c) is an atomically resolved and zoomed image corresponding to the *rectangular area* marked in (b), containing the (1×2) unit cell (*dashed line*). Straight atomic rows are running parallel to the x-direction, perpendicular to the only high symmetry plane of the surface. The STM results are not discussed in this work. Taken from Ref. [16].

5.1.2 Electronic structure

Beside the geometric characteristics, the one-dimensional character of the Bi(114) surface is also strongly reflected in its electronic structure. The Fermi surface map (FSM) in Fig. 46, taken at the VG ESCALAB 220 [23] at $h\nu = 21.21$ eV, reveals straight lines along $\overline{\Gamma}$-$\overline{Y}$ as the dominating feature. The Fermi line passes through the center $\overline{\Gamma}$ of the first SBZ. Corresponding lines can be found in the second SBZ at $k_x = 1.4 \pm 0.03$ Å^{-1} and -1.4 ± 0.03 Å^{-1}, respectively. According to photoemission measurements for variable UV-photon energies [16] at the SGM-3 beamline of the storage ring ASTRID [120] the intensity and k-position of the one-dimensional FSM contour does not depend on the probing photon energy. This suggests a missing dispersion of these states along $k_\perp$ in the [114]-direction and thus a surface-localized character [16]. From the straight line along $\overline{\Gamma}$-$\overline{Y}$ one can conclude a purely one-dimensional dispersive delocalization of the surface state along $\overline{\Gamma}$-$\overline{X}$, parallel to the straight atomic lines of the surface.

Since the broad features with weak intensity in Fig. 46 have not exactly been reproduced for other UV-wavelengths from the synchrotron and do not follow the periodicity of the SBZ they are attributed to bismuth bulk bands in the vicinity of E_F.

Bulk bismuth is known to be a 'traditional' semimetal with a low density of states (DOS) at the Fermi level E_F. For the Bi(110) and the Bi(111) surfaces metallic surface states have already been found in the projected truncated bulk band gap, crossing the Fermi level E_F and therefore turning the surface into a better metal than the bulk [121]. Furthermore spin-resolved ARPES measurements from the COPHEE end station [35, 122] at the surface and interface spectroscopy (SIS) beam line at the Swiss Light Source (SLS) give a second argument for the *surface localization* of the one-dimensional state. The spin-integrated cut perpendicular to the Fermi line at E_F in Fig. 47 (b) with an FWHM of 0.082 Å^{-1} can be decomposed by means of three-dimensional spin de-

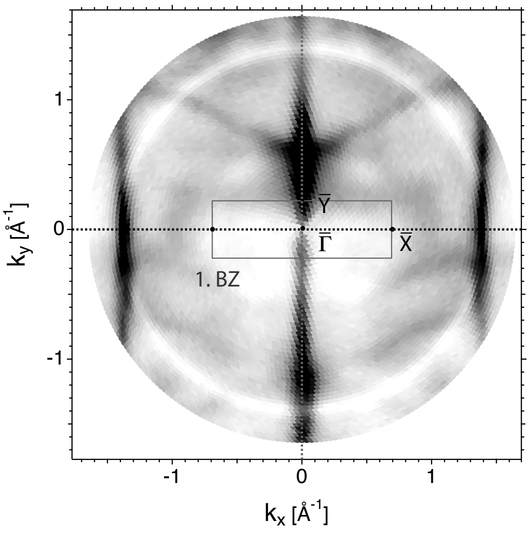

Figure 46: Fermi surface map of Bi(114), measured for $h\nu$ =21.21 eV at the VG ESCALAB [23]. The *solid rectangle* marks the first Brillouin zone.

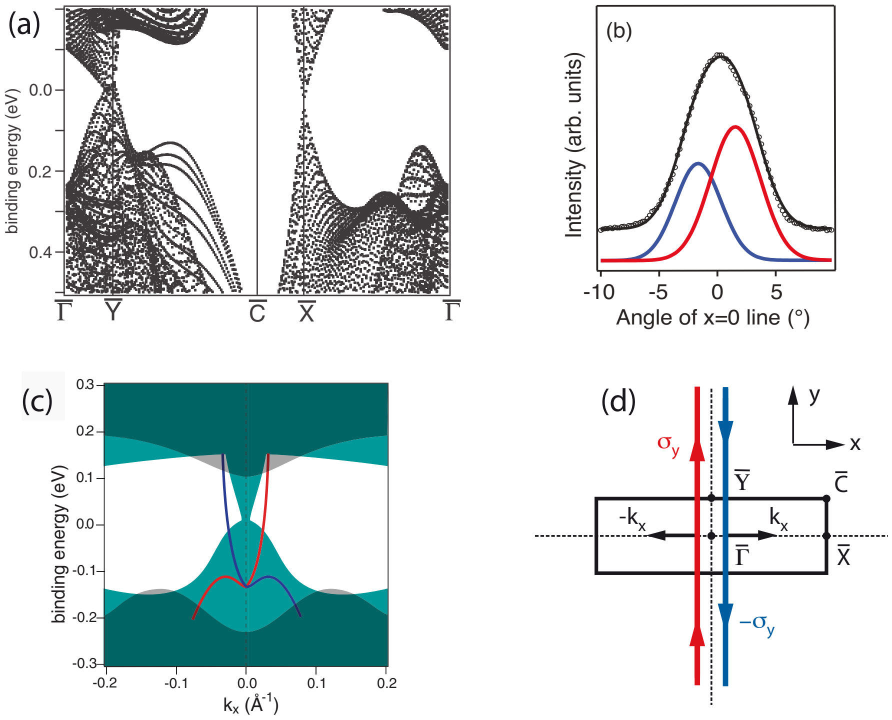

Figure 47: (a) Tight binding calculation of the Bi band structure along several high-symmetry directions in the truncated bulk SBZ. Note the band gap of ≈ 0.3 eV at $\bar{\Gamma}$ and the bulk band crossing of the Fermi level at $\bar{Y}$. (b) Spin-integrated photoemission intensity (*open circles*) of an azimuthal cut through the Fermi surface along the $\bar{\Gamma}$-$\bar{X}$ direction, corresponding to the two different spin states with opposite momentum k_x, separated by 0.067 Å^{-1}, representing the non-degenerate spin-split structure of the 1D surface state along $\bar{\Gamma}$-$\bar{X}$. (c) Qualitative drawing of the surface state dispersion $E(k_x)$ on top of the calculated projected bulk band structure along $\bar{\Gamma}$-$\bar{X}$ (*light grey area*) and along $\bar{Y}$-$\bar{C}$ (*light green area*). (d) Scheme of the Fermi surface contour of Bi(114), with the *red* and *blue* arrows pointing towards the main in-plane spin direction. Taken from Ref. [16].

tection into a subset of two 100 % spin-polarized sub-bands, with maxima separated by 0.067 Å^{-1} from each other. The spin polarization vectors σ_y(-σ_y) are almost pointing (anti)parallel to $\bar{\Gamma}$-$\bar{Y}$ with an out of plane incline of 30° and perpendicular to the electron momenta k_x(-k_x), schematically sketched in Fig. 47 (d).

The Fermi line actually turned out to be a Kramers pair of two one-dimensional fully spin-polarized states, fulfilling time reversal symmetry

$$[H,T] \;=\; HT \;-\; TH \;=\; 0 \tag{38}$$

with the corresponding relation[17] $E(-\mathbf{k_x},\sigma_\mathbf{y}) \;= E(\mathbf{k_x},-\sigma_\mathbf{y})$. Note that the time reversal operator T both changes the momentum $\mathbf{k}$ and flips the spin σ of an electron. In the Rashba model [123]

---

[17] Note that $E(-\mathbf{k_x},\sigma_\mathbf{y}) = E(\mathbf{k_x},-\sigma_\mathbf{y})$ follows from $[H,T] = HT$ - $TH = 0$, given by the characteristics of the time-reversal operator T:

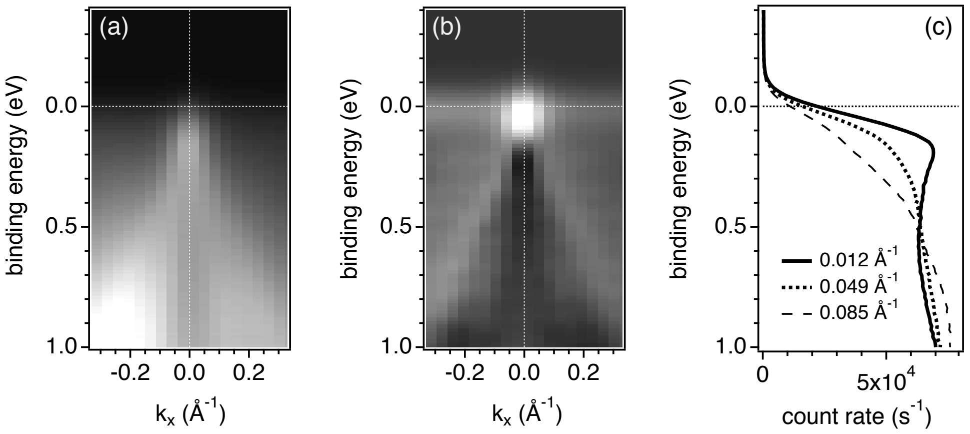

Figure 48: (a) Energy versus electron momentum along $\overline{\Gamma}$-$\overline{X}$ parallel to the atomic rows for $k_y = 0$, revealing the surface state on top of the Λ-shaped dispersing bulk band below, measured with $h\nu = 21.21$ eV in the VG ESCALAB 220 [23]. (b) First derivative with respect to binding energy of the spectra in (a) in order to outline the dispersion. (c) Photoemission spectra at different values of k_x, indicating a binding energy maximum of the 1D surface state at 150 meV.

the spin degeneracy is lifted at the surface due to the structural inversion symmetry breaking of the surface and the strong spin-orbit coupling of the heavy element bismuth (209 au). The corresponding spin-orbit coupling Hamiltonian H_{SOC} is given by

$$H_{SOC} = \frac{-i\hbar^2}{2m_e^2} \cdot (\nabla_{\mathbf{z}} V \times \nabla_{\mathbf{x}}) \cdot \sigma_{\mathbf{y}}, \tag{39}$$

whereas $\nabla_{\mathbf{z}} V$ is the symmetry breaking potential gradient at the surface, $\sigma_{\mathbf{y}}$ the spin vector of the Pauli matrices along $\overline{\Gamma}$-$\overline{Y}$ and $-i\hbar\nabla_{\mathbf{x}}$ the momentum operator of the electrons along $\overline{\Gamma}$-$\overline{X}$. The fact that only one Fermi level crossing (odd number) per spin has been detected in the spin-resolved cut through the whole FSM is actually inconsistent with the common picture of two Rashba parabolas, slightly shifted in k-space with respect to each other. One explanation for the missing even number of Fermi surface crossings could be that the other two bands may disperse towards higher binding energies, loosing their surface-localization in the bulk continuum [16] (Fig. 47 c).

Due to the inversion symmetry in the bulk one would not expect such a spin splitting for bulk states in general. Time reversal symmetry *and* space inversion symmetry ($[H, P] = 0$) are assumed to hold in the bulk. Note that the space inversion operator P just changes the momentum of the electron. Consequently the relation [18] $E(-\mathbf{k}, \sigma) = E(+\mathbf{k}, \sigma)$ would exclude a k-resolved

---

$HT|\psi(k,\uparrow)\rangle = H|\psi(-k,\downarrow)\rangle = E(-k,\downarrow)|\psi(-k,\downarrow)\rangle$
$TH|\psi(k,\uparrow)\rangle = E(k,\uparrow)T|\psi(k,\uparrow)\rangle = E(k,\uparrow)|\psi(-k,\downarrow)\rangle$

[18] Note that $E(\mathbf{k_x}, \sigma_{\mathbf{y}}) = E(\mathbf{k_x}, -\sigma_{\mathbf{y}})$ follows from $[H, PT] = HPT - PTH = 0$, given by the characteristics of the time inversion T and space inversion operator P:
$HPT|\psi(k,\uparrow)\rangle = HP|\psi(-k,\downarrow)\rangle = H|\psi(k,\downarrow)\rangle = E(k,\downarrow)|\psi(k,\downarrow)\rangle$
$PTH|\psi(k,\uparrow)\rangle = E(k,\uparrow)PT|\psi(k,\uparrow)\rangle = E(k,\uparrow)P|\psi(-k,\downarrow)\rangle = E(k,\uparrow)|\psi(k,\downarrow)\rangle$

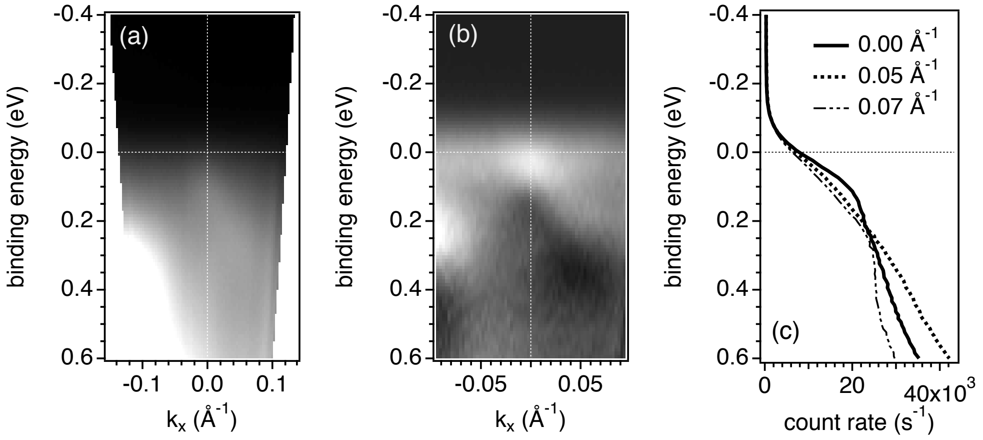

Figure 49: (a) As in Fig. 48, but for 2PPE ($h\nu$ = 2×3.1 eV) involving a virtual intermediate state.

spin splitting for bulk states. However this picture is not fully true since recently a Rashba-type polarization of the photocurrent from bulk states of Bi(111) was reported [124].
Spin-integrated polar cuts of energy versus electron momentum along $\overline{\Gamma}$-$\overline{X}$ for $k_y = 0$ in Fig. 48 and Fig 49 do not resolve the 0.067 Å^{-1} wide splitting of the two spin-polarized states at E_F, as already seen in Fig. 47 of Ref. [16]. Nevertheless both measurements with $h\nu$ = 21.21 eV and with 2×3.1 eV reveal that the two states giving rise to the two parallel Fermi lines are located on top of a Λ-shaped pair of bulk bands. From the spectra at $k_x = k_y = 0$ in Fig. 48 (c) and Fig. 49 (c) one can estimate the binding energy maximum of the surface states at $\overline{\Gamma}$ to be 150 meV. These considerations are consistent with the calculated projected bulk band gap and bulk band structure in Fig. 47. Note that due to the experimental geometry in the polar scans (fixed analyzer and incident light direction but rotating sample) in Fig. 49 the photoemission matrix elements and thus the photoemission intensity of the individual bands strongly depend on the polar angle. The measured asymmetry between positive and negative k_x-values becomes stronger going from higher ($h\nu$ = 21.21 eV in Fig. 48) towards lower photon energies ($h\nu$ = 6.2 eV in Fig. 49) due to the increasing polar angle range in the experiment.

5.1.3 Preparation

Initially the Bi(114) crystal was mechanically and electrochemically polished by Ph. Hofmann (in Aarhus). Before each measurement the surface was cleaned in situ by cycles of argon sputtering and subsequent annealing at 300 K. Despite the fact that Bi(114) is chemically quite inert, possible contamination and surface quality have been checked after each preparation by measuring the Fermi surface of the 1D surface state with $h\nu$ = 21.21 eV, as shown in Fig. 46.

5.2 Circular dichroism revealing the spin-splitting of the one-dimensional surface state

Owing to the strongly one-dimensional electronic character of the Bi(114) surface and the strong spin-orbit coupling in bismuth a 100% spin polarization was found for the surface state [16]. The spin structure follows the electronic one-dimensionality of the surface state in a sense that the spin vectors are orientated perpendicular to $\mathbf{k_x}$. Hence, such a relatively simple spin structure with only one unique spin quantization axis could serve as nice model system for testing alternative spin detection methods.

Circular dichroism in the angular distribution of photoelectrons (CDAD) is an interference effect between symmetric and antisymmetric contributions in the final state of the photoexcitation process [125]. In the non-relativistic case the matrix element for photoexcitation entirely depends on the spatial symmetry properties of the initial and final electronic state in the solid and the helicity of the photon. This general principle can be translated into various dipole selection rules for different crystalline surface and bulk structures and their corresponding electronic band structure. These selection rules are governed by spatial symmetries of the electronic states only. For heavy elements the strong spin-orbit coupling affects the symmetries and introduces an electron spin dependance into the transition matrix elements.

Recently Wang *et al.* mapped the spin helicity of the topological surface state of Bi_2Se_3 by means of an alternative way [126]. The method is based on time-of-flight (TOF) photoelectron detection that is capable of measuring simultaneously spin polarization vectors for different energies E and k-vectors over a large phase-space volume, by using circularly polarized 6 eV laser pulses. The collected three-dimensional TOF-ARPES data $I_R(E, k_x, k_y)$ for right- and $I_L(E, k_x, k_y)$ for left-circularly polarized photons respectively are subsequently subtracted from each other, leading to a difference ΔI. Due to angular momentum selection rules, arising from the electron spin via the spin-orbit interaction, ΔI is sensitive to the spin polarization $\langle S_y \rangle$ and $\langle S_z \rangle$ of the non-degenerate initial state ψ_i^{2D} and on the polarization A_x, A_y and A_z of the incident A-field by [126]

$$\Delta I = I_R - I_L = \alpha \langle S_y \rangle Re(A_x^\star \cdot A_z) + |\beta| \langle S_z \rangle Re(A_y^\star \cdot A_x). \tag{40}$$

Note that in principle the third spin component $\langle S_x \rangle$ directly follows from azimuthal rotation of the sample by 90°. Fig. 51 (c) schematically sketches the corresponding situation for a two-dimensional energy versus momentum cut $E(k)$.

Leading spin-resolved experiments based on Mott scattering are capable to measure the spin polarization vector of one discrete point in energy and momentum space at a time [35,122,127,128]. Furthermore the efficiency of the Mott scattering process reduces the available statistics compared to spin-integrated ARPES measurements with an electrostatic hemispherical analyzer further by three to four orders of magnitude. Once knowing the detailed spin structure from Mott scattering based SARPES, an alternative spin sensitive method, such as circular dichroism based on angular momentum selection rules, combined with a parallel detection scheme, could be well suited for experiments with rather low data acquisition times. The following Sec. 5.2.1 and 5.2.2 will describe the attempt of revealing the one-dimensional spin structure of the Bi(114) surface state by means of this technique.

5.2.1 Experimental realisation

Direct comparison of optical transition probabilities requires a fixed relative orientation between the sample position and the photon polarization (compare discussion about matrix element effects in Sec. 3.1). Hence, a parallel detection scheme for data acquisition at multiple emission angles is required. Especially if one is interested in mapping ΔI over the complete SBZ an elliptical display analyzer (EDA), as introduced in chapter 3, can be the instrument of choice. Despite the restrictions in energy resolution and in the signal-to-noise ratio, as discussed in Sec. 3.4 and 3.6.2, the thin one-dimensional signature in k-space of the surface state 150 meV below E_F [19] is clearly revealed in Fig. 50 by using linearly p-polarized light of $h\nu = 5.95$ eV.
The pass energy E_{pass} of the EDA was set to 9 eV with a corresponding energy resolution of roughly 170 meV (compare Sec. 3.4.1). Already within typical 90 s data acquisition time snapshots at fixed energy and light polarization exhibit very reasonable statistical quality. Since the photon energy of 5.95 eV exceeds the work function $\Phi_{Bi(114)} = 4.32$ eV, the corresponding 1PPE photoemission process is linear. Unlike in a non-linear 2PPE process where the laser beam waist on the sample can be minimized by maximizing the total photoelectron yield (*e.g.* by measuring the corresponding sample current), the 6 eV spot size has to be optimized outside of the UHV chamber. Therefore the beam was picked by means of a flip-mirror between the last lens and the UHV-viewport [20] and steered on a fluorescent screen outside of the vacuum chamber at the same distance as the sample. Such a procedure is imperative since the angular resolution of the EDA and thus the mapping precision in k-space delicately depends on the laser beam waist on the sample as discussed in Sec. 3.5. Optimization leads to an estimated focus diameter of < 500 μm. According to Eq. 24 and Eq. 25 the chosen aperture size of 1.5 mm in the lower focal point of the ellipsoidal mirror governs the upper limit, leading to an estimated angular resolution of ± 1.8°.

5.2.2 Results

Fermi surface maps have been taken for both circular right- and circular left-polarized pulses, respectively, as well as for linear p-polarized light, for always exactly the same exposition time. The asymmetry ΔI has been obtained by post-processing the measured snap shots according to

$$\Delta I \; = \; \frac{I_R - I_L}{I_p}. \tag{41}$$

Dividing the difference I_R-I_L by the photoelectron intensity distribution for linear p-polarized light allows to correct for the inhomogeneous detector acceptance over all detected solid angles,

---

[19] The crossing point of the two spin-split surface bands lies 150 meV below E_F.

[20] A special strontium fluoride (SrF_2) viewport is transparent to light in the photon energy range from 8.3 eV to 0.1 eV.

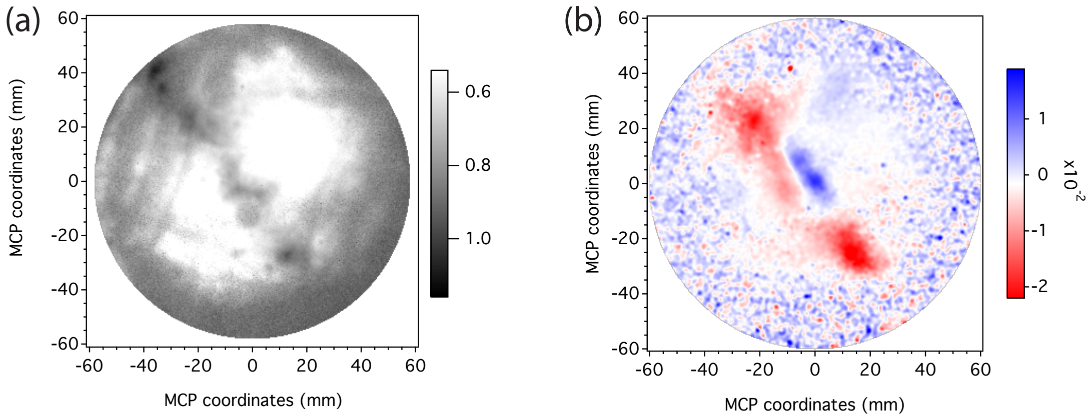

Figure 50: (a) Constant energy snap shot at $E_{binding} = 0.150$ eV, at the maximum of the Bi(114) surface state, for linearly *p*-polarized 6 eV pulses. The data were collected with an exposure time of 90 seconds and a pass energy of 9 eV. The intensity distribution has been corrected for detector inhomogeneities over all solid angles according to Eq. 13. (b) Asymmetry ΔI according to Eq. 41, revealing the spin-splitting of the Bi(114) surface state in the center of the image at $E_{binding} = 0.0$ eV by means of spin dependent circular dichroism.

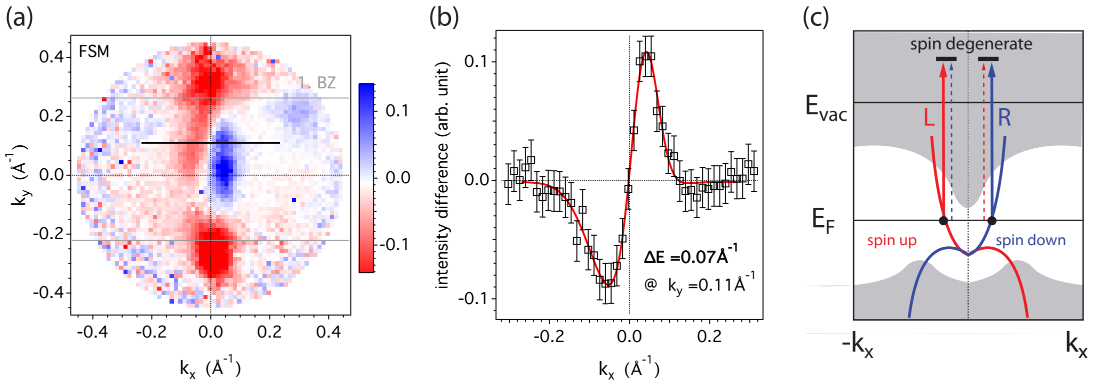

Figure 51: (a) Dichroic signal $\Delta I(k_x, k_y)$ between the Fermi surface map (FSM) recorded with circularly right- and left-polarized 6 eV pulses. Borders of the truncated (1×1) SBZ (*grey lines*) are marked for the sake of clarity. (b) Cut through the SBZ (*rectangular markers*) along $\overline{\Gamma}$-$\overline{X}$ for $k_y = 0.11$ Å^{-1} fitted by a double Gaussian (*red solid line*). (c) Schematically depicted optical transitions from the spin-polarized surface state (*red* and *blue lines*; ψ_i) from the Fermi energy E_F to an unoccupied spin-degenerate bulk bands (*shaded grey region*; ψ_f) above the vacuum level E_{vac}. *Thick* and *thin* vertical arrows represent strong and weak transitions respectively depending on the circular polarization of the pulses, according to the angular momentum selection rules in Eq. 40.

in analogy to the standard procedure in Eq. 13. The resulting image is mapped in Fig. 50 (b). Note that no additional background subtraction has been performed on the data in Fig. 50 and in Fig. 51. However, the only visible feature at E_F is a line passing through the center of the detector. This line is split into two parallel running lines at the center of the spherical imaging. Using Eq. 14 and 15 the projection $\Delta I(x, y)$ can be transformed into $I(k_x, k_y)$ as shown in Fig. 51 (a). The two parallel lines with opposite asymmetry run in parallel over more than 0.2 Å^{-1} from the center of the (1×1) SBZ around $\overline{\Gamma}$ towards $\overline{Y}$. A double Gaussian fit has been applied to the horizontal cut along the $\overline{\Gamma}$-$\overline{X}$ direction at $k_y = 0.11$ Å^{-1}. The results are plotted in Fig. 51 (b). The Gaussian with negative intensity at -0.034(3) Å^{-1} and the opposite Gaussian with positive intensity at 0.036(2) Å^{-1} lead to a total splitting of 0.07 Å^{-1}. This value is in agreement with the value of 0.067 Å^{-1} obtained in spin-resolved ARPES experiments [16]. Therefore the two lines can be identified as the two spin split bands of the Bi(114) surface state. Furthermore the fact that the splitting vanishes at the borders of the SBZ at $\overline{Y}$ and $\overline{Y}'$ coincides with the Fermi surface of the spin degenerated projected bulk band. Projected bulk band contributions to the Fermi surface of Bi(114) appear only in the vicinity of the $\overline{Y}$ point. Indeed the Fermi level crossing of bulk bands at $\overline{Y}$ and $\overline{Y}'$ in the tight binding calculations (Fig. 47) match the region where the splitting gets lost in the measured ΔI in Fig. 51.

Conclusion: In summary, the spin-splitting of the one-dimensional surface state at E_F as shown in Fig. 50 (b), characterized in previous Mott-scattering experiments [16], was revealed in a circular dichroism experiment, based on angular momentum selection rules arising from the electron spin via spin-orbit interaction. The two characteristic oppositely polarized surface state bands, crossing the Fermi level in two parallel lines, appear in the asymmetry of the FSM taken with circularly left-hand and right-hand polarized 6 eV pulses.

The instrument of choice for these spin-investigations was the elliptical display analyzer (EDA), described in detail in chapter 3. Such a parallel detection scheme is necessary to avoid matrix element effects whose intensity modulations would strongly affect the differences arising from circular dichroism.

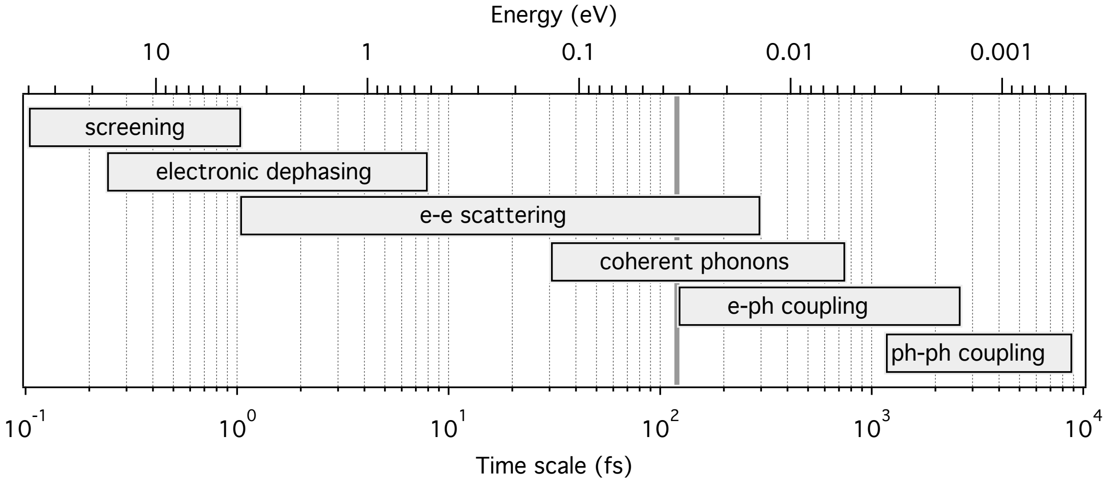

Figure 52: Various dynamical processes at metallic surfaces with their typical timescales (bottom axis) and energy scales (top axis) [22, 129]. The vertical *grey line* indicates the temporal pump pulse width in the present experiment.

5.3 Hot electron dynamics at the Bi(114) surface

5.3.1 Dynamical processes in solid state metal surfaces: an overview

The goal of this section is to monitor the coherent response of the electronic system of Bi(114) upon absorption of an intense femtosecond infrared laser pulse. Initially the energy of the absorbed infrared pulse is transferred into the excitation of a transient electron-hole population. Several decay processes limit the finite lifetime of the initial electron-hole population. According to their timescales they are listed in Fig. 52, from the fastest to slowest processes as the following:

- electron-electron screening
- electron-hole dephasing
- electron-electron scattering
- electron-phonon coupling
- phonon-phonon interaction.

Electron-electron scattering Inelastic electron-electron scattering is the dominant process for reestablishing a thermodynamic equilibrium within the electronic population within the first 100 fs, after infrared laser pulse irradiation [113]. The results of the Landau theory of Fermi liquids describe inelastic electron-electron scattering processes. A hot electron $\mathbf{k}_1$ and a cold electron $\mathbf{k}_2$ in the Fermi sea exchange energy and momentum $\mathbf{q} = \mathbf{k}'_1\text{-}\mathbf{k}_1$ due to the screened Coulomb interaction W, leading to two quasi-particles with final momenta $\mathbf{k}'_1$ and $\mathbf{k}'_2$ and a remaining quasi-hole with

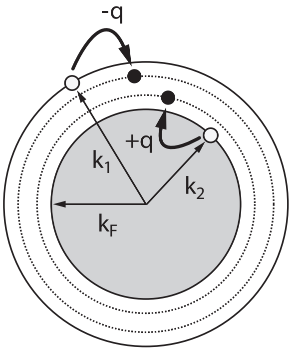

Figure 53: Scheme of an inelastic electron-electron scattering process between a hot electron $\mathbf{k}_1$ and an electron $\mathbf{k}_2$ from the Fermi sea into the quasi-particle states $\mathbf{k}'_1$ and $\mathbf{k}'_2$ by exchanging the momentum q. The radius of the *grey sphere* corresponds to the length of Fermi vector $|k_F|$. According to Fermi-liquid theory the appropriate total scattering rate Γ_{ee}, for an electron with momentum k_1 and spin σ is given by Eq. 42.

$\mathbf{k}_2$. Formally the scattering rate Γ_{ee} written in Fermis Golden rule is given by [130]

$$\Gamma_{ee}(k_1,\sigma_1) \;=\; 2\pi \sum_{k_2,q}\sum_{\sigma_2} W^2(\mathbf{q})\; n_{k_2,\sigma_2}\left[1-n_{k'_2,\sigma_2}\right]\left[1-n_{k'_1,\sigma_1}\right]\delta(\mathbf{k}_{1,\sigma_1}-\mathbf{k}'_{1,\sigma_1}+\mathbf{k}_{2,\sigma_2}-\mathbf{k}'_{2,\sigma_2}), \tag{42}$$

whereas the δ-function assures energy and momentum conservation in the summation over all possible wave vectors k with population occupation number n_k and spin states [21] σ.
The matrix element is determined by the squared Coulomb interaction W^2 as function of momentum exchange $\mathbf{q}$, according to the second order pertubation approach. In the Thomas-Fermi approximation $W(q)$ only depends on q and the Thomas-Fermi screening vector k_s. Together with the density of states of a 3D electron gas the results of Quinn and Ferrel [131] assuming low temperature $k_BT \ll E-E_F \ll E_F$ lead then to the scaling law [132]

$$\tau_{ee}^{(3D)} \;=\; \frac{\pi(4\pi\epsilon_0)^2\hbar^7 k_F k_s^3}{\sqrt{2}m_e^3e^4}\cdot(E-E_F)^{-2} \;=\; a^{(3D)}\cdot n^{5/6}\cdot(E-E_F)^{-2} \;=\; \tau_0\cdot(E-E_F)^{-2}\;, \tag{43}$$

with

$$\tau_0 \;=\; a^{(3D)}\;\cdot\; n^{5/6} \qquad \textit{and} \qquad a^{(3D)} \;=\; \frac{32\;3^{5/6}\;\pi^{2/3}\;\epsilon_0^{1/2}\;\hbar^4}{e\;m_e^{3/2}}. \tag{44}$$

For the TR-PE experiments in this work the bulk electron density in Bi $n_{Bi} = 5.297\cdot 10^{22}$ cm^{-3} is assumed to be constant and hence Eq. 43 reduces to $\tau_{ee} = \tau_0\cdot(E-E_F)^{-2}$ with $\tau_0 = 43.15$ fs and (E-E_F) given in electron-volt. Intuitively speaking, the available scattering phase space of the excited electrons above E_F is reduced upon approaching the Fermi level. Hence the according scattering times τ_{ee} and the associated lifetimes of the electrons increase drastically in proximity of E_F.

---

[21] Note that Eq. 42 does not include spin-flip processes. σ_1 and σ_2 remain constant.

However temporal width of the pump-pulse in this experiment is larger than typical electron-electron thermalization times, even under high excitation densities. Thus the assumption of an electronic equilibrium system described by a transient Fermi-Dirac distribution $f_{Fermi}(\epsilon, t)$ for modeling the measured single particle excitation is justified under these conditions.

Electron-phonon scattering: On a slower timescale of a few hundred femtoseconds up to a few picoseconds the excited electronic system interacts with the lattice by means of electron-phonon scattering.

The strength of the electron-phonon coupling can be expressed by the mass enhancement factor λ. Electron-phonon coupling flattens the dispersion of the electronic states in close vicinity $\pm\hbar\omega_D$ of the Fermi level E_F and thus increases the effective electron mass such that $m^* = m_0(1+\lambda)$, whereas ω_D is the Debye frequency and m^* and m_0 are the effective elective masses with and without electron-phonon coupling respectively. The mass enhancement factor

$$\lambda = 2\int\limits_0^\infty \frac{\alpha^2 F(\omega)}{\omega} d\omega \tag{45}$$

depends on the Eliashberg function $\alpha^2 F(\omega)$, which can be regarded as "the product of a squared matrix element α^2 and the phonon density of states (DOS) $F(\omega)$" depending on the phonon frequency ω. The Eliashberg function $\alpha^2 F(\omega)$ written in a quasi-elastic approximation as [133,134]

$$\alpha^2 F(\omega) \;=\; \sum_{\mathbf{q},\nu,f} |g_{i,f}^{\mathbf{q},\nu}|^2 \delta(\omega - \omega_{\mathbf{q},\nu})\delta(\epsilon_{\mathbf{k},i} - \epsilon_{\mathbf{k},f}) \tag{46}$$

is a sum over all different possibilities to scatter an electron from k_i to k_f involving a phonon $\hbar\omega$ providing the momentum $q = k_f$-k_i. If one assumes a constant matrix element in Eq. 46, free-electron like electronic states and *e.g.* an Einstein model for the phonon distribution function $F(\omega) = \delta(\omega - \omega_E)$, then the Eliashberg function can analytically be expressed as

$$\alpha^2 F(\omega) \;=\; \frac{1}{2}\lambda\; \omega_E\; \delta(\omega - \omega_E). \tag{47}$$

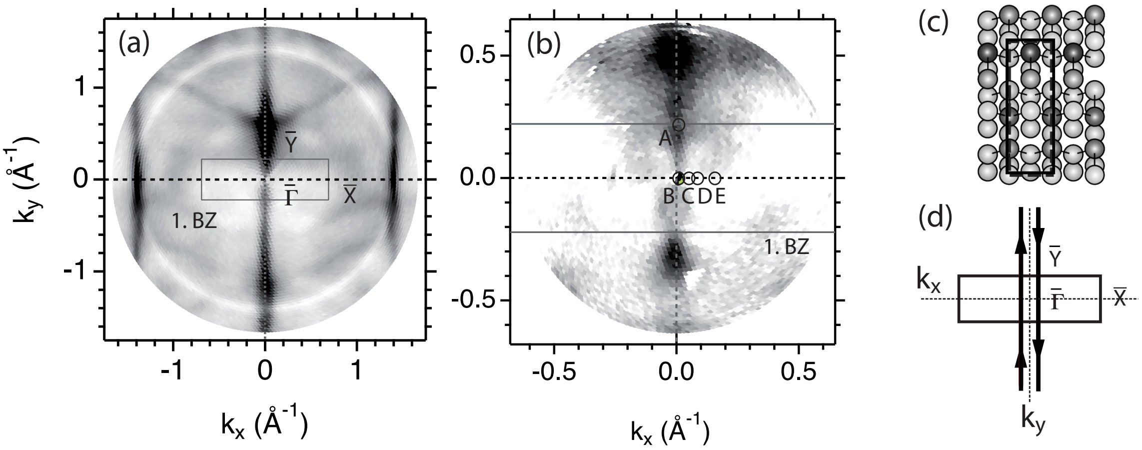

Figure 54: Photoemission intensity at the Fermi energy of a Bi(114) surface, measured by means of continuous 1PPE at a photon energy of hν = 21.21 eV (a) and by 2PPE at $2 \times h\nu = 2 \times 3.1$ eV (b). A, B, C, D and E depict selective spots in the first SBZ, at which the time resolved measurements were made. $(k_x, k_y) = (0\ ,\ 0.219)$; $(0\ ,\ 0)$; $(0.037\ ,\ 0)$; $(0.074\ ,\ 0)$; $(0.147\ ,\ 0)$ Å^{-1}. The borders of the first (1×1) SBZ are drawn (*solid lines*) for the sake of clarity. (c) unit cell of the (1×1) surface in real space (*solid square*) and (d) first SBZ in reciprocal space (*solid square*). The two vertical lines depict the one-dimensional spin-split surface state.

5.3.2 Transient population of the Bi bulk conduction band

Since the workfunction of the clean Bi(114) surface was measured to be $\Phi = 4.32$ eV, the spectral width of the direct 2PPE spectrum at normal emission amounts to ΔE = 4hν - Φ = 1.88 eV. Therefore the small kinetic energy of the photoelectrons limits the detectable parallel momentum in the SBZ to the maximum value of $k_{||} = \sqrt{k_x^2 + k_y^2} \leqslant 0.70$ Å^{-1}. This is the reason for the smaller measured k-space section at E_F in Fig. 54 (b) with $h\nu = 2{\times}3.1$ eV as compared to the larger one in Fig. 54 (a) with $h\nu = 21.21$ eV.

The escape depth and the matrix element for the accessible final states ψ_f strongly depend on the final energy of the photoelectrons. Hence the photoemission distribution is not a priori the same for different photon energies, especially for bulk states due to their dispersion with momentum axis $k_\perp$ along the surface normal. Though the good agreement between the 1D surface state in the FSM in Fig. 54 (a) for $h\nu = 21$ eV (1PPE) and in Fig. 54 (b) for $h\nu = 2{\times}3.1$ eV (direct 2PPE) assures that the same region of the SBZ was probed with 2PPE as in the ARPES experiments of Wells *et al.* [16].

In the following experiment the Bi(114) surface is excited by means of an infrared pulse with 1.55 eV photon energy and a fluence of 2.2 mJ/cm^2. Subsequent probing of the transient occupied ($E_{binding} > 0$) and unoccupied ($E_{binding} < 0$) band structure, by means of 2PPE with the SH probing pulse for variable time delays between -1 ps to +10 ps, has been performed for 5 different k-points in the SBZ of the Bi(114) surface. Point A in the FSM in Fig. 54 (b) with $(k_x, k_y) = (0\ ,\ 0.219)$ corresponds to the $\overline{Y}$-point, lying at the border of the first SBZ of the truncated bulk $(1{\times}1)$

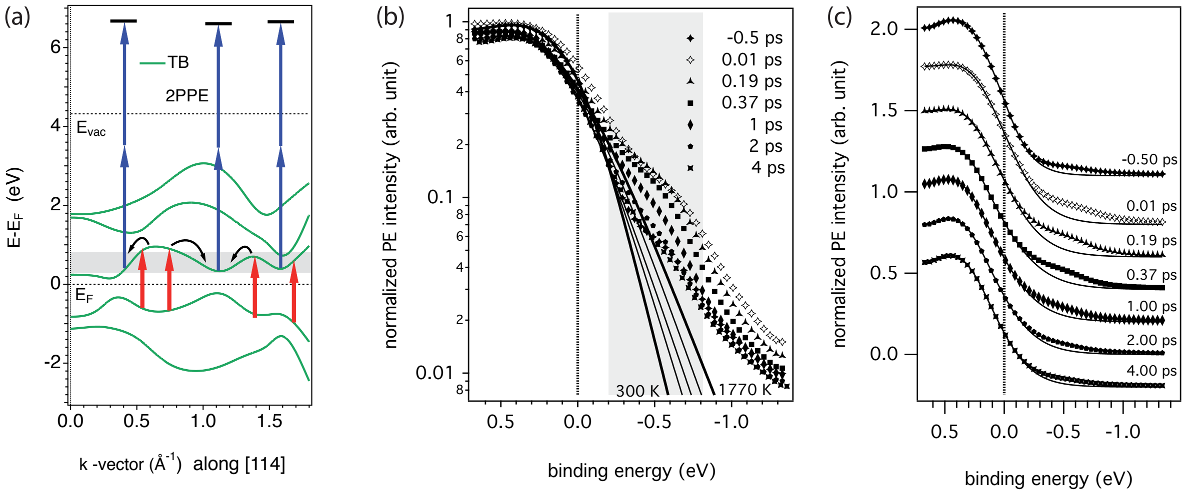

Figure 55: (a) Momentum conserving transitions from the 5th to the 6th valence band (*solid lines*) (both dominantly p-character [136]) along the [114]-direction, obtained from tight-binding (TB) calculations based on the model by Liu and Allen [135]. Electrons are excited by means of 1.55 eV photons (*short arrows*) and the *grey shaded* energy range is subsequently probed by 2PPE with 2×3.1 eV (*long arrows*). (b) Logarithmically and non-logarithmically (c) plotted photoelectron spectra (*markers*) taken along $\overline{\Gamma}$-$\overline{X}$ for various pump probe delays between -0.5 ps and 4 ps clearly showing the pronounced signature of hot electrons above E_F. *Solid lines* are fits to the measured data composed of one Gaussian times a Fermi Dirac distribution.

surface. According to the tight-binding calculations [16] with parameters of Liu and Allen [135] in Fig. 47 (a) bulk states cross the Fermi level E_F at $\overline{Y}$, contributing at $\overline{Y}$ to the DOS in the vicinity of E_F or to the overall conductivity. Points B to E in Fig. 54 (b) have been measured for different polar angles along the $\overline{\Gamma}$-$\overline{X}$ direction, along the dispersion of the one-dimensional surface state and with $k_y = 0$. Note that point C with $(k_x, k_y) = (0.037, 0)$ is exactly where the surface state bands cross the Fermi level [16].

Time-resolved Bi(114) photoelectron spectra from a spectral range between 0.7 eV $> E_{binding} >$ -1.4 eV taken at point C for different delays between -0.5 ps and 8 ps are exemplarily shown in Fig. 55 (b), (c) and in Fig. 56 (a).

Since elastic electron-hole dephasing and inelastic electron-electron thermalization is supposed to happen on a time scale faster then the pump-pulse width, as discussed in paragraph 5.3.1, it is justified to fit the measured TR-ARPES spectra in Fig. 56 with an equilibrium Fermi-Dirac distribution $f(\epsilon, t)$ and to assign an equilibrium electronic temperature $T_F(t)$ to each pump-probe delay t. Note that unlike in the spectra obtained with $h\nu = 21.21$ eV in Fig. 48 the distinct peak due to the 1D surface state at E_F is not clearly visible by eye due to the longer linewidth of the SH pulse compared to the UV light. Hence one Gaussian $G(\epsilon, t)$ for the bulk valence band and the surface state times a Fermi edge $f(\epsilon, t)$ have been fitted to the data in Fig. 56 at each time delay (cf. Fig. 55).

The fits are logarithmically plotted in Fig. 55 (b), clearly revealing a Fermi tail flattening due to

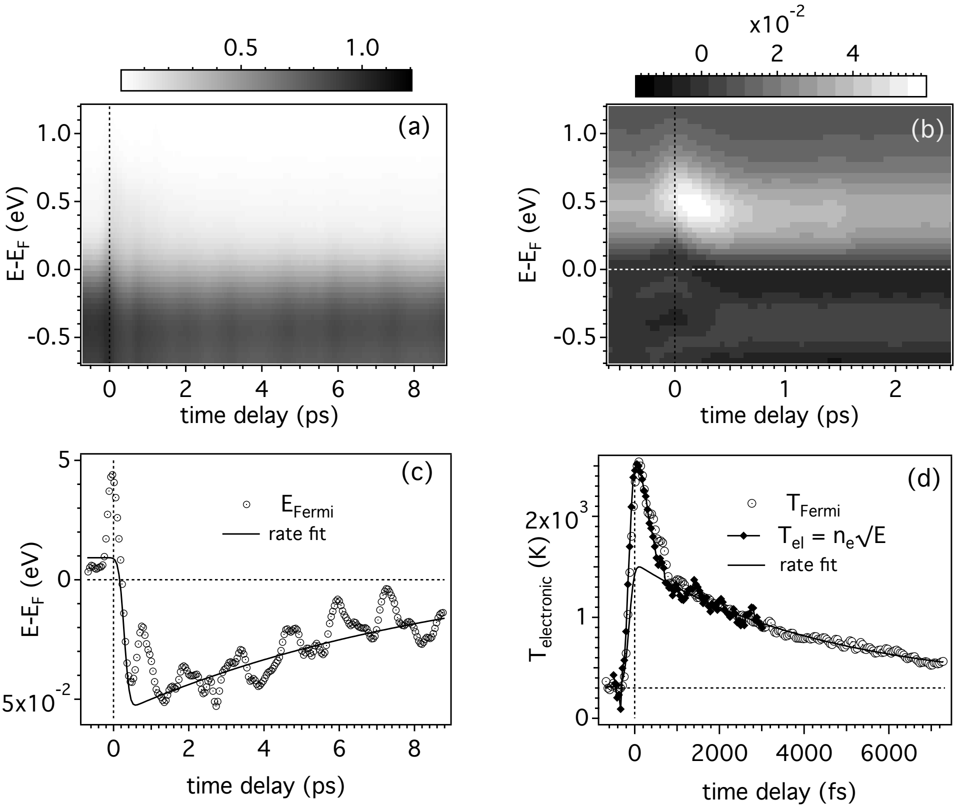

Figure 56: (a) Time-resolved photoelectron spectra from the Bi(114) surface at $(k_x,\ k_y) = (0.037, 0.0)$ for various pump-probe delays between -1 ps and +8 ps. (b) Extracted transient occupation of the Bi conduction band, obtained from subtracting the raw data in (a) from the fitted spectral function in Fig. 55 (c). Fitted transient position of the Fermi level E_F (c) and the fitted Fermi temperature T_F (*open circles*) in (d) as function of pump-probe delay. The measured electronic excess energy above E_F leads to a calculated transient electronic temperature $T_{el}(t) = \int \sqrt{E} \cdot n(E,t)dE$ (*filled diamonds*) in (d).

the infrared irradiation. The Fermi temperature T_F of the electronic system rises from 300 K up to 2500 K within the pump-pulse duration. Subsequent cooling occurs on a timescale of 5.3 ps, as plotted in Fig. 56 (d). In order to obtain T_F the fitted effective temperature T_{eff} has been corrected for the finite energy resolution ΔE_{exp} according to $T_F = \sqrt{(T_{eff})^2 - (\Delta E_{exp}/4k_B)^2}$ [137].

Meanwhile the probed Fermi energy position $E_F(t)$ in Fig. 56 (c) initially shifts by 50 meV towards lower kinetic energies within the pump pulse duration and subsequently recovers on the same timescale (5.3 ps) as the recovery of the Fermi temperature T_F. The modulations of $E_F(t)$ by ±5 meV with a periodicity of 1.3 ps will be the topic of a detailed discussion in Sec. 5.4.2. Note that these fits do not include any unoccupied band structure above the Fermi level E_F as can best be seen from the discrepancy between measurement and fit in Fig. 55 (c) for $t = 0.01$ ps. The additional broad peak around 0.6 eV above E_F is likely to be an unoccupied bulk band of Bi. Indeed time-resolved measurements for different polar angles along the $\overline{\Gamma}$-$\overline{X}$ direction (data not shown here) reveal a weak dispersion for this feature. Since the electrons from the occupied

1D surface state are strongly delocalized along $\overline{\Gamma}$-$\overline{X}$ with an approximate effective mass [22] of $m^* = 0.03 \cdot m_e$ one would expect the unoccupied surface state in the projected bulk band gap to have a similar dispersion. According to the tight binding calculations of Wells *et al.* [16] there is no projected bulk band gap between 0.9 eV and 0.3 eV above E_F along $\overline{\Gamma}$-$\overline{X}$, in agreement with DFT calculations for bulk bismuth by Gonze *et. al.* [138]. Furthermore the lower limit of the detected photoelectrons around 0.3 eV above E_F in Fig. 55 (b) roughly matches the calculated bulk conduction band (CB) bottom. The anticipated unoccupied bulk band projected on the SBZ of the [114] surface along $\overline{\Gamma}$-$\overline{X}$ is visible for both negative and positive delays respectively. Since the SH fluence is rather low and a 3PPE process from the red pulse would be necessary to probe the spectral region at 0.6 eV above E_F one can conclude a thermal occupation at 300 K and for negative delays. Nevertheless one can not fully exclude an exponential non-zero background due to inelastically scattered electrons from a SH 3PPE process around 1 eV above E_F.

At zero pump-probe delay, however, the conduction band is populated by absorption of the infrared pulse with a transient hot electron-hole population, which then subsequently decays for positive delays. Fig. 55 (a) denotes schematically the population by possible momentum-conserving direct transitions from the valence to the conduction bands under absorption of a infrared photon. The subtraction of the fitted spectra, which do not include structure above E_F, from the raw data in Fig. 56 (a) helps to extract the transient occupation of the conduction band, plotted in Fig. 56 (b).

One way to analyze the relaxation of the conduction band is by looking at the energy dependent lifetimes. Cross correlation curves taken from the data in Fig. 56 (a) at fixed energies between 0.9 eV and 0.3 eV above E_F versus pump-probe delay are shown in Fig. 57 (a). The shift of the spectral weight towards the band-bottom for increasing pump-probe delays is outlined with an almost vertical line in Fig. 57 (a) whereas the straight vertical line at 0 fs marks the enhanced photoelectron intensity due to bichromatic (red and blue) multiphoton photoemission processes. The lifetimes have been deduced from the fitted exponential tail for $t \geqslant 300$ fs and plotted versus energy in Fig. 57 (b). Phase space arguments give a qualitative explanation for the increasing lifetimes towards E_F since the number of available states an electron can scatter into decreases upon approaching E_F. The fitted relation $\tau(E) = \tau_0 \cdot (E - E_{CB\ min})^{\alpha}$ leads to an experimental value of $\alpha = -1.51(9)$ which is higher than the expected $\alpha = -2$ from Landau's Fermi liquid theory (FLT) in Eq. 43. This deviation suggests the importance of electron-phonon scattering in addition to electron-electron scattering in the relaxtion of the Bi conduction band. The constant τ_0 obtained in the fit with $\tau_0 = 173(15)$ fs is by a factor of four larger than the one from FLT ($\tau_0 = 43$ fs). Since FLT is based on a three-dimensional free electron gas, the inelastic electron-electron lifetimes per definition do not depend on any band structure but only on the bulk electron density n of a given material. The fact that the measured hot electron population persists several hundred femtoseconds is most likely due to the semi-metallic band structure of bismuth with a

---

[22] The effective mass of the 1D surface state on Bi(114) has been estimated to be $m^* = 0.03 \cdot m_e$ by assuming a parabolic dispersion relation $E(k) = (\hbar\ k)^2/2 \cdot m_{eff}$ and considering the measured spin-splitting of 0.067 $\AA^{-1}$ at ≈ 150 meV above the band bottom [16].

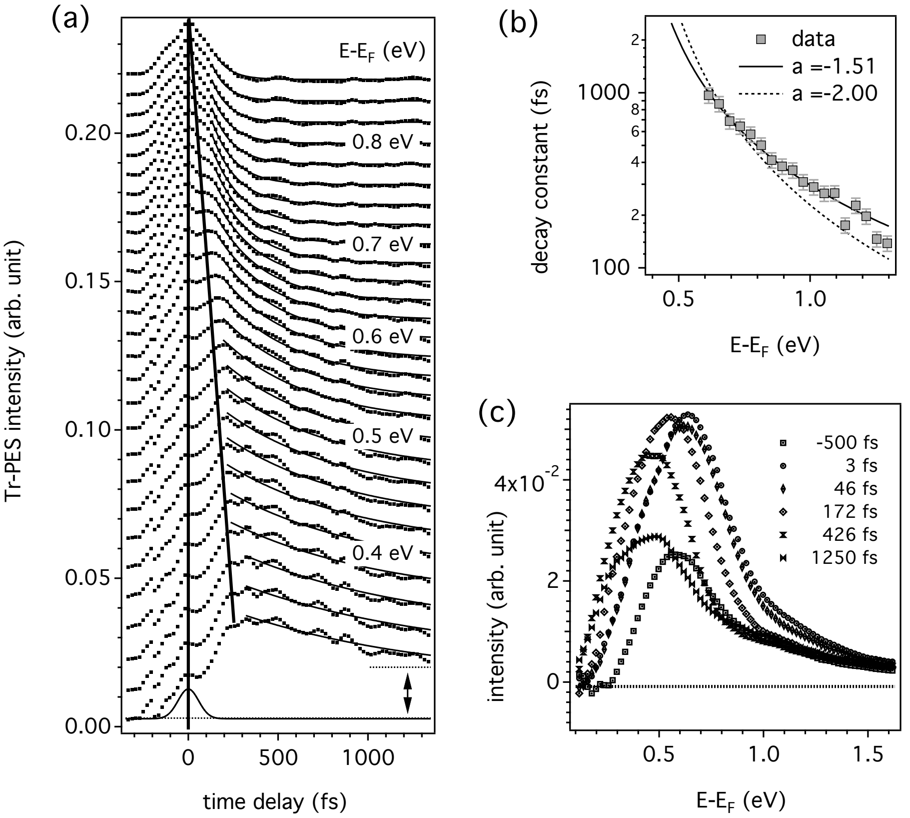

Figure 57: (a) Cross correlation curves obtained from the Bi(114) conduction band at $\overline{\Gamma}$ (point B) for energies between 0.34 eV and 0.86 eV above E_F and pump-probe delays between -500 fs and +1500 fs. (b) extracted decay constants as function of energy above Fermi level E_F. The measured lifetimes fit the relation $\tau = \tau_0(E\text{-}E_{CB\ min})^{\alpha}$ with $\alpha =$ -1.51(9) (*solid line*). (c) Selected extracted photoelectron spectra of the Bi bulk conduction band, thermally populated for negative delays (-500 fs) and transiently populated by means of infrared laser pulse excitation for positive delays (from 0 fs to 1250 fs) respectively.

band gap of roughly 300 meV at E_F. After intraband scattering to the CB bottom $E_{CB\ min}$, the states available for scattering towards E_F between $\overline{\Gamma}$ and $\overline{X}$ in the SBZ are the 1D surface states, but only in close vicinity to the surface where spatial overlap of the wave functions is exists.

5.3.3 Evolution of the electronic temperature

Another way to analyze the relaxation of the transient electron-hole population, induced by the femtosecond infrared laser pulse, is to define an equilibrium temperature T_{el} for the electronic system. Under the assumption, that the transient hot electrons thermalize within the pump pulse duration an equilibrium temperature T_F can be obtained by fitting the Fermi function $f(E, T_F)$ to the measured spectral distribution as shown by *empty circles* in Fig. 56 (d).

Since the pump pulse is shorter than the typical electron-phonon scattering time the absorbed infrared energy density $\epsilon_{h\nu}$ is solely stored within the electronic system [139, 140] immediately after the pump pulse, leaving the lattice temperature T_L essentially unchanged. Thus one can alternatively define an initial maximum electronic temperature $T_{el,max}$ after complete pump pulse irradiation as

$$\epsilon_{h\nu} \;=\; C_{el}\; n_e\; T_{el,max} \;=\; \frac{2\; A\; F_{h\nu}}{z_{h\nu}} \tag{48}$$

with the electron density n_e. The reflectivity R of bismuth leads to an absorption coefficient $A = $ (1-R) and together with the total fluence $F_{h\nu} = \int I_{h\nu}(t)\; dt$ and the absorption length $z_{h\nu}$ to the absorbed energy density which equals $\epsilon_{h\nu}$. The absorbed energy and thus the electronic temperature exponentially decays from the surface towards the bulk with $T_{el}(z,t) = T_{el,max}\; exp(-2z/z_{h\nu})$. The electronic heat capacity C_{el} of bismuth is proportional to the electronic temperature [141] T_{el}

$$C_{el} \;=\; \gamma\; T_{el}, \tag{49}$$

where γ directly depends on the Fermi energy E_F of bulk bismuth and is assumed to be [140]

$$\gamma \;=\; \frac{\pi^2 k_B^2}{2E_F}. \tag{50}$$

Using the experimentally applied fluence on the sample of F = 2.24 mJ/cm^2, a laser absorption depth of $z_{h\nu} = 298$ Å and Eq. 48 the absorbed energy density then amounts to 0.39 × 10^3 J/cm^3. Together with an electron density in bulk bismuth [23] of $n_e = 5.297 \cdot 10^{22}$ cm^{-3} , a Fermi energy E_F = 5.17 eV of bulk bismuth [142], a reflectivity R of 74 % at 800 nm and thus an absorption coefficient A of 0.26 [143] the maximum temperature of the electronic system $T_{el,max}$ right after absorption of the complete pump pulse can be estimated as

$$T_{el,max} \;=\; \left[\frac{4E_F AF}{k_B^2 \pi^2 n_e z_{h\nu}}\right]^{\frac{1}{2}} \;=\; 2550\; K. \tag{51}$$

This value is in good agreement with the values of Boschetto *et al.* [140] for slightly higher fluences and allows to normalize the maximum value of the transient $T_{el}(t)$ at t = 65 fs in Fig. 56 (d) and Fig. 58 (a). One can assume the proportionality [12]

$$\frac{T_{el}(t)}{T_{el,max}} \;=\; \frac{\int \sqrt{E} \cdot n(E,t) dE}{\int \sqrt{E} \cdot n(E,t_{max}) dE} \tag{52}$$

and hence obtain by counting the measured transient electron population above E_F the corresponding electronic temperature $T_{el}(t)$ for all pump-probe delays t in Fig. 56 (d) and Fig. 58 (a). Over a time scale of a few picoseconds electron-phonon interactions cause an equilibrium distribution of the excess energy between the electronic and lattice subsystems, the macroscopic electron-

---

[23] The electron density n_e has been derived from the atomic density of bulk bismuth $n_{Bi} = 2.818 \cdot 10^{22}$ cm^{-3} and the number of available valence electrons of 3.79 per atom (bismuth has 5 valence band electrons with the atomic electron configuration $[Xe]4f^{14}5d^{10}6s^2 6p^3$). The totally absorbed energy per pump pulse of 176 nJ corresponds to $7.1 \cdot 10^{11}$ absorbed photons per pulse. With a beam waist on the sample of 100 μm and an absorption depth of 29.8 nm and hence a probed volume of $1.2 \cdot 10^{-10}$ cm^3 the *excitation density* can be estimated to amount 0.055 electrons per atom.

(T_{el}) and lattice-temperature (T_L) equalize on a excited level, in a time equal to a few phonon oscillation periods [139]. Meanwhile phonon-phonon interactions equally distribute the heat transferred from the electronic system within the lattice subsystem [24]. Finally the two thermalized subsystems relax back to ambient temperature by means of heat diffusion out of the probed volume [144, 145]. Phenomenological two-temperature models describe the temperature relaxation rate of T_{el} and T_L by means of two coupled rate equations. By neglecting the ballistic transport of energy from the surface to the bulk they can be written according to Allen's theory of thermal relaxation of electrons in metals [139] as

$$\frac{\partial T_{el}}{\partial t} = \frac{3\hbar\lambda\langle\omega^2\rangle}{\pi k_B} \cdot \frac{(T_L - T_{el})}{T_{el}} + \frac{A}{C_e} \cdot \int_{-\infty}^{t} I_{h\nu}(t)dt \tag{53}$$

$$\frac{\partial T_L}{\partial t} = -\frac{C_{el}}{C_L} \cdot \frac{3\hbar\lambda\langle\omega^2\rangle}{\pi k_B} \cdot \frac{(T_L - T_{el})}{T_{el}}, \tag{54}$$

where

$$C_{el} = T_{el}\gamma \quad and \quad C_L = 3\langle\hbar\omega_p\rangle\frac{\partial n_p}{\partial T_L} \tag{55}$$

denote the specific electronic and lattice heat capacities with $\langle\hbar\omega_p\rangle$ being the mean phonon energy. The phonon distribution $n_p = (exp(\hbar\omega_p/k_BT_L) - 1)^{-1}$ is given by a Bose-Einstein distribution. The integral over $I_{h\nu}(t)$ in Eqs. 53 represents the laser intensity which exclusively excites the electronic system. Finally λ is the electron-phonon coupling constant, introduced in Eq. 45 which determines the energy transfer rate from the electronic system to the lattice.

Note that ballistic electron transport out of the probed volume as well as lattice heat diffusion by means of anharmonic phonon-phonon scattering is neglected in Eq. 53 and 54 since the corresponding time scales are much longer than the monitored temporal range of 0 ps to 10 ps in this experiment.

The observed electron temperatures $T_{el}(t)$ in Fig. 56 (d) shows a nearly double-exponential decay with a first decay time of τ_i = 400 fs between 150 fs and 0.5 ps and a second τ_{ii} = 5.1 ps for pump-probe delays larger than 0.5 ps. Assuming the Einstein-model for the phonon distribution $F(\omega_P) = \delta(\omega_p - \omega_E)$ the second moment of the Eliashberg function $\lambda\langle\hbar\omega_E\rangle^2$ and thus the dimensionless electron-phonon coupling strength λ can be estimated by fitting Eq. 53 to the first decreasing slope τ_i of $T_{el}(t)$ for 0.1 ps < t < 0.5 ps. Under the assumption of a mean phonon energy of $\hbar\omega_E$ = 65 meV the fitted value of $\lambda\langle\hbar\omega_E\rangle^2 = 1660 \pm 70$ meV^2 would correspond to a coupling strength of $\lambda = 0.4$. The mean phonon energy $\langle\hbar\omega_E\rangle$ as function of λ for the fitted value of 1660 ± 70 meV^2 is plotted in Fig. 58 (b). This estimation is close to the measured value by Gayone *et al.* at the hole pockets of a Bi(111) surface, obtained from temperature dependent angular distribution curves (MDC) analysis [146]. It was argued that the substantial higher λ at metallic bismuth surfaces could be due to the higher DOS of electronic surface states at E_F as

---

[24] The phonon-phonon scattering rate can be estimated to be in the order of $\Gamma_{p-p} = \omega_D \frac{T_L}{T_D}$ with a Debye frequency $\omega_D = 1.56 \cdot 10^{13}$ s^{-1}, T_L = 300 K and a Debye temperature T_D = 119 K of bismuth which corresponds to phonon-phonon scattering timescales between 10 fs and 100 fs. [140]

compared to the lower DOS and thus the lower λ for semimetallic bulk bismuth. Kirkegaard *et al.* question this argument because of the strong spin-orbit coupling and the resulting spin-split nature of the surface states in bismuth, which is supposed to drastically reduce the possible scattering phase space [134].

However such a two-temperature model in Eq. 53 and 54 is not fully capable to explain the obtained curve of the electronic temperature $T_{el}(t)$ in Fig. 56 (d), especially the kink between the two distinct decay times τ_i and τ_{ii}. It is rather unlikely that T_{el} and T_L fully thermalize with each other ($T_{el} = T_L$) within the first 500 fs after pump pulse irradiation since the electronic heat capacity C_{el} is too low compared to the one of the lattice C_L.

Perfetti *et al.* developed a three-temperature model in order to explain the ultrafast electron-phonon dynamics in the anisotropic $Bi_2Sr_2CaCu_2O_{8+\delta}$ (Bi-2212) compound [147]. They found the hot electrons to thermalize within 50 fs and assigned a delay dependent electronic temperature $T_{el}(t)$. The hot electrons subsequently scatter only with a minor subset of strongly coupled phonons, described by a hot phonon temperature T_p. Within a timescale $\tau_i = 110$ fs the electrons and the small fraction m of non-equilibrium phonons thermalize, roughly until $T_{el} = T_p$. An observed kink in $T_{el}(t)$ appears at 330 fs, corresponding to an energy bottleneck. T_{el} and T_p have completely thermalized far above the equilibrium temperature of the lattice T_L. On a slower second timescale of $\tau_{ii} = 2$ ps the excess energy relaxes from the strongly coupled phonon bath to the large amount of $(1 - m)$ cold lattice modes with temperature T_L and with inferior coupling by means of anharmonic phonon-phonon scattering. T_{el}, T_p and T_L satisfy the given rate equations [147]

$$\frac{\partial T_{el}}{\partial t} = -\frac{3\hbar\lambda\omega_E^2}{\pi k_B} \cdot \frac{T_{el} - T_p}{T_{el}} + \frac{A\int_{-\infty}^{t} I_{h\nu}(t)dt}{C_{el}} \tag{56}$$

$$\frac{\partial T_p}{\partial t} = \frac{3\hbar\lambda\omega_E^2}{\pi k_B} \cdot \frac{C_{el}}{C_p} \cdot \frac{T_{el} - T_p}{T_{el}} - \frac{C_p}{C_L} \cdot \frac{T_p - T_L}{\tau_{ii}} \tag{57}$$

$$\frac{\partial T_L}{\partial t} = \frac{C_p}{C_L} \cdot \frac{T_p - T_L}{\tau_{ii}}. \tag{58}$$

The corresponding heat capacities of the lattice C_L and the strongly coupled phonon subset C_p depend on the size of the subset described by the fraction m and the phonon temperature T_p. They are given by $C_L = (1 - m) \cdot 3\langle\hbar\omega_E\rangle(\partial n_p/\partial T_L)$ and $C_L = m \cdot 3\langle\hbar\omega_E\rangle(\partial n_p/\partial T_L)$.

Relaxation dynamics, macroscopically described by equilibrium temperatures, revealing two different relaxation timescales $\tau_i \ll \tau_{ii}$, can indicate a sudden reduction of energy flow [147]. Even in gapless compounds, as *e.g.* graphite such a 'bottleneck' has even been found. Kampfrath *et al.* investigated ultrafast charge carrier dynamics in graphite by time-resolved terahertz spectroscopy and found that more than 90% of the initially deposited excitation energy is transferred to a few strongly coupled lattice vibrations within 500 fs [148]. The hot phonon modes then persist over a few picoseconds. In general such a situation of a small strongly coupled phonon subset leading to an energy bottleneck can be expected for systems with a strong directional conduction and bonding [129, 149].

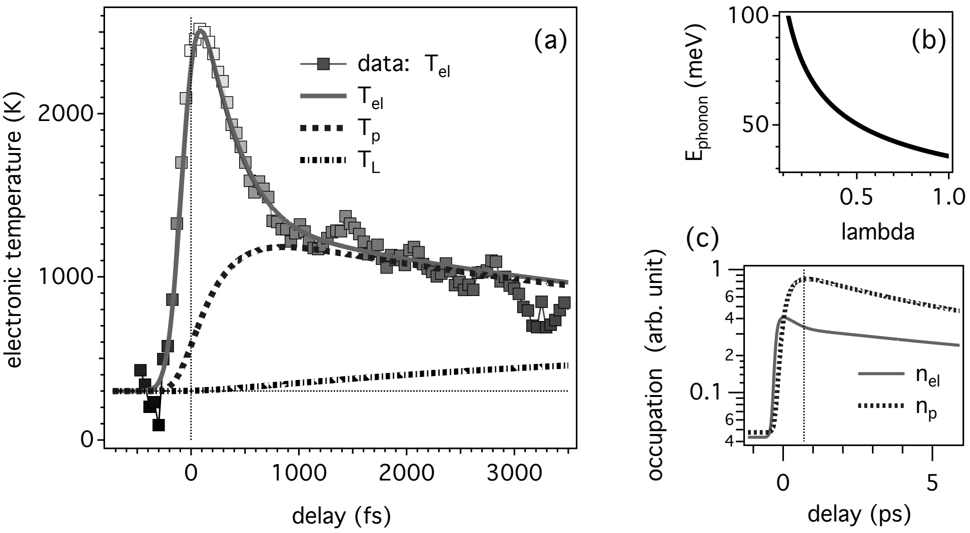

Figure 58: (a) Measured transient electronic temperature $T_{el}(t)$ of the Bi(114) surface, obtained with Eq. 52 from the hot electron population in Fig. 56. (b) The experimentally determined moment of the Eliashberg function $\lambda(\omega_E)^2$ of 1660 ± 70 meV^2 leads to possible mean phonon energies as function of the electron-phonon coupling constant λ. (c) Corresponding normalized phononic and electronic occupation numbers n_p and n_{el}, directly depending on T_p and T_{el} via the Bose-Einstein and the Fermi-Dirac statistics.

Anticipating that it is the case for the strongly anisotropic vicinal Bi(114) surface as well, Eqs. 56, 57 and 58 have been numerically fitted to $T_{el}(t)$. For a pump-probe pulse cross correlation width of 155 fs, a maximal electronic temperature of 2550 K (from Eq. 51), a second and slower relaxation time of τ_{ii} = 5.1 ps and a moment of the Eliashberg function of $\lambda\langle\hbar\omega_E\rangle^2$ of 1660 ± 70 meV^2, the fitted relative subset size of m = 26 ± 5 % seems to reproduce the data best. This means that initially after the pump pulse excitation the thermalized hot electron population interacts for a few hundred femtoseconds almost exclusively with a strongly coupled fraction of only 26% of all lattice phonons. One may conjecture that on the longer time scales of τ_{ii} = 5.1 ps the hot electron and hot phonon baths thermalize with the rest of the lattice by means of phonon-phonon scattering. The calculated lattice temperature T_L after 6 ps amounts to 520 K.

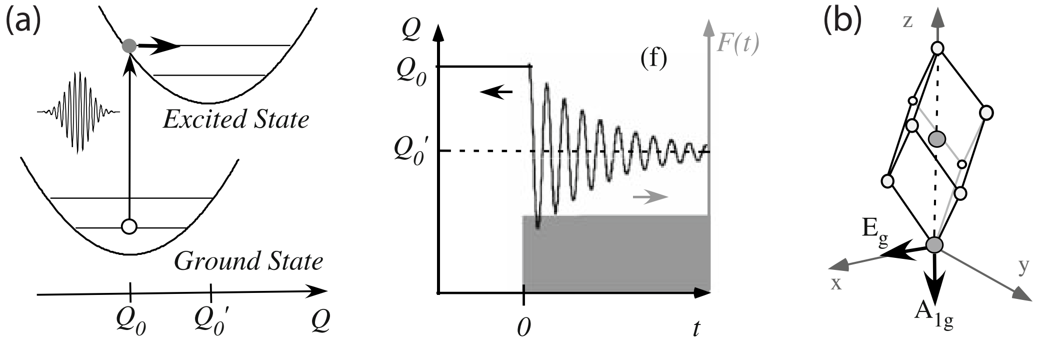

Figure 59: Schematic view of coherent phonon excitation (courtesy of Ishioka *et al.* [150]). (a) Total energy diagram for displacive excitation of coherent phonons (DECP) from the equilibrium atomic coordinate Q_0 to $Q_0^{'}$; temporal evolution of the driving force $F(t)$ (grey area) and of the corresponding nuclear displacement $Q(t)$ (solid line). (b) Crystalline A_7 structure of Bi indicating the directions of the A_{1g} and the E_g modes.

5.4 Displacive excitation of coherent optical phonons at the Bi(114) surface

5.4.1 Introduction to displacive excitation of coherent optical phonons

Bismuth is well known for the displacive excitation of coherent phonons (DECP) by means of femtosecond laser pulses. Transient reflectivity measurements [151, 152] and time-resolved X-ray diffraction measurements [153–155] revealed coherent electronic excitations to be the driving force for DECP in bismuth on an ultrafast time scale. A transient hot electron population $n(t)$ changes the lattice potential and thus the equilibrium position of the ion cores from Q_0 to $Q_0^{'}$ such that the atoms start to perform damped oscillations [151, 156], as schematically drawn in Fig. 59 (a). The equilibrium structure A_7 of Bi is a distortion from the cubic structure along the rhombohedral [111]-direction in Fig. 59 (b), which is stabilized by the so called Peierls-Jones mechanism [157]. Being responsible for the semimetallic character of bismuth, the spatial Peierls distortion opens up a small electronic bandgap over an expanded region of the BZ. Due to the low DOS around the Fermi level this equilibrium structure, particularly given by the interatomic distance of the two atoms in the unit cell, is very sensitive to the excitation of electrons to higher bands. A small relative number of photoexcited electron-hole pairs of about <1% can lead to a coherent oscillation of the Bi atoms along the [111]-body-diagonal. This coherent oscillation represents the totally symmetric A_{1g} optical phonon mode along the trigonal axis of the unit cell in real space (z-axis in Fig. 59) which is located at the center of the Brillouin zone Γ *i.e.* at $k = 0$ in reciprocal space.

5.4.2 Coherent excitation of optical phonons on Bi(114)

The relaxation dynamics of the electronic system, macroscopically described by a transient electronic temperature $T_{el}(t)$ in paragraph 5.3.3 give support to the existence of a subset of strongly

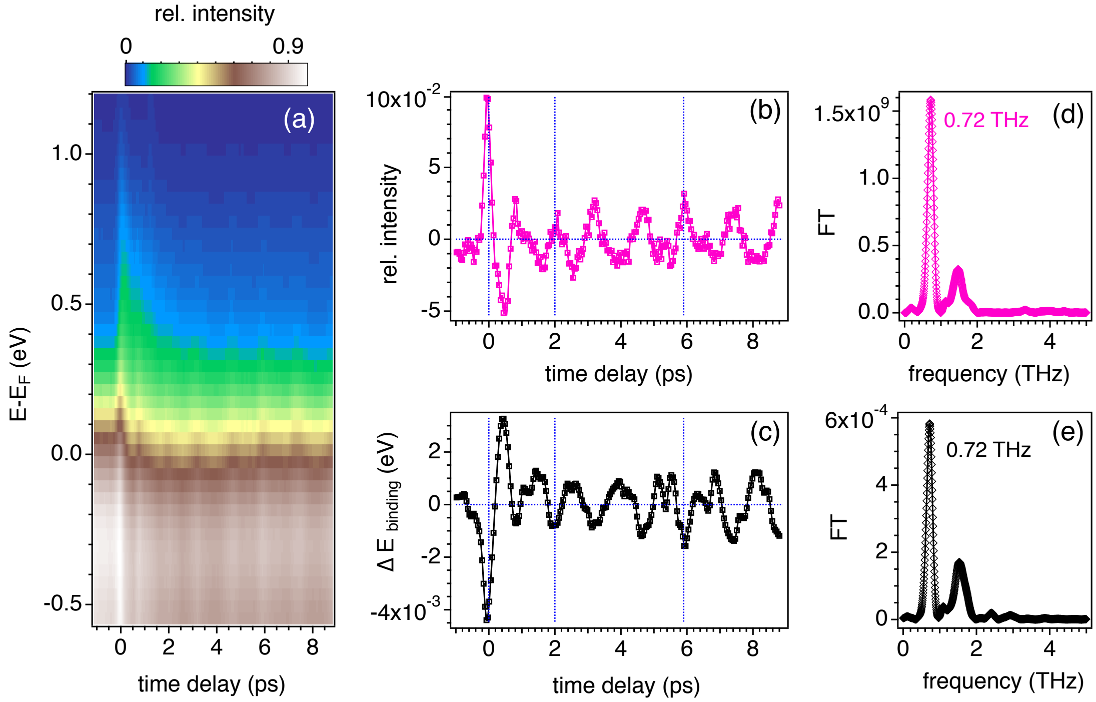

Figure 60: (a) Intensity map of the photoelectron counts (normalized to the maximum intensity) as function of time delay between pump and probe pulse, acquired at $(k_x,\, k_y) = (0.037,\, 0)$ Å^{-1} in the SBZ (point C in the FSM in Fig. 54 (b)). (b) Change in photoemission intensity and (c) variation of the center of mass energy position after subtraction of a smooth background function. (d) and (e) are the Fourier transforms of the curves in (b) and (c) for time delays $>$ 700 fs, respectively.

coupled phonon modes at the Bi(114) surface, phase locked by the pump pulse over a large spatial region. Indeed the photoelectron spectra for various pump-probe delays in Fig. 60, measured for different k-points along $\overline{\Gamma}$-$\overline{X}$, reveal periodic modulations on a picosecond time scale. The spectra show a periodic temporal change in the intensity in Fig. 60 (b) and in the center-of-mass of the bands as shown in Fig. 60 (c). A Fourier transform (FT) of the oscillations reveals the peaks of the same frequency components as the periodic rigid shift of the chemical potential in Fig. 56 (c). The electron-phonon coupling constant λ is known to connect the coherent lattice distortions and subsequent periodic vibrations with the electronic bandstructure causing periodic shifts in energy and intensity modulations in the photoelectron spectra [83,129,161,162]. Thus the corresponding FT in Figs. 60 (d) and (e) should directly indicate the contribution of the different coherent modes in the phonon frequency domain. For the measured k-point C at $(k_x; k_y) = (0.037;\, 0)$ the FT reveals two dominant frequencies, first at 0.72(6) THz and second at 1.53(7) THz, respectively. The relative contribution of the measured modes in the FT can be compared with the calculated phonon density of states $F(\omega)$ for Bi [158] in Fig. 61 (b). If the value α^2 in Eq. 47 is assumed to be constant, the relative contribution $\frac{d\lambda}{d\omega}$ from a phonon mode in the energy range $[\omega, \omega + d\omega]$ to the total electron-phonon coupling in Eq. 45 and thus to the periodic modulations in the

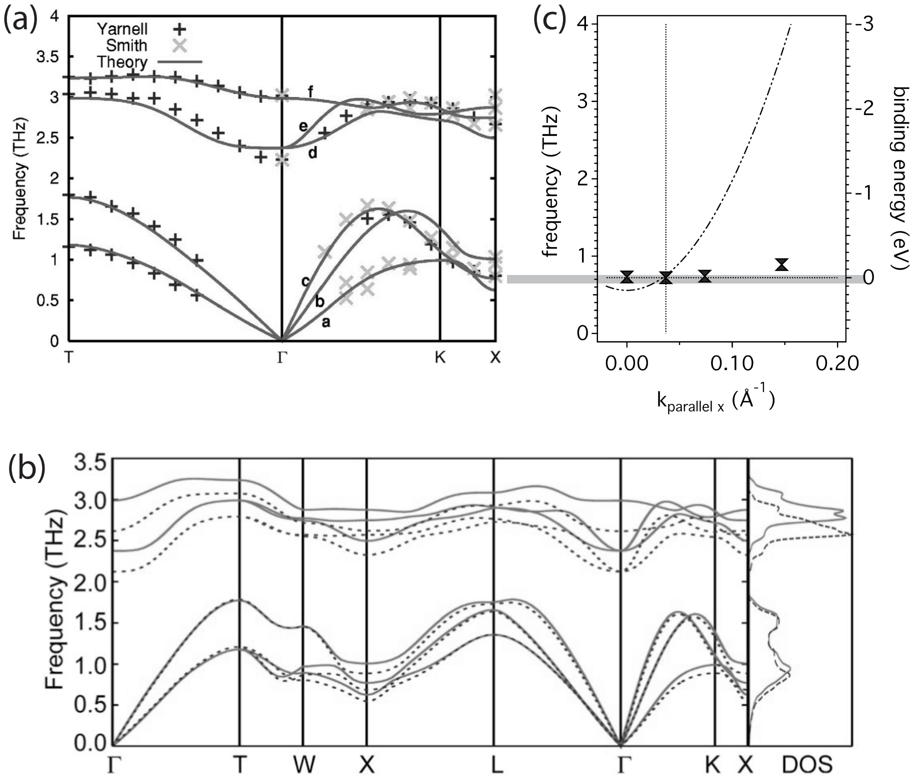

Figure 61: (a) Calculated phonon dispersions curves (*solid lines*) from Murray *et al.* (Ref. [158]) for the ground state with n = 0% excited valence electrons. In comparison experimental neutron scattering results of Yarnell et al. (Ref. [159]) and Smith (Ref. [160]) (*markers*). Labels a through f correspond to the calculated modes described in Ref. [158], respectively. (b) Phonon dispersion curves by Murray *et al.* [158] of the ground state (n = 0%; *solid line*) and for n = 1% excited valence electrons (*dashed line*), respectively. (c) Main frequencies from the Fourier transform (FT) versus the electronic k-vector along $\overline{\Gamma}$-$\overline{X}$. *Dashed parabola* as guideline to the eye, marking the Fermi energy crossing of the 1D surface state as function of k_x.

photoelectron spectra are proportional to $F(\omega)/\omega$. Fig. 62 directly compares the experimentally obtained FT with the quantity $F(\omega)/\omega$. They are in reasonable agreement except for the missing A_{1g} mode in the data between 2.6 THz and 2.9 THz. One could speculate that the given temporal width of the fundamental pump pulse of 280 fs was not sufficiently short enough to coherently excite modes with $T/2 = 170$ fs. The effect of these lattice vibrations on the photoelectron spectra can not be resolved under incoherent excitation conditions.

On the other hand the strongest contribution between 0.7 THz and 0.8 THz have been found for all measured points B to E along $\overline{\Gamma}$-$\overline{X}$, plotted in Fig. 61 (c). Because the pump-pulse duration is shorter than 1/2 of the oscillation period a phase relation is established with respect to time zero. The calculated phonon dispersion of the six branches by Murray *et al.* [158] are shown in Fig. 61. The first-principle DFT calculations are in good agreement with results from several neutron scattering experiments [159, 160]. According to Murray *et al.* branch c in Fig. 61 (a)

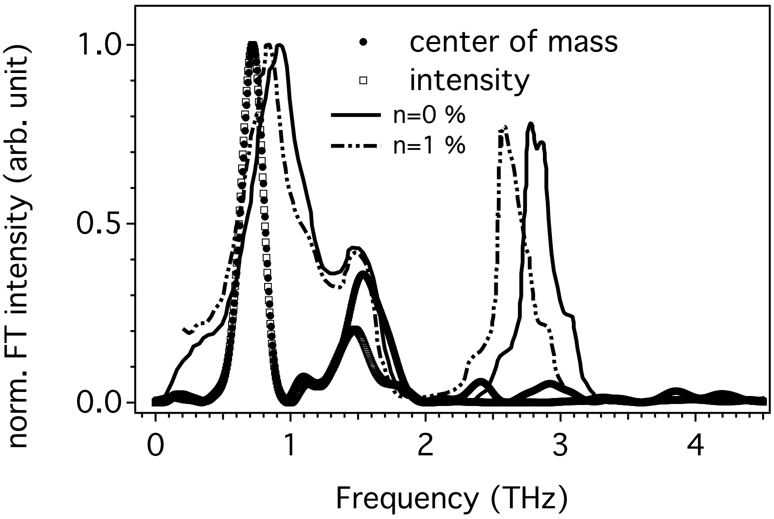

Figure 62: Calculated phonon DOS from Ref. [158] divided by $1/\omega_p$ for the ground state (n = 0%; *solid line*) and for n = 1% excited valence electrons (*dashed line*) respectively. *Round markers* represent the experimentally obtained FT at k-point C at $(k_x; k_y) = (0.037; 0)$.

has transversal optical character at the X-point of the Brillouin zone (BZ) [158]. The calculated frequency of the phonons from branch c at the X-point in the BZ amounts to 0.77 THz for $n = 0\%$ and to 0.69 THz for $n = 1\%$ excited valence band electrons respectively. These values are close to the measured values along $\overline{\Gamma}$-$\overline{X}$ (point B to E in the SBZ), plotted in Fig. 61 (c). Note that in the case of generic coherent phonons one would not expect differing frequencies or phases in the spectral distortions for different k-points [162].

A necessary condition for a coherent modification of the surface electronic structure over a macroscopic spatial area is the non-propagating character of the optical phonon. Owing to the fact that the X-point corresponds to a reciprocal lattice vector in bulk Bi the calculated mode at 0.7 THz fulfills this condition with $\partial\omega/\partial k = 0$. Furthermore the Γ-K-X-direction runs parallel to the binary axis of the Bi crystal and along the atomic rows of the Bi(114) surface, as shown in Fig. 63 (a). The found 0.72 THz mode can therefore be assigned to a standing wave along the atomic rows of the Bi(114) surface with a wavelength of 4.53 Å. The wavelength corresponds to the length of the surface unit cell along the $[1\bar{1}0]$-direction.

Time-resolved X-ray diffraction data from the (111) lattice planes in bulk Bi by Johnson *et al.* reveal the non-propagating A_{1g} mode at the Γ-point of the BZ with a frequency of 2.61 THz to be the dominant contribution [155]. Since time-resolved X-ray diffraction is a bulk sensitive technique which probes a macroscopic volume the effect of coherent phonons at the surface is expected to be much weaker. That may explain the absence of the low frequency modes in these experiments. In contrast to that the TR-ARPES experiments in this work are very surface sensitive due to the low mean free path of the photoelectrons at low kinetic energy. The surface is macroscopically excited within an area of the pump beam focus but the probe pulses can only access the electronic structure in close proximity of the surface.

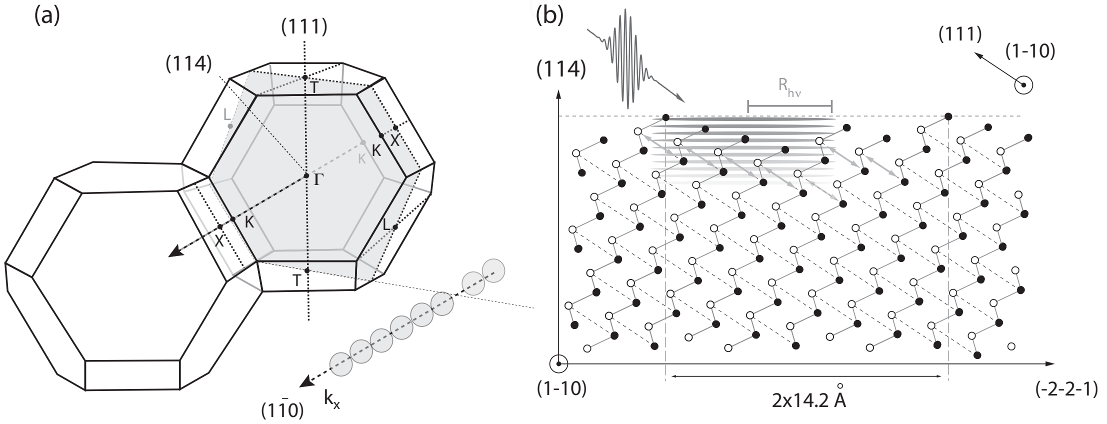

Figure 63: (a) Brillouin zone of the spatial A 7 rhomboedral structure of Bi. (b) Schematic sketch of the laser excited Bi(114) surface, parallel to the mirror plane of the Bi crystal.

According to the estimations in paragraph 5.3.3 damping of the oscillations should occur on the slow timescale τ_{ii} of 5.1 ps. Phase space arguments could account for the weak damping of the coherent oscillation [129]. The coherent phonon mode can only decay by electron-hole pair generation in a small energy range with excitation energy $E_{final} \simeq \hbar\omega_E \simeq 3$ meV. The electronic structure at the Fermi energy of the vicinal Bi(114) surface consists of only two crossings of the surface state with opposite spin and $\mathbf{k}$ vector, corresponding to the 1D line along $\overline{\Gamma}$-$\overline{Y}$. Thus the bulk band gap [16] of roughly 300 meV at $\overline{\Gamma}$ precludes the decay by scattering with occupied electronic bulk states. Only scattering with the low DOS of the surface state electrons and the anharmonic decay channel to other phonon modes is available. Therefore the decay channel of phonon-phonon interaction has a τ_{ii} in the order of several picoseconds.

Conclusion: In summary, evidence for the displacive excitation of coherent phonons at the Bi(114) surface was presented. As already conjectured in previous studies, the coherent excitation of electron-hole pairs in the Bi bulk conduction band and the subsequent population decay, mainly dominated by means of electron-phonon coupling, is the driving force for the coherent phonon excitation. Analysis of the transient electronic temperature $T_{el}(t)$ in Sec. 5.3.3 reveals a double exponential decay, indicating an energy bottle neck in the relaxation process. A phenomenological three-temperature model fits well the data, including besides the electronic T_{el} and lattice temperature T_L a third temperature T_p representing a small subset of strongly coupled phonons. From comparison with theoretical phonon dispersion calculations the strong periodic modification of the time-resolved photoelectron spectra can be caused by optical phonons with a frequency of 0.7 THz, forming a standing wave along the atomic rows of the vicinal Bi(114) surface.

6 Conclusions and outlook

Elliptical Display Analyzer (EDA): Main topic in the "machine-part" of this work was the commissioning and characterization of the EDA by photoemission with low energy laser pulses from one- and two-dimensional metallic surface states from the Bi(114) and Cu(332) surface, respectively.

The most remarkable result is the decomposition of the spin-splitting in the one-dimensional surface state on Bi(114) by means of circular dichroism in the angular distribution (CDAD) using femtosecond 6 eV pulses. The results are in agreement with the spin-resolved data based on Mott-scattering experiments. The parallel data acquisition avoids matrix-element effects and allows for short data acquisition times over large acceptance angles of ± 43°. Note that it is a priori not clear whether a dichroic asymmetry in the angular distribution originates from the spatial symmetry of the involved initial and final states or from the spin of the electron via relativistic spin-orbit coupling. Therefore such a method can only be applied in combination with previous spin-resolved photoemission studies based on conventional Mott-scattering.

Unfortunately the performance of the EDA turned out to be insufficient regarding TR-ARPES applications around the Fermi level. First the main limiting factor is the measured signal to noise ratio. Laser pulse induced transient changes of the occupied and unoccupied band structure have to amount to more than 5 % of the strongest features in the occupied band structure around E_F in order to be distinguished from background fluctuations. Note that this is still the case after post processing of the data for normalization of the detector over the whole acceptance range. Second the energy resolution of the analyzer is limited to values larger than 100 meV. This is mainly due to the reflection characteristics of the photoelectrons at the ellipsoidal mirror as well as due to spatial inhomogeneities of the work function at different parts of the detector, respectively.

The *h*-BN/Ni(111) and *h*-BN/Rh(111) interface: Monolayers of hexagonal boron nitride (*h*-BN) on various metal surfaces have widely been studied in our group in the past few years. For certain metal surfaces such as Rh(111) boron nitride forms corrugated superstructures, for other surfaces as Ni(111) the boron nitride monolayers stay atomically flat, depending on the given lattice mismatch with respect to the metal surface substrate. Such metal-insulator interfaces reveal an additional type of unoccupied electronic states compared to bare metal surfaces. These so called interface states are spatially located between the metal surface and the dielectric overlayer, in analogy to the interlayer states in bulk boron nitride. For *h*-BN/Ni(111) the existence of an interface state has been predicted by means of both DFT calculations and DCM calculations and for the first time measured with TR-2PPE by Muntwiler *et al.* [46]. Resonant two-photon photoemission (2PPE) was applied in this work in order to investigate the binding energy and the free-electron like dispersion of these states on both systems *h*-BN/Ni(111) and *h*-BN/Rh(111), respectively. The large difference in binding energy of 190 meV between inverse photoemission experiments and 2PPE measurements from *h*-BN/Ni(111) raises speculations about an excitonic pairing of the interface electron with the remaining photohole in the Ni *d*-band which would lead to an enhanced binding energy in the case of 2PPE. Further experiments should trace the dependance of the measured effective mass systematically for a larger variety of pump photon energies. The corrugation of the *h*-BN superstructure on Rh(111) affects the electronic structure of the occupied BN-related bands. 3PPE investigations on *h*-BN/Rh(111) reveal indications for the existence of a split pair of interfaces states in analogy to the split occupied σ states at the center of the BZ. This finding is supported by the measured binding energies, dispersions and the relative ratio of both spectral features. Selective excitation of the state from the pores of the *h*-BN/Rh(111) nanomesh may allow for the observation of a lensing effect in the angular distribution of the photoelectrons.

Beside the interface state an unoccupied image potential state (IPS) appears as second distinct feature in the 2PPE spectra from *h*-BN/Ni(111). Located a few Å outside of the metal-insulator interface the lowest lying IPS serves as probe for the ferromagnetic phase transition of the underlying Ni substrate. The energy position of the IPS is sensitive to variations of the magnetization state across the Curie temperature. Similar shifts in the energy position of the IPS were found in the TR-2PPE spectra 300 fs after the irradiation with intense infrared laser pulses from *h*-BN on thin Ni(111) films. A possible explanation could be the ultrafast demagnetization of the Ni film on a femtosecond time scale.

Using such high excitation densities, typically in the order of several mJ/cm^2, large photo currents are generated in the order of 10^3 photoemitted electrons per pulse. Spectral shifts and broadenings arise as a consequence from mutual Coulomb repulsion between the electrons in vacuum. A simple but complete model reproduces the measured space-charge effects based on a charged disk model by iterative calculation of the propagation. The simulations allow the electron dynamics within the solid to be disentangled from the spectral changes induced by mutual Coulomb repulsions in the vacuum. A given example is the time-resolved measurement and simulation of an additional polarisation dependent multi photon transition in the high excitation regime including the lifetime and symmetry of the involved intermediate interface state.

The quasi one-dimensional Bi(114) surface: TR-ARPES experiments from the Bi(114) were performed. The intense infrared laser pulse creates a transient hot electron population in the unoccupied conduction band of bismuth which subsequently decays by means of electron-electron, electron-hole and electron-phonon scattering processes. The analysis of the electronic temperature within the framework of a common phenomenological three-temperature model indicates the excitation of coherent optical phonons at the Bi(114) surface on a femtosecond time scale. As a consequence the coherent lattice modes periodically modulate the measured transient electronic structure on a picosecond time scale. From comparison with theoretical phonon dispersion calculations the strong periodic modification of the time-resolved photoelectron spectra have been identified to be caused mainly by optical phonons, with a frequency of 0.7 THz, forming a standing wave along the atomic rows of the vicinal Bi(114) surface.

References

[1] D. E. Eastman, J. J. Donelon, N. C. Hien, and F. J. Himpsel, *An Ellipsoidal Mirror Display Analyzer System for Electron Energy and Angular Measurements*, Nucl. Instrum. Methods Phys. Res. **172**, 327 (1980).

[2] T. Dütemeyer, C. Quitmann, and M. Kitz, *Photoelectron imaging using an ellipsoidal display analyzer*, Review of Scientific Instruments **72**, 2638 (2001).

[3] T. Dütemeyer, *Elliptical Display Analyzer (EDA)*, PhD thesis, University of Dortmund, 1999.

[4] P. Kirchmann, L. Rettig, D. Nandi, U. Lipowski, M. Wolf, and U. Bovensiepen, *A time-of-flight spectrometer for angle-resolved detection of low energy electrons in two dimensions*, Appl. Phys. A **91**, 211 (2008).

[5] SPECS Surface Nano Analysis GmbH, Voltastrasse 5, 13355 Berlin, Germany, *THEMIS 600/1000*, 2010.

[6] B. D. Patterson, L. Heyderman, C. Milne, P. Thibault, K. Ballmer, and U. Staub, *Ultrafast Phenomena at the Nanoscale: Science opportunities at SwissFEL X-ray Laser*, Technical report, Paul Scherrer Institute (PSI), 2009.

[7] M. Muntwiler, Q. Yang, W. A. Tisdale, and X. Y. Zhu, *Coulomb Barrier for Charge Separation at an Organic Semiconductor Interface*, Phys. Rev. Lett. **101**, 196403 (2008).

[8] Th. Gerrits, H. A. M. van den Berg, J. Hohlfeld, L. Bär, and Th. Rasing, *Ultrafast precessional magnetization reversal by picosecond magnetic field pulse shaping*, Nature **418**, 509 (2002).

[9] I. Tudosa, C. Stamm, A. B. Kashuba, F. King, H. C. Siegmann, J. Stöhr, G. Ju, B. Lu, and D. Weller, *The ultimate speed of magnetic switching in granular recording media*, Nature **428**, 831 (2002).

[10] C. D. Stanciu, F. Hansteen, A. V. Kimel, A. Kirilyuk, A. Tsukamoto, A. Itoh, and Th. Rasing, *All-Optical Magnetic Recording with Circularly Polarized Light*, Phys. Rev. Lett. **99**, 047601 (2007).

[11] E. Beaurepaire, J.-C. Merle, A. Daunois, and J.-Y. Bigot, *Ultrafast spin dynamics in ferromagnetic nickel*, Phys. Rev. Lett. **76**, 4250 (1996).

[12] H.-S. Rhie, H. Dürr, and W. Eberhardt, *Femtosecond Electron and Spin Dynamics in Ni/W(110) Films*, Phys. Rev. Lett. **90**, 247201 (2003).

[13] M. Cinchetti, M. S. Albaneda, D. Hoffmann, T. Roth, J.-P. Wüstenberg, M. Krauß, O. Andreyev, H. C. Schneider, M. Bauer, and M. Aeschlimann, *Spin-Flip Processes and Ultrafast*

Magnetization Dynamics in Co: Unifying the Microscopic and Macroscopic View of Femtosecond Magnetism, Phys. Rev. Lett. **97**, 177201 (2006).

[14] B. Koopmans, G. Malinowski, F. D. Longa, D. Steiauf, M. Fähnle, T. Roth, M. Cinchetti, and M. Aeschlimann, *Explaining the paradoxical diversity of ultrafast laser-induced demagnetization*, Nature Mat. **9**, 259 (2010).

[15] C. Stamm, T. Kachel, N. Pontius, R. Mitzner, T. Quast, K. Holldack, S. Khan, C. Lupulescu, E. F. Aziz, M. Wietstruk, H. A. Dürr, and W. Eberhardt, *Femtosecond modification of electron localization and transfer of angular momentum in nickel*, Nature Mat. **6**, 740 (2007).

[16] J. W. Wells, J. H. Dil, F. Meier, J. Lobo-Checa, V. N. Petrov, J. Osterwalder, M. M. Ugeda, I. Fernandez-Torrente, J. I. Pascual, E. D. L. Rienks, M. F. Jensen, and Ph. Hofmann, *Nondegenerate Metallic States on Bi(114): A One-Dimensional Topological Metal*, Phys. Rev. Lett. **102**, 096802 (2009).

[17] M. König, S. Wiedmann, C. Brüne, A. Roth, H. Buhmann, L. W. Molenkamp, X.-L. Qi, and S.-C. Zhang, *Quantum Spin Hall Insulator State in HgTe Quantum Wells*, Science **318**, 766 (2007).

[18] H. Hertz, *Über den Einfluss des ultravioletten Lichts auf die elektrische Entladung*, Ann. Phys. **31**, 983 (1887).

[19] A. Einstein, *Über einen die Erzeugung und Verwandlung des Lichts betreffenden heuristischen Gesichtspunkt*, Ann. Phys. **14**, 164 (2005, reprint).

[20] S. Hüfner, *Photoelectron Spectroscopy*, Springer Series in Solid-State Sciences 82, 1995.

[21] W. Demtröder, *Laser Spectroscopy, Basic Concepts and Instrumentation*, Springer Verlag, third edition edition, 2003.

[22] H. Petek and S. Ogawa, *Femtosecond time-resolved two-photon photoemission studies of electron dynamics in metals*, Prog. Surf. Sci. **56**, 239 (1995).

[23] T. Greber, O. Raetzo, T. Kreutz, P. Schwaller, W. Deichmann, E. Wetli, and J. Osterwalder, *A photoelectron spectrometer for k-space mapping above the Fermi level*, Rev. Sci. Instrum. **68**, 4549 (1997).

[24] M. Hengsberger, F. Baumberger, H. J. Neff, T. Greber, and J. Osterwalder, *Photoemission momentum mapping and wave function analysis of surface and bulk states on flat Cu(111) and stepped Cu(443) surfaces: A two-photon photoemission study*, Phys. Rev. B **77**, 085425 (2008).

[25] M. Bauer, M. Wessendorf, D. Hoffmann, C. Wiemann, A. Mönnich, and M. Aeschlimann, *Time-resolved 2PPE: Probing adsorbate motion on femtosecond time-scales - what is the role of the laser bandwidth?*, Appl. Phys. A **80**, 987 (2005).

[26] W. Eberhardt and F. Himpsel, *Dipole selection rules for optical transitions in the fcc and bcc lattices*, Phys. Rev. B **21**, 5572 (1980).

[27] S. Roth, D. Leuenberger, J. Osterwalder, J. E. Dahl, R. M. K. Carlson, B. A. Tkachenko, A. A. Fokin, P. R. Schreiner, and M. Hengsberger, *Negative-electron-affinity diamondoid monolayers as high-brilliance source for ultrashort electron pulses*, Chem. Phys. Lett. **495**, 102 (2010).

[28] M. Bauer and M. Aeschlimann, *Dynamics of excited electrons in metals, thin films and nanostructures*, J. Elec. Spectr. Rel. Phen. A **124**, 225 (2002).

[29] S. Roth, *Alignment and Characterisation of an Optical Parametric Amplifier*, 2007.

[30] M. Hausherr, *Generation of femtosecond 6 eV laser pulses for time-resolved photoemission applications with an elliptical display analyzer*, 2009.

[31] C. Westphal, J. Bansmann, M. Getzlaff, and G. Schönhense, *Circular dichroism in the angular distribution of photoelectrons from oriented CO molecules*, Phys. Rev. Lett. **63**, 151 (1989).

[32] H. Daimon, *Stereoscopic Microscopy of Atomic Arrangement by Circularly Polarized-Light Photoelectron Diffraction*, Phys. Rev. Lett. **86**, 2034 (2001).

[33] M. Kotsugi, Y. Miyatake, K. Enomoto, K. Fukumoto, A. Kobayashi, T. Nakatani, Y. Saitoh, T. Matsushita, S. Imada, and T. Furuhata, *Construction of two-dimensional photoelectron spectrometer at SPring-8*, Nuclear Instruments and Methods in Physics Research Section A: Accelerators, Spectrometers, Detectors and Associated Equipment **467**, 1493 (2001).

[34] K. Dörnemann, *Aufbau und Simulation eines elliptischen Energie-Analysators für Elektronenspektroskopie*, Master's thesis, Physics Institute, University of Dortmund, 1998.

[35] M. Hoesch, T. Greber, V. Petrov, M. Muntwiler, M. Hengsberger, W. Auwärter, and J. Osterwalder, *Spin-polarized Fermi surface mapping*, J. Electron Spectrosc. Relat. Phenom. **124**, 263 (2002).

[36] B. J. Siwick, J. R. Dwyer, R. E. Jordan, and R. J. D. Miller, *Ultrafast electron optics: Propagation dynamics of femtosecond electron packets*, J. Appl. Phys. **92**, 1643 (2002).

[37] S. Passlack, S. Mathias, O. Andreyev, D. Mittnacht, M. Aeschlimann, and M. Bauer, *Space charge effects in photoemission with a low repetition, high intensity femtosecond laser source*, J. Appl. Phys. **100**, 024912 (2006).

[38] D. Leuenberger, H. Yanagisawa, S. Roth, J. Osterwalder, and M. Hengsberger, *Disentanglement of electron dynamics and space-charge effects in time-resolved photoemission from h-BN/Ni(111)*, Phys. Rev. B **84**, 125107 (2011).

[39] J. Rice, *Mathematical Statistics and Data Analysis*, Duxbury Press, second edition, 1995.

[40] F. Baumberger, T. Greber, and J. Osterwalder, *Fermi surface of the two-dimensional surface states on vicinal Cu(111)*, Phys. Rev. B **64**, 195411 (2001).

[41] W. Auwärter, *One Monolayer of Hexagonal Boron Nitride on Ni(111): an Atomically Sharp Interface*, PhD thesis, University of Zurich, 2003.

[42] W. Auwärter, T. J. Kreutz, T. Greber, and J. Osterwalder, *XPD and STM investigation of hexagonal boron nitride on Ni(111)*, Surface Science **429**, 229 (1999).

[43] G. Grad, P. Blaha, K. Schwarz, W. Auwärter, and T. Greber, *Density functional theory investigation of the geometric and spintronic structure of h-BN/Ni(111) in view of photoemission and STM experiments*, Phys. Rev. B **68**, 085404 (2003).

[44] C. Oshima and A. Nagashima, *Ultra-thin epitaxial films of graphite and hexagonal boron nitride on solid surfaces*, J. Phys.: Condens. Matter **9**, 1 (1997).

[45] K. Zumbrägel, K. Wulff, C. Eibl, M. Donath, and M. Hengsberger, *Exchange-split interface state at h-BN/Ni(111)*, Phys. Rev. B **78**, 085422 (2008).

[46] M. Muntwiler, M. Hengsberger, A. Dolocan, H. J. Neff, T. Greber, and J. Osterwalder, *Energetics and dynamics of unoccupied electronic states at the h-BN/Ni(111) interface*, Phys. Rev. B **75**, 075407 (2007).

[47] H. Lüth, *Solid Surfaces, Interfaces and thin Films*, Springer Verlag (Berlin, Heidelberg, London, New York), 4 edition, 2001.

[48] M. Corso, W. Auwärter, M. Muntwiler, A. Tamai, T. Greber, and J. Osterwalder, *Boron Nitride Nanomesh*, Science **303**, 217 (2004).

[49] D. Leuenberger, *Time-resolved photoemission from h-BN/Ni(111) across the ferromagnetic phase transition*, Master's thesis, University of Zurich, 2007.

[50] S. Gsell, *Wachstum von großflächigen einkristallinen Diamantschichten mittels Heteroepitaxie auf Silizium: Entwicklung von Pufferschichtsystemen und Untersuchung der Nukleationsmechanismen*, PhD thesis, University of Augsburg, 2008.

[51] E. Bertel and M. Donath, *Electronic surface and interface States on metallic systems*, World Scientific (Singapur), 1994.

[52] P. M. Echenique and J. B. Pendry, *The existence and detection of Rydberg states at surfaces*, J. Phys. C: Solid State Phys. **11**, 2065 (1978).

[53] M. W. Cole and M. H. Cohen, *Image-potential-induced surface bands in insulators*, Phys. Rev. Lett. **23**, 1238 (1969).

[54] N. Garcia and J. Solana, *Surface states in a one-dimensional crystal*, Surf. Sci. **36**, 262 (1973).

[55] C. Harris, N. Ge, R. Lingle, J. McNeill, and C. Wong, *Femtosecond dynamics of electrons on surfaces and at interfaces 1*, Annual review of physical chemistry **48**, 711 (1997).

[56] U. H. ofer, I. Shumay, C. Reuß, U. Thomann, W. Wallauer, and T. Fauster, *Time-resolved coherent photoelectron spectroscopy of quantized electronic states on metal surfaces*, Science **227**, 1480 (1997).

[57] A. Hotzel, G. Moos, K. Ishioka, M. Wolf, and G. Ertl, *Femtosecond electron dynamics at absorbate-metal interfaces and the dielectric continuum model*, Appl. Phys. B: Lasers and Optics **68**, 615 (1999).

[58] J. Güdde and U. Höfer, *Femtosecond time-resolved studies of image-potential states at surfaces and interfaces of rare-gas adlayers*, Prog. Surf. Sci. **80**, 49 (2005).

[59] G. Dutton and X.-Y. Zhu, *Unoccupied States in C_{60} Thin Films Probed by Two-Photon Photoemission*, J. Phys. Chem. B **106**, 5975 (2002).

[60] A. Catellani, M. Posternak, A. Baldereschi, H. J. F. Jansen, and A. J. Freeman, *Electronic interlayer states in hexagonal boron nitride*, Phys. Rev. B **32**, 6997 (1985).

[61] A. Catellani, M. Posternak, A. Baldereschi, and A. J. Freeman, *Bulk and surface electronic structure of hexagonal boron nitride*, Phys. Rev. B **32**, 6997 (1987).

[62] X. Blase, A. Rubio, and S. Louie, *Quasiparticle band structure of bulk hexagonal boron nitride and related systems*, Phys. Rev. B **51**, 6868 (1995).

[63] R. I. G. Uhrberg, G. V. Hansson, J. M. Nicholls, and S. A. Flodström, *Experimental Evidence for one Highly Dispersive Dangling-Bond Band on Si(111) (2×1)*, Phys. Rev. Lett. **48**, 1032 (1982).

[64] P. Perfetti, J. M. Nicholls, and B. Reihl, *Unoccupied surface-state band on Si(111) (2×1)*, Phys. Rev. B **36**, 6160 (1987).

[65] P. Chiaradia, A. Cricenti, S. Selci, and G. Chiarotti, *Differential reflectivity of Si(111) (2×1) surface with polarized light: a test for surface structure*, Phys. Rev. Lett. **52**, 1145 (1984).

[66] M. Rohlfing and S. G. Louie, *Excitons and Optical Spectrum of the Si(111) (2×1) Surface*, Phys. Rev. Lett. **83**, 856 (1999).

[67] M. Weinelt, M. Kutschera, T. Fauster, and M. Rohlfing, *Dynamics of exciton formation at the Si(100) c(4×2) surface*, Phys. Rev. Lett. **92**, 126801 (2004).

[68] P. Perfetti, T. Riesterer, M. Tschudy, and B. Reihl, *Angle-resolved inverse photoemission of GaP(110)*, Surf. Sci. **189/190**, 556 (1987).

[69] F. Sette, P. Perfetti, F. Patella, C. Quaresima, C. Capasso, M. Capozi, and A. Savoia, *Resonant photoemission from surface states in GaP*, Phys. Rev. B **28**, 4882 (1983).

[70] M. Muntwiler and X. Y. Zhu, *Dynamics at Solid State Surfaces and Interfaces*, Vol. Vol. 1: Current Developments, Wiley-VCH, 2010.

[71] R. Prasad, S. Auluck, and S. K. Joshi, *Wavevector dependent susceptibility and dielectric function for paramagnetic nickel*, J. Phys. F: Metal Phys. **6**, 889 (1976).

[72] H. Dil, J. Lobo-Checa, R. Laskowski, P. Blaha, S. Berner, J. Osterwalder, and T. Greber, *Surface Trapping of Atoms and Molecules with Dipole Rings*, Science **319**, 1824 (2008).

[73] A. Goriachko, Y. He, M. Knapp, H. Over, M. Corso, T. Brugger, S. Berner, J. Osterwalder, and T. Greber, *Self-Assembly of a Hexagonal Boron Nitride Nanomesh on Ru(0001)*, Langmuir **23**, 2928 (2007).

[74] T. Brugger, S. Günther, B. Wang, J. H. Dil, M.-L. Bocquet, J. Osterwalder, J. Wintterlin, and T. Greber, *Comparison of electronic structure and template function of single-layer graphene and a hexagonal boron nitride nanomesh on Ru(0001)*, Phys. Rev. B **79**, 045407 (2009).

[75] M. Morscher, M. Corso, T. Greber, and J. Osterwalder, *Formation of single layer h-BN on Pd(111)*, Surf. Sci. **600**, 3280 (2006).

[76] M. P. Allan, S. Berner, M. Corso, T. Greber, and J. Osterwalder, *Tunable self-assembly of one-dimensional nanostructures with orthogonal directions*, Nanorscale Res. Lett. 2 **94** (2007).

[77] R. Laskowski, P. Blaha, T. Gallauner, and K. Schwarz, *Single-Layer Model of the Hexagonal Boron Nitride Nanomesh on the Rh(111) Surface*, Phys. Rev. Lett. **98**, 106802 (2007).

[78] M. Corso, *Boron Nitride Nanostructures on Transition Metals: Flat Layers and Nanomesh*, PhD thesis, University of Zurich, 2006.

[79] A. Dolocan, *Time-Resolved Low-Energy Electron Diffraction and Photoemission Pump-Probe Experiments*, PhD thesis, University of Zurich, 2006.

[80] W. Di, S. Dhar, K. E. Smith, and S. D. Kevan, *Angle-resolved photoemission study of the clean and hydrogen-covered Rh(111) surface*, Phys. Rev. B **49**, 4821 (1994).

[81] D. A. Papaconstantopoulos, *Handbook of the Band Structure of Elemental Solids*, Pentum Press, 1986.

[82] www.ioffe.ru

[83] F. Schmitt, P. S. Kirchmann, U. Bovensiepen, R. G. Moore, L. Rettig, M. Krenz, J.-H. Chu, N. Ru, L. Perfetti, D. H. Lu, M. Wolf, I. R. Fisher, and Z. X. Shen, *Transient Electronic Structure and Melting of a Charge Density Wave in* $TbTe_3$, Science **321**, 1649 (2008).

[84] T. Rohwer, S. Hellmann, M. Wiesenmayer, C. Sohrt, A. Stange, B. Slomski, A. Carr, Y. Liu, L. M. Avila, M. Kalläne, S. Mathias, L. Kipp, K. Rossnagel, and M. Bauer, *Collapse of long-range charge order tracked by time-resolved photoemission at high momenta*, Nature , 1 (2011).

[85] S. Hellmann, M. Beye, C. Sohrt, T. Rohwer, F. Sorgenfrei, H. Redlin, M. Kalläne, M. Marczynski-Bühlow, F. Hennies, M. Bauer, A. Föhlisch, L. Kipp, W. Wurth, and K. Rossnagel, *Ultrafast Melting of a Charge-Density Wave in the Mott Insulator 1T-*TaS_2, Phys. Rev. Lett. **105**, 187401 (2010).

[86] A. L. Cavalieri et al., *Attosecond spectroscopy in condensed matter*, Nature **449**, 1029 (2007).

[87] X. Zhou, B. Wannberg, W. Yang, V. Brouet, Z. Sun, J. Douglas, D. Dessau, Z. Hussain, and Z. Shen, *Space charge effect and mirror charge effect in photoemission spectroscopy*, Journal of electron spectroscopy and related phenomena **142**, 27 (2005).

[88] A. Pietzsch, A. Föhlisch, M. Beye, M. Deppe, F. Hennies, M. Nagasono, E. Suljoti, W. Wurth, C. Gahl, K. Döbrich, and A. Melnikov, *Towards time resolved core level photoelectron spectroscopy with femtosecond x-ray free-electron lasers*, New Journal of Physics **10**, 033004 (2008).

[89] K. Moribayashi, *Application of photoelectron spectroscopy to the measurement of the flux of x-ray free-electron lasers irradiating clusters or biomolecules*, Physical Review A **80**, 025403 (2009).

[90] C. Cirelli, M. Hengsberger, A. Dolocan, H. Over, J. Osterwalder, and T. Greber, *Direct observation of space charge dynamics by picosecond low-energy electron scattering*, Europhys. Lett. **85**, 17010 (2009).

[91] S. Hellmann, K. Rossnagel, M. Marczynski-Bühlow, and L. Kipp, *Vacuum space-charge effects in solid-state photoemission*, Phys. Rev. B **79**, 035402 (2009).

[92] J. Robertson, *Electronic structure and core exciton of hexagonal boron nitride*, Phys. Rev. B **29**, 2131 (1984).

[93] M. Wolf, A. Hotzel, E. Knoesel, and D. Velic, *Direct and indirect excitation mechanisms in two-photon photoemission spectroscopy of Cu (111) and CO/Cu (111)*, Phys. Rev. B **59**, 5926 (1999).

[94] N. V. Smith, *Phase analysis of image states and surface states associated with nearly-free-electron band gaps*, Phys. Rev. B **32**, 3549 (1985).

[95] R. F. Garrett and N. V. Smith, *Unoccupied bulk, surface, and image states on Ni(001), Ni(111), and Ni(110)*, Phys. Rev. B **33**, 3740 (1986).

[96] F. J. Himpsel, *Image states at ferromagnetic surfaces: Fe(110), (100), (111) and Co(0001)*, Phys. Rev. B **43**, 13394 (1991).

[97] A. B. Schmidt, M. Pickel, M. Donath, and M. Weinelt, *Ultrafast spin dependent electron dynamics at the surface of ferromagnetic thin films*, J. Magn. Magn. Mat. **310**, 2330 (2007).

[98] M. Nekovee, S. Crampin, and J. E. Inglesfield, *Magnetic Splitting of Image States at Fe(110)*, Phys. Rev. Lett. **70**, 3099 (1993).

[99] F. Passek and M. Donath, *Spin-Split Image-Potential-Induced Surface State on Ni(111)*, Phys. Rev. Lett. **69**, 1101 (1992).

[100] F. Passek, M. Donath, K. Ertl, and V. Dose, *Longer Living Majority than Minority Image State at Fe(110)*, Phys. Rev. Lett. **75**, 16163 (1995).

[101] U. Thomann, C. Reuss, T. Fauster, F. Passek, and M. Donath, *Image-potential states on bcc(110) surfaces of iron and tungsten*, Phys. Rev. B **61**, 16163 (2000).

[102] N. Fischer, S. Schuppler, T. Fauster, and W. Steinmann, *Intrinsic linewidths of image-potential states on Ni(111)*, Phys. Rev. B **42**, 9717 (1990).

[103] M. Weinelt, A. B. Schmidt, M. Pickel, and M. Donath, *Spin-polarized image-potential-state electrons as ultrafast magnetic sensors in front of ferromagnetic surfaces*, Progr. Surf. Sci. **82**, 388 (2007).

[104] J. Hohlfeld and E. Matthias, *Nonequilibrium Magnetization Dynamics of Nickel*, Phys. Rev. Lett. **78**, 4861 (1997).

[105] A. Scholl, L. Baumgartner, R. Jacquemin, and W. Eberhardt, *Ultrafast Spin Dynamics of Ferromagnetic Thin Films Observed by fs Spin-Resolved Two-Photon Photoemission*, Phys. Rev. B **79**, 5146 (1997).

[106] H. Regensburger, R. Vollmer, and J. Kirschner, *Time-resolved magnetization-induced second-harmonic generation from the Ni(110) surface*, Phys. Rev. B **61**, 14716 (2000).

[107] P. M. Oppeneer and A. Liebsch, *Ultrafast demagnetization in Ni: theory of magneto-optics for non-equilibrium electron distributions*, J. Phys.: Cond. Mat. **16**, 5519 (2004).

[108] R. Paniago, R. Matzdorf, G. Meister, and A. Goldmann, *Temperature dependence of Shockley-type surface energy bands on Cu(111), Ag(111) and Au(111)*, Surf. Sci. **336**, 113 (1995).

[109] J. S. Kouvel and J. B. Comly, *Magnetic Equation of State for Nickel near its Curie Point*, Phys. Rev. Lett. **20**, 1237 (1968).

[110] M. Hengsberger, M. Muntwiler, T. Greber, and J. Lobo-Checa, *Source for spin-polarized electrons*, US patent no. WO 2007/006168, 2006.

[111] J. J. Yeh and I. Lindau, At. Data Nuc. Data Tables **32** (1985).

[112] R. Knorren, K. H. Bennemann, R. Burgmeister, and M. Aeschlimann, *Dynamics of excited electrons in copper and ferromagnetic transition metals: Theory and experiment*, Phys. Rev. B **61**, 9427 (2000).

[113] U. Bovensiepen, *Coherent and incoherent excitations of the Gd(0001) surface on ultrafast timescales*, J. Phys. Condens. Matter **19**, 083201 (2007).

[114] V. L. Moruzzi, J. F. Janak, and A. R. Williams, *Calculated electronic properties of metals*, Pergamon Press, New York, 1978.

[115] G. Borstel and G. Thörner, *Inverse photoemission from solids: Theoretical aspects and applications*, Surf. Sci. Rep. **8**, 8627 (1988).

[116] Y. Yafet, F. Seit, and D. Turnbull, Solid State Physics **14** (1963).

[117] B. Koopmans, H. H. J. E. Kicken, M. van Kampen, and W. J. M. de Jonge, *Microscopic model for femtosecond magnetization dynamics*, J. Magn. Magn. Mat. **286**, 271 (2005).

[118] B. Koopmans, J. J. M. Ruigrok, F. D. Longa, and W. J. M. de Jonge, *Unifying Ultrafast Magnetization Dynamics*, Phys. Rev. Lett. **95**, 267207 (2005).

[119] M. Aeschlimann, M. Bauer, S. Pawlik, R. Knorren, G. Bouzerar, and K. H. Bennemann, *Transport and dynamics of optically excited electrons in metals*, Appl. Phys. A **71**, 485 (2000).

[120] S. V. H. C. Sondergaard, C. Schultz, Z. Li, and Ph. Hofmann, *An undulator-based spherical grating monochromator beamline for angle-resolved photoemission spectroscopy*, Nucl. Instrum. Methods Phys. Res. **411**, Sect. A 523 (2004).

[121] S. Agergaard, C. Sondergaard, H. Li, M. B. Nielsen, S. V. Hoffmann, Z. Li, and Ph. Hofmann, *The effect of reduced dimensionality on a semimetal: the electronic structure of the Bi(110) surface*, New J. of Phys. **3**, 15.1 (2001).

[122] F. Meier, H. Dil, J. Lobo-Checa, L. Patthey, and J. Osterwalder, *Quantitative vectorial spin analysis in angle-resolved photoemission: Bi/Ag(111) and Pb/Ag(111)*, Phys. Rev. B **77**, 165431 (2008).

[123] Y. A. Bychkov and E. I. Rashba, *Oscillatory effects and the magnetic susceptibility of carriers in inversion layers*, J. of Phys. C: Solid State Physics **17**, 6039 (1984).

[124] A. Kimura, E. E. Krasovskii, R. Nishimura, K. Miyamoto, T. Kadono, K. Kanomaru, E. V. Chulkov, G. Bihlmayer, K. Shimada, H. Namatame, and M. Taniguchi, *Strong Rashba-Type Spin Polarization of the Photocurrent from Bulk Continuum States: Exeriment and Theory for Bi(111)*, Phys. Rev. Lett. **105**, 076804 (2010).

[125] C. M. Schneider and J. Kirschner, *Spin- and angle-resolved photoelectron spectroscopy from solid surfaces with circularly polarized light*, Critical Reviews in Solid State and Materials Sciences **20:3**, 179 (1995).

[126] Y. H. Wang, D. Hsieh, D. Pilon, L. Fu, D. R. Gardener, Y. S. Lee, and N. Gedik, *Observation of a Warped Helical Spin Texture in* Bi_2Se_3 *from Circular Dichroism Angle-Resolved Photoemission Spectroscopy*, Phys. Rev. Lett. **107**, 207602 (2011).

[127] J. H. Dil, F. Meier, J. Lobo-Checa, L. Patthey, G. Bihlmayer, and J. Osterwalder, *Rashba-Type Spin-Orbit Splitting of Quantum Well States in Ultrathin Pb Films*, Phys. Rev. Lett. **101**, 266802 (2008).

[128] F. Meier, V. Petrov, S. Guerrero, C. Mudry, L. Patthey, J. Osterwalder, and J. H. Dil, *Unconventional Fermi surface spin textures in the* $Bi_xPb_{1-x}/Ag(111)$ *surface alloy*, Phys. Rev. B **79**, 241408 (2009).

[129] L. Perfetti, P. A. Loukakos, M. Lisowski, U. Bovensiepen, M. Wolf, H. Berger, S. Biermann, and A. Georges, *Femtosecond dynamics of electronic states in the Mott insulator* $1T\text{-}TaS_2$ *by time resolved photoelectron spectroscopy*, New J. Phys. **10**, 053019 (2008).

[130] B. Rethfeld, A. Kaiser, M. Vicanek, and G. Simon, *Ultrafast dynamics of nonequilibrium electrons in metals under femtosecond laser irradiation*, Phys. Rev. B **65**, 214303 (2002).

[131] J. J. Quinn and R. A. Ferrell, *Electron self-energy approach to correlation in a degenerate electron gas*, Phys. Rev. **112**, 812 (1958).

[132] P. S. Kirchmann, *Ultrafast Electron Dynamics in Low-Dimensional Materials*, PhD thesis, Freie Universität Berlin, 2009.

[133] A. Eiguren, B. Hellsing, F. Reinert, G. Nicolay, E. V. Chulkov, V. M. Silkin, S. Hüfner, and P. M. Echenique, *Role of Bulk and Surface Phonons in the Decay of Metal Surface States*, Phys. Rev. Lett. **88**, 066805 (2002).

[134] C. Kirkegaard, T. K. Kim, and Ph. Hofmann, *Self-energy determination and electron–phonon coupling on Bi(110)*, New J. of Phys. **7**, 99 (2005).

[135] Y. Liu and R. E. Allen, *Electronic structure of the semimetals Bi and Sb*, Phys. Rev. B **52**, 1566 (1995).

[136] L. Ley, R. A. Pollack, S. P. Kowalczyk, R. McFeely, and D. A. Shirley, *Evidence of Covalent Bonding in Crystalline and Amorphous As, Sb, and Bi from Valence-Band Photoelectron Spectra*, Phys. Rev. B **8**, 641 (1973).

[137] T. J. Kreutz, *The temperature-dependent electronic structure of nickel metal*, PhD thesis, University of Zurich, 1997.

[138] X. Gonze, J. P. Michenaud, and J. P. Vigneron, *First-principles study of As, Sb, and Bi electronic properties*, Phys. Rev. B **41**, 11827 (1990).

[139] P. B. Allen, *Theory of Thermal Relaxation of Electron in Metals*, Phys. Rev. Lett. **59**, 1460 (1987).

[140] D. Boschetto, E. G. Gamaly, A. V. Rode, B. Luther-Davies, D. Glijer, T. Garl, O. Albert, A. Rousse, and J. Etchepare, *Small atomic displacements recorded in bismuth by the optical reflectivity of femtosecond laser-pulse excitations*, Phys. Rev. Lett. **69**, 027404 (2008).

[141] N. E. Phillips, *Nuclear Quadrupole and Electronic Heat Capacities of Bismuth*, Phys. Rev. , 7218 (1960).

[142] D. Boschetto, T. Garl, and A. Rousse, *Ultrafast dielectric function dynamics in bismuth*, Journal of Modern Optics **57**, 953 (2010).

[143] Y. R. Shen and N. Bloembergen, *Theory of Stimulated Brillouin and Raman Scattering*, Phys. Rev. **137** (1965).

[144] M. Aeschlimann, M. Bauer, and S. Pawlik, *Competing nonradiative channels for hot electron induced surface photochemistry*, Chem. Phys. **205**, 127 (1996).

[145] M. Aeschlimann, M. Bauer, S. Pawlik, R. Knorren, G. Bouzerar, and K. H. Bennemann, *Transport and dynamics of optically excited electrons in metals*, Appl. Phys. A **71**, 485 (2000).

[146] J. E. Gayone, C. Kirkegaard, J. W. Wells, S. V. Hoffmann, Z. Li, and Ph. Hofmann, *Determining the electron-phonon mass enhancement parameter λ on metal surfaces*, Appl. Phys. A **80**, 943 (2005).

[147] L. Perfetti, P. A. Loukakos, M. Lisowski, U. B. H. Eisaki, and M. Wolf, *Ultrafast Electron Relaxation in Superconducting $Bi_2Sr_2CaCu_2O_{8+\delta}$ by Time-Resolved Photoelectron Spectroscopy*, Phys. Rev. Lett. **99**, 197001 (2007).

[148] T. Kampfrath, L. Perfetti, F. Schapper, C. Frischkorn, and M. Wolf, *Strongly Coupled Optical Phonons in the Ultrafast Dynamics of the Electronic Energy and Current Relaxation in Graphite*, Phys. Rev. Lett. **95**, 187403 (2005).

[149] P. A. Loukakos, M. Lisowski, G. Bihlmayer, S. Blügel, M. Wolf, and U. Bovensiepen, *Dynamics of the Self-Energy of the Gd(0001) Surface State Probed by Femtosecond Photoemission Spectroscopy*, Phys. Rev. Lett. **98**, 097401 (2007).

[150] K. Ishioka and O. V. Misochko, Progress in Ultrafast Intense Laser Science **V**, 1 (2009).

[151] T. K. Cheng, S. D. Brorson, A. S. Kazeroonian, J. S. Moodera, G. Dresselhaus, M. S. Dresselhaus, and E. P. Ippen, *Impulsive excitation of coherent phonons observed in reflection in bismuth and antimony*, Appl. Phys. Lett. **57**, 1004 (1990).

[152] M. Hase, K. Mizoguchi, H. Harima, S. Nakashima, M. Tani, K. Sakai, and M. Hangyo, *Optical control of coherent optical phonons in bismuth films*, Appl. Phys. Lett. **100**, 2474 (1996).

[153] K. Sokolowski-Tinten, C. Blome, J. Blums, A. Cavalleri, C. Dietrich, A. Tarasevitch, I. Uschmann, E. Förster, M. Kammler, M. H. von Hoegen, and D. von der Linde, *Femtosecond X-ray measurement of coherent lattice vibrations near the Lindemann stability limit*, Nature **422**, 287 (2003).

[154] D. M. Fritz et al., *Ultrafast Bond Softening in Bismuth: Mapping a Solid's Interatomic Potential with X-rays*, Science **315**, 633 (2007).

[155] S. L. Johnson, P. Beaud, E. Vorobeva, C. J. Milne, E. D. Murray, S. Fahy, and G. Ingold, *Directly observing squeezed phonon states with femtosecond X-ray diffraction*, Phys. Rev. Lett. **102**, 175503 (2009).

[156] H. J. Zeiger, J. Vidal, T. K. Cheng, E. P. Ippen, G. Dresselhaus, and M. S. Dresselhaus, *Theory for displacive excitation of coherent phonons*, Phys. Rev. B **45**, 768 (1992).

[157] R. Peierls, *More Surprises in Theoretical Physics*, Princton Univ. Press, Princton (1991).

[158] E. D. Murray, S. Fahy, D. Prendergast, T. Ogitsu, D. M. Fritz, and D. A. Reis, *Phonon dispersion relations and softening in photoexcited bismuth from first principles*, Phys. Rev. B **75**, 184301 (2007).

[159] J. L. Yarnell, J. L. Warren, R. G. Wenzel, and S. H. Koenig, Technical report, IBM J. Res. Dev., 1964.

[160] D. B. Smith, Los Alamos Report No. 3773, 1967.

[161] L. Perfetti, P. A. Loukakos, M. Lisowski, U. Bovensiepen, H. Berger, S. Biermann, P. S. Cornaglia, A. Georges, and M. Wolf, *Time Evolution of the Electronic Structure of 1T-*TaS_2 *through the Insulator-Metal Transition*, Phys. Rev. Lett. **97**, 067402 (2006).

[162] F. Schmitt, P. S. Kirchmann, U. Bovensiepen, R. G. Moore, J. H. Chu, D. H. Lu, L. Rettig, M. Wolf, I. R. Fisher, and Z. X. Shen, *Ultrafast electron dynamics in the charge density wave material* $TbTe_3$, New J. of Physics **137**, A1787 (2011).

Acknowledgements

I would like to thank all the people who contributed to this work or helped along the way.

First of all I would like to thank Jürg Osterwalder for giving my the opportunity to carry out this thesis in his well positioned group. This work profited a lot from your sharp insight into the physics, your constructive criticisms and your careful guidance.

A special Thank You goes out to my supervisor Matthias Hengsberger. This work would never have been possible without all your expertise, ideas, patience and help! Please call me whenever there is need for ”stretching the bandhas” or ”compressing some pulses”.

I also want to thank Martin Aeschlimann for the effort he made judging this thesis as an external expert. Thank you Thomas Greber for introducing me since the first students practicum to the various topics in surface physics.

I would like to thank my former laserlab mates Hirofumi Yanagisawa and Silvan Roth. It was always joyful and enlightening to work together with you guys.

Shout-outs go to my office mates from team-cophee: Hugo Dil, Fabian Meier, Bartosz Slomski, Gabriel Landolt and Stefan Muff. Thank you for sharing your physical topics as well as all the nonsense with me. I paid with a little bit of concentration for a lot of inspiration each wednesday.

I would like to thank Martin Morscher, Thomas Brugger and Martin Köckner for beeing my ”older brothers” in the ESCA Lab, for all the discussions, the experimental support and the good times.

Thank you Luca Castiglioni and Michael Greif from the MUST-team for the nice common time at conferences and in the lab. I am very grateful to all the present and past colleauges of the surface physics group as Adrian Hemmi (thank you for maintaining the Ferrari F50), Thomas Kälin, Fumihiko Matsui, Huanyao Cun, Haifeng Ma, Rasmus Westerström, Ronald Stania, Carlo Bernard, Jorge Lobo-Checa, Claudio Cirelli, Martina Corso, Andrei Dolocan and Simon Berner.

Furthermore I would like to thank the whole Physics Institute of UZH, especially: Peter Robman for the ”nanoampere-meter-special”, Kurt Bösiger, Reto Maier, Bruno Lussi, Marcel Schaffner and Silvio Scherr from the workshop team, Ruth Halter, Monika Röllin and the whole administrative team for their good organization and Roland Bernet for continuous IT support.

A thank you also goes to Christoph Quitmann for providing the EDA and Matthias Muntwiler for the discussions about metal-insulator interfaces and hot electrons in bismuth. I would like to thank Stefan Gsell and Matthias Schreck for the 80 nm nickel film.

Furthermore Philip Hofmann and Justin Wells are gratefully acknowledged for providing the vicinal Bi(114) surface as well as a lot of physical background knowledge about it. I appreciated your correspondence a lot.

Last but not least I would like to thank my family and friends: Thanks Christophe Salzmann for the last 10 years. Thanks Sascha Kuster and Serge Butz for taking a large collection of pictures of me falling asleep in front of the tv after a long day at the institute. I owe a lot of mental and physical vitality to Mario Thomann and Urs Thoma from the sg-runners.

Finally I would like to thank my brother Fabian and my parents Theres and Otto for supporting me at all times.

Curriculum Vitae

Name	Dominik Leuenberger
Birth	08.12.1979 in Luzern (LU), Schwitzerland
Nationality	Swiss

Education

since 07/2007	PhD studies of *“Electron dynamics in low-dimensional surfaces studied by time-resolved photoelectron spectroscopy”* in the Surface Physics Group of Prof. Dr. J. Osterwalder, University of Zurich, Switzerland
01/2007	Master of Science degree in Physics, University of Zurich, masters thesis: *“Time-resolved photoemission from h-BN/Ni(111) across the ferromagnetic phase transition”* Bachelor of Science degree in Physics, University of Zurich, bachelor thesis: “π_0 *mass and Panovsky ratio”*
2003 - 2006	Advanced studies in theoretical and experimental physics, University of Zurich
2000 - 2003	Undergraduate studies in physics, mathematics and astronomy, University of Zurich
07/1997	A-level diploma (Matura Typus E), Kantonsschule Obwalden, Switzerland

Working Experience

02/2007 - 05/2007	Research assistant in the group of Prof. Dr. Jürg Osterwalder, University of Zurich
09/1999 - 10/2000	Project collaborator, Department for Electrical Engineering, Lucerne University of Applied Sciences and Arts

Teaching Experience

since Oct 2002	Teaching assistant at the University of Zurich; taught lab-courses and problem classes in physics for medical, biology and physics students.

Publications

1. H. Yanagisawa, C. Hafner, P. Dona, M. Klöckner, D. Leuenberger, T. Greber, M. Hengsberger, and J. Osterwalder,
   “Optical control of field-emission sites by femtosecond laser pulses”,
   Phys. Rev. Lett. **103**, 257603 (2009).

2. H. Yanagisawa, C. Hafner, P. Dona, M. Klöckner, D. Leuenberger, T. Greber, J. Osterwalder, and M. Hengsberger,
   “Laser-induced field emission from a tungsten tip: optical control of emission sites and the emission process”,
   Phys. Rev. B **81**, 115429 (2010).

3. M. Hengsberger, D. Leuenberger, and S. Roth,
   “Modengekoppelete Laser - (Im-)Pulse für die Forschung”,
   Bulletin SEV/VSE Electrosuisse 6/2010.

4. S. Roth, D. Leuenberger, J. Osterwalder, J.E. Dahl, R.M.K. Carlson, B. Tkachenko, A.A. Fokin, P.R. Schreiner, and M. Hengsberger,
   “Negative-electron-affinity diamondoid monolayers as high-brilliance source for ultrashort electron pulses”,
   Chem. Phys. Lett. **495**, 102 (2010).

5. L. Castiglioni, M. Greif, D. Leuenberger, S. Roth, J. Osterwalder, and M. Hengsberger,
   “Time-resolved photoelectron spectroscopy to probe ultrafast charge transfer and electron dynamics in solid surface systems and metal-molecule interfaces”,
   Chimia **65**, 342 (2011).

6. H. Yanagisawa, M. Hengsberger, D. Leuenberger, M. Klöckner, C. Hafner, T. Greber, and J. Osterwalder,
   “Energy distribution curves of ultrafast laser-induced field emission and their implications for electron dynamics”,
   Phys. Rev. Lett. **107**, 087601 (2011).

7. D. Leuenberger, H. Yanagisawa, S. Roth, J. Osterwalder, and M. Hengsberger,
   “Disentanglement of electron dynamics and space-charge effects in time-resolved photoemission from h-BN/Ni(111)”,
   Phys. Rev. B **84**, 125107 (2011).

8. L. Castiglioni, D. Leuenberger, M. Greif and M. Hengsberger,
   “Attosecond Transversal Streaking to Probe Electron Dynamics at Surfaces”,
   ICOMP12-ATTO3 proc., (2011)